



CCI
BIOMASS

CLIMATE ASSESSMENT REPORT
YEAR 3
VERSION 3.0

DOCUMENT REF:	CCI_BIOMASS_CAR_V3
DELIVERABLE REF:	D5.1_CAR
VERSION:	3.0
CREATION DATE:	2020-09-01
LAST MODIFIED	

	Ref	CCI Biomass Climate Assessment Report v3		
	Issue	Page	Date	
	3.0	2	14.07.2021	

Document Authorship

	NAME	FUNCTION	ORGANISATION	SIGNATURE	DATE
PREPARED	P. Ciais	WP8 Lead	LSCE		
PREPARED	H. Yang		LSCE		
PREPARED	Y. Y. Huang		LSCE		
PREPARED	M. Santoro		Gamma		
PREPARED	W. Li		LSCE		
PREPARED	Y. L. Wang		LSCE		
PREPARED	A. Bastos		LMU		
PREPARED	D. S. Goll		University Augsburg		
PREPARED	S. de Bruin		Wageningen University		
PREPARED	R. Lucas		Aberystwyth University		
VERIFIED	S. Quegan	Science Leader	Sheffield University		
APPROVED					

Document Distribution

ORGANISATION	NAME	QUANTITY
ESA	Frank Seifert	

Document History

VERSION	DATE	DESCRIPTION	APPROVED
0.1	2019-09-01	First draft version	14 07 2021
1.0	2019-09-03	Finalised version	

Document Change Record (from Year 1 to Year 2)

VERSION	DATE	DESCRIPTION	APPROVED







	Ref	CCI Biomass Climate Assessment Report v3		
	Issue	Page	Date	
	3.0	3	14.07.2021	

TABLE OF CONTENTS

List of tables.....	5
List of figures	6
Symbols and acronyms.....	10
1. Biomass in Climate Models.....	11
2. Processes controlling the dynamics of biomass.....	14
2.1. Gross Primary Productivity	14
2.2. Carbon use and biomass production efficiency	15
2.3. Allocation of net primary productivity to biomass pools.....	15
2.4. Mortality.....	16
2.5. Land use change and harvest affecting biomass.....	17
2.6. Turnover times	17
3. Evaluation of biomass in carbon cycle models	19
3.1. Materials and methods	22
3.1.1. Modelling biomass in global climate/carbon process-based models.....	22
3.2. Evaluation of DGVMs using CCI Biomass dataset	24
3.2.1. Global and Biome estimates.....	24
3.2.2. Global, regional and local spatial variability of AGB density	26
3.3. Conclusions	29
4. Towards an evaluation of carbon allocation and turnover times in models.....	30
4.1. Data assimilation of carbon allocation and turnover times from EO data.....	30
4.1.1. Parameter optimization.....	30
4.1.2. Input data to the carbon cycle data assimilation system	33
4.1.3. Input data to constrain carbon allocation and turnovers.....	36
4.1.4. Uncertainties in carbon allocation and turnover times.....	37
4.2. Spatial patterns of carbon allocation and turnover	37
4.3. Evaluation using ground-based measurements.....	39
4.4. Trade-offs between allocation to growth and turnover time	41
4.5. Factors influencing spatial gradients of carbon allocation and turnover times	41
5. Tropical biomass change. Case study of impacts and legacy from the 2015-16 El Niño event.....	46
5.1. Data and Methods.....	47
5.1.1. L-VOD AGB data	47
5.1.2. Forest cover data	47
5.1.3. Drought characteristics.....	47
5.1.4. AGB response and recovery.....	48
5.1.5. Variable importance and partial dependence	48
5.2. Severity, duration and onset timing of 2015/16 drought	52

	Ref	CCI Biomass Climate Assessment Report v3		
	Issue	Page	Date	
	3.0	4	14.07.2021	

5.3.	Changes in AGB during and after drought	53
5.4.	Factors influencing AGB changes during and after drought	56
5.4.1.	AGB changes during the drought.....	56
5.4.2.	AGB recovery	57
6.	<i>Biomass change products</i>	61
7.	<i>Forest edges biomass carbon deficits in Africa</i>	64
7.1.	Forest Edge characteristics and AGB deficits compared to interior forests	65
7.2.	Fire impacts on edge effects	66
8.	<i>Preliminary global estimates of AGB changes combining SMOS passive microwave data and CCI Biomass high resolution maps</i>	67
8.1.	Regional aboveground biomass (AGB) changes	68
8.2.	AGB changes attributed to disturbances.....	70
8.3.	AGB changes in relation to forest age.....	72
8.4.	Interannual variability of AGB changes	72
9.	<i>References</i>	73

	Ref	CCI Biomass Climate Assessment Report v3		
	Issue	Page	Date	
	3.0	5	14.07.2021	

LIST OF TABLES

Table 1-1: A brief summary of global model ensembles	12
Table 3-1: A brief summary of different regional/global above-ground biomass datasets.....	20
Table 3-2: A brief description of 15 DGVMs from the Trendy v8 project.	23
Table 4-1: The prior value of the optimized parameters and their uncertainties.	32
Table 4-2: The definition of forest and grass.	33
Table 5-1: The predictor variables used in Random Forest.	49
Table 5-2: The confusion matrix of the classification results using the Random Forest model. The classification is based on the RF-predicted and observed percentage of AGB recovery (%). “Yes” indicates that, by 2019, forest where AGB decreased has fully recovered to its pre-drought AGB level. “No” indicates that, by 2019, forest where AGB decreased has not fully recovered to its pre-drought AGB level.	52
Table 7-1: Carbon deficit from edge effects, fire-increased carbon deficit and area with edge effects. Note that carbon deficit from edge effects includes fire-increased carbon deficit. The weighted median of density of carbon deficit and density of fire-increased carbon deficit are shown in the table.	66

LIST OF FIGURES

Figure 3-1: Spatial patterns of 0.5-degree above-ground biomass circa the year 2017 derived from the CCI Biomass product, defined by tree cover thresholds of 0%, 15%, 20%, 25% and 30%.	21
Figure 3-2: Spatial patterns of 0.5-degree forest area, defined by tree cover thresholds of 15%, 20%, 25% and 30%.	22
Figure 3-3: Map of six Köppen-Geiger climate biomes. TRO W = wet tropical, TRO D = dry tropical, ARID = arid, TMP = temperate, BOREAL = boreal, POL = polar.....	24
Figure 3-4: Global total all plants AGB (black bars) and forest AGB (green bars) circa the year 2017 derived from the CCI Biomass dataset and DGVMs. Based on the Hansen dataset, forest pixels are defined in the CCI Biomass dataset by the tree cover thresholds of 15%, 20%, 25% and 30%.....	25
Figure 3-5: (a) Biases in the total all plants and forest AGB (simulated minus CCI Biomass data) in six biomes circa 2017. The Köppen-Geiger climate classification map (see Figure 3-3) is used to determine biome types. TRO W = wet tropical, TRO D = dry tropical, ARID = arid, TMP = temperate, BOREAL = boreal, POL = polar.....	26
Figure 3-6: (a) Difference in AGB density of all plants between the multi-model ensemble of Trendy DGVMs and CCI Biomass. (b) Difference in AGB density of forests between the multi-model ensemble of Trendy DGVMs and CCI Biomass. Forest AGB density from CCI Biomass are defined using 30% tree cover threshold.....	26
Figure 3-7: Spatial patterns of correlation coefficients between the CCI Biomass and simulated spatial local variation of all plants AGB density (individual panels labelled by model name). The correlation coefficients are calculated using all 0.5° grid cells of AGB density within super-grid-cells of 10°.....	27
Figure 3-8: Same as Figure 3-8, but for forest AGB density.....	28
Figure 3-9: The observed and simulated sensitivity of AGB density to precipitation (a) and temperature (b) in six biomes. MME is the multi-model ensemble mean of 15 DGVMs. The sensitivities are calculated using linear regression, $AGB = \beta_0 + \beta_1Pre + \beta_2Tmp$. The residuals in AGB density of the fitting regression model are in (c) and (d). AGB density are from (c) CCI Biomass and (d) the multi-model ensemble mean (MME) of 15 DGVMs. 29	
Figure 4-1: The structure of the carbon emulator and data used to retrieve 25km × 25km carbon state and process variables. Within each 25km × 25km grid cell, satellite-based NPP over forest and grassland are partitioned into the live biomass pools. Natural and climate-induced plant mortality are the output of the live biomass pools. Fire fluxes are derived from the GFED dataset. Grass grazing fluxes are from the ISIMIP2 project. Data constraints include L-VOD above-ground carbon and leaf mass. Here, leaf mass is obtained by multiplying specific leaf area (SLA) from Butler et al. (2017) and leaf area index from MODIS, GIMMS and GlobMAP datasets. ax is the allocation fraction; Sx is the biomass stocks; and rx is the rate of turnover. Details are provided in section 4.1.	33
Figure 4-2: Forest NPP, grass NPP, forest and grass cover fraction. Spatial patterns of (a) MODIS forest NPP, (b) MODIS grass NPP, (c) GIMMS forest NPP, (d) GIMMS grass NPP, (e) BESS forest NPP, and (f) BESS grass NPP during the period 2011-2016, and spatial patterns of (e) forest cover fraction and (f) grass cover fraction from MODIS land cover data.	35
Figure 4-3: Comparison between satellite-based and measured LAI from field sites in the tropics. LAI measurements cover the period 1982-2000. The linear calibration coefficients are estimated by linear regression through the origin; they are 0.95 for the satellite-based LAI from (a) GIMMS and 0.89 for those from (b) GlobMAP datasets.	36
Figure 4-4: Forest NPP allocated to leaf and wood carbon pools. The left column panels show the spatial distributions of forest NPP allocation to (a) leaf (af,L) and (b) wood (af,W) carbon pools. The right column panels show the boxplots of af,L and af,W estimates per vegetation type according to the MODIS land cover map. Vegetation types are evergreen broadleaf forest (EBF), open shrublands (OS), woody savannas (WS) and savannas (S).	37



	Ref	CCI Biomass Climate Assessment Report v3		
	Issue	Page	Date	
	3.0	7	14.07.2021	

Figure 4-5: Turnover time of forest leaf and wood carbon pools. The left column panels show the spatial distributions of turnover time of forest (a) leaf carbon pools ($1/rf,L$) and (b) wood carbon pools ($1/rf,W$) in each $25 \times 25\text{km}$ grid cell. The right column panels show the boxplots of $1/rf,L$ and $1/rf,W$ estimates for different tropical continents, including South America (SA), Africa (Af), and Southeast Asia (SEA)..... 38

Figure 4-6: Carbon allocation and turnover time from CARDAMOM. Spatial patterns of forest NPP allocation to leaf, wood and root pools, and the turnover times of forest leaf and wood carbon pools..... 38

Figure 4-7: Evaluation with ground-based NPP allocation to leaf and wood, leaf NPP and woody NPP. (a) CAT-estimated and measurement-based carbon leaf and wood allocation fractions in Amazon. Grey bars show ground measurements, while colored bars show the estimates from CAT. The errorbars for grey bars are one standard deviations of the repeated measurements from different years and plots; and the errorbars for colored bars are one standard deviations of CAT estimates resulted from different input and constraint data. (b) The comparison of plot-scale leaf litterfall and CAT-estimated leaf NPP, which are obtained as the product of leaf allocation and mean forest NPP. (c) The comparison of plot-scale woody NPP and CAT-estimated woody NPP (the product of wood allocation and mean forest NPP). The insets in (b) and (c) show the probability density function of measured and estimated leaf NPP and woody NPP. Horizontal error bars show 1 standard deviations across plots within one $25 \times 25\text{km}$ grid cell. Vertical error bars show 1 standard deviation stem from different input and constraint data. 39

Figure 4-8: Validation with measured turnover times of wood biomass pools at the mature forest plots. (a) CAT-estimated and measurement-based turnover times of wood biomass pools in the tropics. Measurement-based woody turnover time were calculated by the ratio of woody biomass and woody productivity from Brienen et al. (2015) and Galbraith et al. (2013). (b) The comparison between measurement-based and L-VOD AGB. (c) The comparison between measurement-based and satellite-based forest woody NPP. Horizontal error bars show the one standard deviations across plots within one $25 \times 25\text{km}$ grid cell. Vertical error bars show the uncertainty stem from different input or constraint data. (d) The locations of forest plots. Background color reflects the mean annual L-VOD AGB for the period 2010-2016..... 40

Figure 4-9: Relationship between leaf/wood growth and wood/leaf lifespan. Correlation coefficients between (a) leaf productivity and leaf turnover times, (b) wood productivity and wood turnover times. (c) (d) The percentage of changes in leaf and wood turnover times when leaf and wood productivity increase by 50%. These percentages are calculated using least-squares regression. Correlation and regression analysis are applied to each spatial window of $5^\circ \times 5^\circ$ 41

Figure 4-10: The relation between carbon allocation and canopy height. (a) Median of leaf and wood allocation fraction for each percentile bin of canopy height. (b) Same as (a), but for evergreen broadleaf forests, woody savannas and savannas respectively. The vertical errorbars in (a) and (b) show interquartile range of allocation fractions. 42

Figure 4-11: The relation between carbon allocation and climate and vegetation factors. Median of leaf allocation fraction for each percentile bin of (a) temperature, (b) precipitation, (c) radiation and (d) the percentage of forests associating with ectomycorrhizal (EcM) fungi. Lines with light color dots represents trees with height being less than 20 m, while lines with dark color dots represents trees with height being more than 20 m. (e)-(h) Same as (a)-(d), but for wood allocation fractions. The vertical error bars show the interquartile range of allocation fractions. 43

Figure 4-12: The relation between carbon turnover times and climate and leaf traits. Median of leaf and wood allocation fraction for each percentile bin of (a) temperature, (b) precipitation, (c) specific leaf area (SLA) and (d) leaf phosphorus concentration. The vertical error bars show interquartile range of allocation fractions. 44

Figure 4-13: The contribution of the uncertainties of carbon allocation and turnover time. (a)-(d) The percentage of standard deviation (%), relative to the mean values) of forest NPP allocation fractions, turnover time of biomass pools. (e)-(h) The contribution of uncertainty derived from the different sources of LAI (blue), NPP (green) and L-VOD AGB (red) datasets. Contribution from a certain variable is represented by a specific color, e.g. the red colored regions indicates the uncertainty is mainly from the L-VOD AGB datasets. 45



	Ref	CCI Biomass Climate Assessment Report v3		
	Issue	Page	Date	
	3.0	8	14.07.2021	

Figure 5-1: Spatial patterns of the AGB changes during the drought ($\Delta\text{AGB}_{14/15 \rightarrow 15/16}$) and the percentage of AGB recovery estimated (a), (c) by L-VOD AGB data and (b), (d) by Random Forest. 51

Figure 5-2: Spatial pattern of AGB fully-recovered and not fully recovered areas estimated (a) by L-VOD AGB data and (b) by Random Forest. The confusion matrix of the classification is in Table 5-2..... 52

Figure 5-3: Spatial patterns of the (a) severity, (b) duration and (c) onset time of the 2015/16 drought over the tropical evergreen forests. The severity, duration and onset of drought are identified based on the standardized anomaly of monthly Cumulative Water deficit anomalies (ACWD). The left-hand panels show the fractional area of tropical forests sorted into different categories of drought severity, duration and onset time. The fractional area is split into values for three continents, i.e., South America (SA), Africa (AF) and Southeast Asia (SEA). The non-forest dominated regions, forest losses regions, flooded and lake areas are masked out. 53

Figure 5-4: Spatial patterns of forest AGB changes during and after the drought. (a) Changes in AGB over the drought period in 2015/16, relative to AGB over the same period in 2014/15 ($\Delta\text{AGB}_{14/15 \rightarrow 15/16}$); (b) Decreases in AGB after the drought; (c) Increases in AGB after reached the lowest AGB point; (d) The start year of AGB recovery, i.e. the year with the lowest AGB value. Green areas correspond to areas where AGB has not reduced over the period of 2015 and 2016. Yellow areas correspond to areas where AGB in 2015/16 was the lowest and regrows immediately after the drought. Purple areas correspond to areas where AGB has not started to recover by 2019. (e) The percentage of AGB recovery, i.e., the increase in AGB after the lowest point divided by the sum of decrease in AGB during and/or after the drought. 54

Figure 5-5: Spatial patterns of the median of ACWD (i.e. the severity of drought) over the same drought month in 2016/17, 2017/18 and 2018/19. Note that the GLEAM ET data of year 2019 are not available, so we use a constant ET of 100 mm month⁻¹ to calculate ACWD in 2019 (Aragão et al., 2007). 55

Figure 5-6: The relationship between the drought severity and the start year of AGB recovery, that is also the year with the lowest AGB value. The fractions of the study area (%) with different start year of AGB recovery are shown. 56

Figure 5-7: The importance of predictor variables in fitting the AGB changes during the drought ($\Delta\text{AGB}_{14/15 \rightarrow 15/16}$), and partial dependence plots for the 6 most important variables. In the partial dependence plot, the red line is the partial dependence curve, showing the relationship between one specific predictor variable and $\Delta\text{AGB}_{14/15 \rightarrow 15/16}$, independent of other predictor variables. Black lines are the individual conditional expectation curves, displaying the dependence of $\Delta\text{AGB}_{14/15 \rightarrow 15/16}$ on corresponding predictor variables for each pixel. Ticks on the x-axis show the deciles of the distribution of the predictors. 57

Figure 5-8: Same as Figure 5-7, but for the log-transformed the percentage of AGB recovery after drought (excluding no recovery pixels). The predictors in bold are the factors strongly associated with $\Delta\text{AGB}_{14/15 \rightarrow 15/16}$ in Figure 5-7. 58

Figure 5-9: Relationship between AGB changes during the drought ($\Delta\text{AGB}_{14/15 \rightarrow 15/16}$, Figure 5-4a) and AGB changes after the drought. 58

Figure 5-10: (a) The relationships between the understory height (RH25), canopy height (RH100) and their ratio γ . (b) Spatial pattern of the ratio of RH25 and RH100. 59



Figure 5-11: (a) The start year of AGB recovery and (b) the percentage of AGB recovery per year (% per year) of canopy-closed forests where the understory height is close to the top canopy height ($\gamma \geq 0.3$), and forests with low understory ($\gamma < 0.3$). In (a), the fraction of study area (%) with different start year of AGB recovery are shown. In (b), the median of the percentage of AGB recovery per year (% per year) are calculated for different levels of soil moisture deficits during the drought year. 60

Figure 6-1: The link between Amazon deforestation (area loss) and L-VOD. 62

Figure 6-2: The correspondence between L-VOD and Landsat-derived forest loss. 62

Figure 6-3: Corresponding changes in AGB retrieved from L-VOD for China and Australia. 63

Figure 7-1: Scales and magnitudes of forest edge in Africa. (a) and (d) are the frequency distributions of scales and magnitudes; (b-c) and (e-f) are maps of scales and magnitudes. Shading in (a) and (d) indicates the

	Ref	CCI Biomass Climate Assessment Report v3		
	Issue	Page	Date	
	3.0	9	14.07.2021	



weighted interquartile ranges, and dashed lines indicate weighted medians. Gray area in (b), (c), (e) and (f) indicates grid cells without detected edge effects (27% and 18% of all grid cells for moist and dry forests). 65

Figure 7-2: Difference of forest edge effects at fire and non-fire edges (Δ scale, fire minus non-fire, a-b; Δ magnitude, c-d) for moist and dry forests and Δ Scale change with $\Delta\beta$ (enhanced bowen ratio) and fire distance (e-f). The differences in edge effects (Δ scale and Δ magnitude) are regarded as the fire impacts on edge effects. Numbers in (e-f) are the total number of 0.25° grid cells located in each $\Delta\beta$ and fire distance interval. Only grid cells with successfully fitted curves at both fire and non-fire edges and with available β at both fire and non-fire edges are shown. 67

Figure 8-1: (a) Spatial distribution of mean annual changes in aboveground biomass (AGB) carbon between 2010 to 2019. The inset shows the total net AGB changes (yellow bars) and forest area changes (black curve) for five climatic biomes. (b) Spatial distribution of the areal fraction of forest loss (2010 – 2019). The inset shows the total changes in AGB (orange bars) and forest area (orange curve) for regions with AGB loss. (c) Spatial distribution of the areal fraction of forest gains (2010 – 2019). The inset shows the total changes in AGB (green bars) and forest area (green curve) for regions with AGB gain. 70



Figure 8-2: Aboveground biomass annual changes (Δ AGB) from L-VOD (thick black line) and Trendy DGVMs, and mean net biome productivity (NBP) from inversion models (OCO2, SURF, and GOSAT) from 2010 to 2019 for five climatic biomes: wet tropics (a), dry tropics (b), arid (c), temperate (d), and boreal (e). The stacked bars of L-VOD show the subcomponents of Δ AGB that are caused by no forest loss (grey), deforestation (red), agriculture (yellow), forestry (green), wildfire (brown) and urbanization (dark blue). 71

Figure 8-3: (a) Interannual variability of reversed global atmospheric carbon growth rate (CGR, black line), global AGB fluxes from L-VOD without coarse woody debris (CWD) buffering (red line), AGB fluxes from L-VOD with CWD buffering (blue line), over 2012 – 2019. The right-hand panel shows the contribution (%) of five climate biomes to the interannual variability in global AGB fluxes from L-VOD without and with CWD buffering. The global AGB fluxes were calculated using annual AGB changes compared to the previous year. The shadings of each curve show the uncertainty of CGR, the standard deviation of L-VOD AGB estimated by different calibrations. (b) Interannual variability of reversed global atmospheric carbon growth rate (CGR, black line), global AGB fluxes from Trendy DGVMs (green lines), over 2012 – 2018. Contribution (%) of five biomes to the interannual variability in global AGB fluxes from individual TRENDY models. 73

	Ref	CCI Biomass Climate Assessment Report v3		
	Issue	Page	Date	
	3.0	10	14.07.2021	

SYMBOLS AND ACRONYMS

AGB	Above-ground Biomass
AGC	Above-ground carbon
BP	Biomass Production
BPE	Biomass Production Efficiency
CAR	Climate Assessment Report
CCI	Climate Change Initiative
CUE	Carbon Use Efficiency
DGVM	Dynamic Global Vegetation Model
DTR	Diurnal Temperature Range
EBF	Evergreen Broadleaf Forest
ESM	Earth System Model
ESA	European Space Agency
GFED	Global Fire Emission Dataset
GLW	Gridded Livestock of the World
GPW	Gridded Population of the World
GPP	Gross Primary Productivity
GSV	Growing Stock Volume
IAV	Inter-annual variability
L-VOD	Low-frequency Vegetation Optical Depth
LAI	Leaf Area Index
LSM	Land Surface Model
LU	Land Use
MAP	Mean Annual Precipitation
NDE	Nitrogen deposition
NPP	Net Primary Productivity
NSD	Normalized standard deviation
PC	Principal Component
PCA	Principal Component Analysis
PFT	Plant Function Type
SAR	Synthetic Aperture Radar
SD	Standard Deviation
SE	Standard Error
SLA	Specific Leaf Area
SMOS	Soil Moisture and Ocean Salinity
VPD	Vapor Pressure Deficit

	Ref	CCI Biomass Climate Assessment Report v3		
	Issue	Page	Date	
	3.0	11	14.07.2021	

1. Biomass in Climate Models



Biomass is an essential variable in the Earth System, as it is an important storage pool for carbon (C) removed from the atmosphere by land carbon sinks, and thus its accumulation of carbon over time mitigates climate warming. The current land sink of atmospheric CO₂ in natural ecosystems absorbs on average about 30% of fossil fuel emissions, and most of the storage of this excess carbon removed from the atmosphere is in biomass (Friedlingstein et al., 2019). Forests hold the largest biomass pool on Earth, about 80% of all the biomass stocks, in particular tropical forests. According to a global analysis of forest carbon stocks and carbon stocks changes (Pan et al., 2011), based on inventory data and long-term field observations, the forest carbon sink is nearly equivalent in magnitude to the global land carbon sink.

Nevertheless, biomass is not just a static repository of carbon. Dynamical variations of the biomass pools relate to 1) the process of total photosynthesis, whose product (GPP) is the carbon input, 2) the fraction of the assimilated carbon from GPP to plant (non-assimilated carbon is used for plant respiration), 3) the allocations of the assimilated carbon into sapwood and soft tissues like leaves and fine roots, 4) the conversion from sapwood into structural heartwood, 5) plant mortality processes, which lead to biomass losses through a number of factors: fires, drought, individual mortality, competition for resources.

Carbon cycle models, an important part of Earth System Models (ESMs), were developed to account for CO₂ fluxes exchanged between ecosystems and the atmosphere (Sellers et al., 1996). The importance of carbon stocks in models was recognized when the first study of carbon-climate feedbacks (Cox et al., 2000) showed that the large biomass pool of the Amazon forest was vulnerable to climate drying and warming, as in their simulation, the entire forest collapsed by 2100, causing a huge loss of CO₂ into the atmosphere. This result has raised a lot of research about the stability of tropical forest biomass, and different ESMs have been applied to solve this question, showing contrasting results (Phillips et al., 2009; Malhi et al., 2009; Rammig et al., 2010; Huntingford et al., 2013). These studies show that most ESMs retain stable tropical forests in the Amazon, although some regions have a decrease of biomass in response to drought and increased fire.

The understanding and quantification of biomass in ESMs, more precisely in land surface models that are part of ESMs, depend on simulation of plant productivity and respiration, which determine the ratio between Gross Primary Productivity (GPP) and Net Primary Productivity (NPP). This ratio is called carbon use efficiency (CUE), or the fraction of GPP used for biomass production, that is, biomass production efficiency (BPE). The simulation of biomass also relates to the carbon allocation schemes and parameterization of plant mortality in models. We summarize below the recent research results related to the evaluation and uncertainty of land carbon cycle models with respect to each of these processes.



We consider both coupled ESMs and offline dynamic global vegetation models (DGVMs). For the coupled ESMs, the carbon cycle and the computation of biomass are coupled with ESM-simulated climate, whereas the offline DGVMs are driven by the observed gridded climate fields or ESM-predicted future climate fields. For the historical period, the most widely used ensemble of DGVM models is from the TRENDY project, in which currently 15 DGVMs are driven by reconstructed climate, observed atmospheric CO₂ and land use land cover data, to assess the annual budget of CO₂ (Le Quéré et al., 2018). Another project called MstMIP project (Huntzinger et al., 2013) also gathers coordinated runs from a larger ensemble of DGVMs, including a set of factorial global simulations considering nitrogen deposition influences, but all the simulations from MstMIP only cover the period up until 2010. For the future, the offline DGVMs have been run to predict biomass and other carbon cycle

	Ref	CCI Biomass Climate Assessment Report v3		
	Issue	Page	Date	
	3.0	12	14.07.2021	



variables in the ISIMIP-Phase2-b project (ISIMIP2b modelling protocol on the website, <https://www.isimip.org/protocol/#isimip2b>) where the climate drivers are from four CMIP5 ESMs with a bias correction to adjust climate fields to observations in the period 1961-1990 (Frieler et al., 2017). Climate projections for the low-emissions Representative Concentration Pathway RCP2.6 and no-mitigation pathway RCP6.0 are used to drive different DGVMs. In the ISIMIP-Phase3 the same DGVMs will be driven by the bias-corrected output of CMIP6 models used in the upcoming 6th IPCC Assessment Report (see Outcome of the ISIMIP Strategy Group Meeting 2018; <https://protocol.isimip.org/>).

Table 1-1: A brief summary of global model ensembles

Project name	Models participating in	Time period	Forcing data*	Reference
TRENDY v8	CABLE, CLASS-CTEM, CLM5.0, DLEM, ISAM, ISBA-CTRIIP, JSBACH, JULES-ES, LPJ-GUESS, LPX-Bern, OCN, ORCHIDEE, ORCHIDEE-CNP, SDGVM, VISIT	1901-2018	CLIM: CRU-NCEP v8; CO2: NOAA LU: Hurtt's Soil&NDE: model group use its own data;	Le Quéré et al. (2018)
MsTMIP	Biome-BGC, CABLE-JPL, CABLE, CLASS-CTEM-N+, CLM, CLM4-VIC, DLEM, ECOSYS, GTEC, HYLAND-JPL, ISAM, JULES-JPL, LPJ-wsl, MC1, ORCHIDEE-JPL, ORCHIDEE-LSCE, SiB3-JPL, SiBCASA, TEM6, TRIPLEX-GHG, VEGAS, VISIT	1901-2010	CLIM: CRU-NCEP; CO2: Enhanced GlobalView; NDE: Enhanced Dentener; Soil: HWSD; LU: Hurtt's + SYNMAP	Huntzinger et al. (2013)
CMIP5	ACCESS1.0, ACCESS1.3, BCC-CSM1.1/-CSM1.1m, BNU-ESM, CanCM4,	Historical: 1860-2005	CO2: NOAA Other GHGs and aerosol: IIASA	Taylor et al. (2012)

	Ref	CCI Biomass Climate Assessment Report v3		
	Issue	Page	Date	
	3.0	13	14.07.2021	

	CanESM2, CCSM4, CESM1-BGC/-WACCM/-FASTCHEM/-CAM5/-CAM5.1-FV2, CMCC-CM/-CMS/-CESM, CNRM-CM5, CSIRO-Mk3.6.0, EC-EARTH, FDOALS-g2, FGOALS-s2, FIO-ESM, GFDL-ESM2M/-ESM2G/-CM2.1/-CM3, GISS-E2-R/-E2-H/-E2-R-CC/-E2-H-CC, HadGEM2-ES/-CC/-AO, HadCM3, INM-CM4, IPSL-CM5A-LR/-CM5A-MR/-CM5B-LR, MIROC4h, MIROC5, MIROC-ESM/-ESM-CHEM, MPI-ESM-LR/-ESM-MR/-ESM-P, MRI-EMS1/-CGCM3, NCEP-CFSv2, NorESM1-M/-ME	Future: 2006-2100	LU: LUH2	
ISIMIP2a	CARAIB, DLEM, JULES-B1, LPJ-GUESS, LPJmL, ORCHIDEE, VEGAS, VISIT	1901-2012	CLIM: GSWP3, WATCH, PGMFD CO2: NOAA LU: Hyde 3.0 NDE: ACCMIP	Chang et al. (2017)
ISIMIP2b	CARAIB, CLM4.5, DLEM, JULES-B1, LPJ-GUESS, LPJmL,	Historical: 1861-2005 Future:	CLIM: CMIP5 CO2: NOAA	Frieler et al. (2017)

	Ref	CCI Biomass Climate Assessment Report v3		
	Issue	Page	Date	
	3.0	14	14.07.2021	



	ORCHIDEE-DGVM, VEGAS, VISIT	2006-2100	LU: Hyde 3.2 NDE: ACCMIP	
ISIMIP3a	CARAIB, CLM4.5, DLEM, JULES-B1, LPJ- GUESS, LPJmL, ORCHIDEE-DGVM, VEGAS, VISIT, et al.	1901-2018	CLIM: GSWP3, GSWP3-W5E5 CO2: NOAA LU: Hyde 3.2 NDE: NCAR CCMI	https://protocol.isimip.org/
ISIMIP3b	CARAIB, CLM4.5, DLEM, JULES-B1, LPJ- GUESS, LPJmL, ORCHIDEE-DGVM, VEGAS, VISIT, et al.	Historical: 1850-2014 Future: 2015-2100	CLIM: CMIP6 CO2: NOAA LU: Hyde 3.2 NDE: NCAR CCMI	https://protocol.isimip.org/

* CLIM = climate, LU = land use, NDE = nitrogen deposition.

2. Processes controlling the dynamics of biomass

2.1. Gross Primary Productivity

A recent analysis of CMIP5 model results by Koven et al. (2015) suggests that in ESMs, the change of biomass stocks in the future is controlled mainly by changes of GPP and not by changes of mortality, because most ESMs do not contain processes representing the effects of disturbances, water stress or stand competition on mortality. Therefore, it is important for biomass simulation to first assess the simulation of GPP. Anav et al. (2013) evaluates the ability of CMIP5 models to simulate GPP against FLUXNET site-level observations using a model tree ensemble (MTE) upscaling approach (MTE-GPP, Jung et al. 2011). For the global averages, all the models overestimate the global mean GPP over the period 1986–2005, which is not due to bias in climate variables, although precipitation is the main driving factor for photosynthesis across the globe, temperature being mainly limiting in northern high latitudes (Piao et al., 2009). Other reasons explain the systematic overestimation of global mean GPP in all the CMIP5 models: first, most of these models do not consider nutrient limitation on GPP (Zaehle et al., 2010; Goll et al., 2012); second, the parameterization of the impact of tropospheric ozone on reducing GPP (Sitch et al., 2007; Witting et al., 2009) is not yet implemented in the models. A further evaluation of global mean GPP simulated by DGVMs forced offline by observed climate (i.e., CRU-NCEP) also confirms that the land surface components of the CMIP5 ESMs still overestimate the GPP when forced by observations. For the inter-annual variability (IAV) of GPP, no model can capture the IAV of the MTE-GPP in the tropics and in the Northern Hemisphere, and all models simulate larger GPP IAV than the one given by the MTE-GPP. However, it should be noted that there are substantial doubts

	Ref	CCI Biomass Climate Assessment Report v3		
	Issue	Page	Date	
	3.0	15	14.07.2021	

about the quality of the MTE-GPP product regarding the magnitude of inter-annual variability, particularly in the tropics, because no FLUXNET sites in the tropics are used to train the MTE-GPP product, and machine learning algorithms use the information on spatial variability of the FLUXNET data to construct the IAV (Anav et al., 2013).



2.2. Carbon use and biomass production efficiency

Carbon use efficiency (CUE) is the ratio of net primary production (NPP) to GPP, and biomass production efficiency (BPE) is the fraction of GPP used for biomass production (BP) of terrestrial ecosystems. CUE is not directly measurable, because NPP comprises BP and the production of non-structural organic compounds, the latter used to maintain functions of the rhizosphere and plant (e.g., mycorrhizae, root exudates, and volatile carbon compound emissions) which cannot be measured directly (Chapin et al., 2006; Vicca et al., 2012; Campioli et al., 2015). In contrast, BP, which is photosynthetically-derived carbon used for biomass growth (i.e. build-up of leaves, wood and roots), is measurable with biometric observations. A large fraction of BP is being appropriated by humans through the harvest of food (Haberl et al., 2007; Erb et al., 2016). Currently non-harvested BP drives a carbon sink in biomass.

Carbon cycle models have not been rigorously evaluated for BP due to the lack of adequate measurements. However, the compilation of large databases of GPP and BP components for forests (Luyssaert et al., 2007) and for other vegetation types (Campioli et al., 2015) allowed evaluation of the distribution of BPE across biomes. Piao et al. (2010) suggest that the BPE is a hump-shaped function of mean annual temperature that peaks at values of 10°C in southern boreal and temperate forests and decreases to ~0.15 in tropical and northern boreal forests. Fernández-Martínez et al. (2014) also find that BP in forests was controlled by soil nutrient availability, with more fertile forests having a large rate of biomass production and NPP relative to GPP, possibly because of less carbon investment costs for maintenance purposes, in particular root tissues. Campioli et al. (2015) show that BP across vegetation types is a function of management, with managed systems being more efficient at converting GPP carbohydrates to biomass. He et al. (in review) presents a new global estimation of BPE obtained by combining field measurements from 113 sites with 14 DGVMs. Their best estimate of global BPE was 0.41 ± 0.05 . The largest BPE was found in boreal forests (0.48 ± 0.06) and the lowest in tropical forests (0.40 ± 0.04). DGVMs from the MstMIP ensemble tend to overestimate BPE, although models with carbon-nitrogen interactions were more realistic. Overestimation of BPE may imply an overestimation of carbon input to biomass pools, but the most important process that discriminates biomass simulation in models is how NPP is allocated to woody and soft tissues pools, because the latter have a fast turnover rate and cannot be a large permanent storage pool of carbon in the Earth system.

2.3. Allocation of net primary productivity to biomass pools

Negrón-Juárez et al. (2015) show that CMIP5 ESMs have limitations in modelling the carbon allocation of net primary production which propagates to errors in biomass estimates from CMIP5 ESMs. More recently, Xia et al. (2019) examine the NPP allocation response to variations in temperature or precipitation and find that carbon allocation is often opposite in leaves and fine roots, which is consistent with the functional balance theory for allocation. They also find that the observed allocation to fine roots decreases with increasing temperature and precipitation. The observed NPP allocation to wood and leaves decreases with forest stand age. Compared with the observations, the simulated NPP allocation estimates from five TRENDY DGVMs show the same spatial gradient of lower NPP allocation

	Ref	CCI Biomass Climate Assessment Report v3		
	Issue	Page	Date	
	3.0	16	14.07.2021	



to fine roots with increasing temperature and precipitation but different spatial gradients of NPP allocation to wood and leaves. None of the five models adequately represents the changes in allocation with forest stand age. Specifically, the models cannot reproduce the decrease in NPP allocation to wood and leaves and the increase in allocation to fine roots with increasing forest stand age. Therefore, an accurate simulation of NPP allocation and biomass requires more realistic representation of multiple processes that are closely related to allocation.

2.4. Mortality

Regarding mortality, at the scale of a single tree, tree biomass develops during the tree lifetime and is transformed to litter when the tree dies. During the lifetime of a tree, leaf and fine root biomass are also continually dying given their short turnover times, and provide carbon input to soil organic carbon pools. Compared to the leaves and fine roots, branches have longer turnover times. Thus, vegetation mortality, at the scale of a single tree, can vary depending on the turnover time of these tissue carbon pools.

At the scale of a population of trees (i.e. forest ecosystem), at any given point in time, the amount of biomass not only depends on the woody growth of all individual trees, but also on competition between trees for resources such as light, water and nutrients. At a critical tree density, light competition is exacerbated and tree mortality can occur due to crowding, usually leading to the smallest trees dying. Competition causes more self-thinning, which generally is reflected by a power law relationship between the mean size of individual trees and the tree density in the stand. But in tropical forests, particularly in productive forests where the growth rates of individual trees is high, competition between trees is very severe, and tropical forests tend to show deviations from the power law relationship for the dominant trees (Farrior et al., 2016). This suggests that it is mainly understory trees, not canopy trees, that engage in competition under strong light limitation. In addition to competition-induced mortality, individual trees can die after a certain lifespan or when they face natural enemies. A study by Stephens et al. (2007) suggests that the highest ecosystem biomass is not achieved in tropical forests, where the rate of vegetation growth is the highest. This is because in tropical forest mortality induced by natural enemies is very high, whereas in temperate regions where vegetation growth rate is relatively low, mortality is much less intense. Most of the current DGVMs use a fixed mortality rate when they simulate biomass as well-mixed carbon pools, and do not describe dynamic mortality processes associated with competition. However, mortality in LPJ-GUESS, LPJmL, OCN and SDGVM accounts for competition among trees for resources (Walker et al. 2015; Thurner et al. 2017). In SDGVM, mortality via self-thinning is a result of competition between cohorts within each individual plant functional type (PFT), under the constraint that NPP must be sufficient to maintain a minimum stem diameter increment, otherwise stem density would reduce. In LPJ-GUESS, LPJmL and OCN, competition for light and water is considered by using a canopy cover upper threshold, i.e. if canopy cover exceeds a threshold ratio to ground area, stem density would reduce.

Last but not least, a large fraction of biomass mortality is induced by disturbances. Disturbances range from small scale mortality events in response to biotic factors to larger scale ones from windthrow (Bouget and Duelli, 2004), fires (Brando et al., 2012), insects and pathogens (Das et al., 2016), and climate warming or drying altering the eco-physiological functioning of forests. Biomass losses also occur from climate-induced and natural disturbances. Allen et al. (2010) examine more than 150 references that document 88 examples of forest mortality induced by climatic water/heat stress since 1970. Such climate-induced mortality events span a broad gradient of woody ecosystems, from monsoonal savannas to subalpine conifer forests, and to tropical rainforests. In savanna, extreme multi-year droughts (more than 3 years) can cause substantial tree death associated with prolonged

	Ref	CCI Biomass Climate Assessment Report v3		
	Issue	Page	Date	
	3.0	17	14.07.2021	



water deficits (Fensham et al., 2009). In temperate forests, extreme seasonal droughts may be more likely to induce dieback of deciduous broadleaved forest due to xylem cavitation (Maherali et al., 2004). In tropical rainforests, short but extreme droughts can cause relatively diffuse mortality; for example, tree mortality rate in Indonesia reached 26% after the severe El Niño in 1997/1998 (Van Nieuwstadt and Sheil, 2005). More recently, Anderegg et al. (2019) developed a set of early warning metrics for drought-induced tree mortality using Landsat satellite data. These early warning metrics predict the tree hydraulic stress and mortality during the droughts in the southwestern US and in tropical forests. In addition, Thurner et al. (2016) suggest that mortality in temperate and boreal forests can be explained by different climate-related processes: tree mortality in temperate forest is associated with the enhanced risk of insects and pathogens during droughts, whereas frost damage can explain the tree mortality in boreal forest. Thurner et al. (2017) highlight discrepancies in simulating loss processes from mortality in DGVMs, i.e., the mortality process is usually modeled using rather simple assumptions. Mortality induced by fires, windthrow, insects, diseases, extreme drought and frost damage is not accounted for in the current generation of DGVMs. In addition, recent studies for the tropics show that incorrect modeling of mortality processes in DGVMs and ESMs tends to cause exacerbated discrepancies in simulating biomass (Delbart et al., 2010; Ahlström et al., 2017). Therefore, improvement in our current understanding and more accurate prediction of tree mortality are critically needed.

2.5. Land use change and harvest affecting biomass

Biomass is not only vulnerable to climate disturbance but also to human disturbances. Today a large percentage of the global forests is harvested, so that the laws of natural mortality controlling the biomass of forests are bypassed by economic processes and human drivers, such as the demand for wood for fuel or materials. This is another challenge for DGVMs as it implies that they must include forest management, not only for wood removal but also for the recovery of forest biomass after human disturbance. Human-driven land use and land cover change dynamics are estimated to impose ~50% reductions in forest carbon stocks at the global scale (Erb et al., 2018). Using a book-keeping approach, these estimates of total cumulative emissions from land use change (since early human activities) range from 375 to 525 PgC (Erb et al., 2018). In comparison, the DGVMs from the TRENDY v2 model ensemble, in which human perturbation of land use may have started in 1850, find a cumulative carbon loss of only one third of Erb's estimate (155 ± 50 PgC; Li et al., 2017). Possible reasons for this large discrepancy include: (1) the book-keeping approach tends to overestimate the pre-industrial biomass stocks in forests; (2) early human activities may already have significantly reduced biomass stocks by 1850, which is plausible because of the use of biomass as a primary source of energy in pre-industrial human societies, and the large per capita biomass appropriation rates reconstructed from pre-historical and historical studies; (3) DGVMs used in Li et al. (2017) only account for biomass losses from forest area loss, but the impacts of forest management and the gathering of litter and fuelwood by local communities are not included.

2.6. Turnover times

The concept of turnover time of carbon in the biosphere is key to understanding the relationship between biomass (carbon stock) and carbon sinks. The term turnover time commonly refers to the ratio of the carbon stock of a pool to its outgoing flux (Bolin and Rhode, 1973; Sierra et al., 2010). Realistic dynamic turnover time (τ) in biomass (used in Cantú et al., 2014) that accounts for changes in vegetation carbon stocks (dCS) and in NPP, as given by:



	Ref	CCI Biomass Climate Assessment Report v3		
	Issue	Page	Date	
	3.0	18	14.07.2021	

$$dCS/dt = NPP - CS/\tau$$

Bolin and Rhode (1973) show that for well-mixed pools, the turnover time is equal to the mean age of carbon in each pool, and that the turnover time of carbon atoms follows an exponentially decreasing distribution. However, since mortality (or respiration for soil carbon) is usually not available as gridded observation-based data, for global estimates of turnover input fluxes (GPP or NPP) have been used in some studies (e.g. Carvalhais et al., 2014) instead of outgoing fluxes, which is based on an additional near-equilibrium assumption that NPP approximates to mortality. This assumption is broadly correct at large spatial scales where NPP and mortality are far greater than the net carbon stock change, but it breaks down at plot scale where the change in stock is a significant fraction of NPP, for example in a growing forest. Processes controlling the turnover times of carbon have been shown to be the least certain, determining the differences between different DGVM models, in projections of the future carbon cycle in forests (Friend et al. 2014). The feedback between the terrestrial carbon cycle and climate is also partly dependent on changes in the turnover time of carbon in land surface ecosystems.

The turnover time is not an independent process but rather is an ecosystem property that emerges from the interplay between productivity, carbon use efficiency, carbon allocation and mortality processes. It is generally controlled by climate (that has an influence on all those processes, as explained above), vegetation types, as well as appropriation of NPP and biomass induced by human land-use (Erb et al., 2016). A spatially explicit and observation-based assessment of whole-ecosystem, biomass and soil carbon turnover times was proposed by Carvalhais et al. (2014), based on GPP derived from eddy covariance flux towers, satellite-based above-ground biomass, and soil carbon data from ground surveys extrapolated to carbon down to 3m depth. They estimate the overall mean global carbon turnover time is 23 years (19 to 30 years at 95 % confidence interval). On average, carbon has a longer turnover time in vegetation and soil near the Equator, and a shorter time in northern latitudes. Mean turnover times vary from 15 to 255 years from the tropics to the northernmost latitudes. Carvalhais et al. (2014) also show a strong dependence of turnover time not only on temperature, as expected from our present understanding of temperature controls on ecosystem dynamics, but also on precipitation. The ecosystem carbon turnover times simulated by CMIP5 ESMs vary widely, and these models, on average, tend to underestimate the global carbon turnover time by 36%. Compared to observation-based estimates, CMIP5 ESMs show stronger spatial relationships between turnover times and temperature, and cannot reproduce the relationships between turnover times and precipitation. This misrepresentation would probably explain why CMIP5 ESMs tend to predict much faster carbon turnover in many semi-arid regions.

Reichstein et al. (2019) further review turnover times in biomass and find that CMIP5 ESMs have a low correlation between the modeled and the observed turnover time of carbon in vegetation ($\tau = \text{biomass}/\text{GPP}$; Carvalhais et al., 2014), although their GPP and biomass estimates show good overall agreement with the observations. They also find that, in CMIP5 ESMs, the correlation between the modelled turnover time and tree cover fraction is significant and positive, that is, tree biomes are expected to have a longer turnover time in biomass, though this correlation can vary among models, ranging from 0.50 (INMCM4) to 0.88 (MPI-ESM- LR). They applied a linear regression to biomass and GPP, and the slope of regression is carbon turnover time. They found the regression results for model and data are quite different. A possible reason is that CMIP5 ESMs did not well consider the impacts of the extent of NPP derived from GPP, carbon allocation strategies, and mortality dynamics on turnover times. However, their analysis could not further quantify the relative contributions of the biases in CUE (or BPE), carbon allocation strategies, or mortality schemes. But CUE differences seemed to co-vary to some extent with turnover time differences between models, which implies the importance of understanding both the controls of carbon allocation and autotrophic respiration in predicting turnover time, not only a possibly wrong NPP-GPP relation in those models.

	Ref	CCI Biomass Climate Assessment Report v3		
	Issue	Page	Date	
	3.0	19	14.07.2021	

3. Evaluation of biomass in carbon cycle models



Estimates of the global distribution of forest above-ground biomass (AGB) have been produced (Table 3.1) using sample plots from forest inventories (Pan et al., 2011) combined with remote sensing observations (Liu et al., 2015). In addition, a number of biome-specific datasets have been published, all characterized by large uncertainties at local scale (Mitchard et al., 2013). Unfortunately, none of these datasets is suitable for evaluating global model outputs either because they are not truly global (e.g. AGB from GEOCARBON project) or have coarse resolution (e.g. AGB from Liu et al. 2015). Yet, substantial advances towards the generation of global datasets of AGB density from remote sensing observations have been made in recent years to support such types of evaluation.

The dataset of AGB density in 2017 produced in CCI Biomass and based on multiple remote sensing observations and in situ measurements, is deemed to be suitable to evaluate global model outputs, because (1) it covers a fixed epoch circa 2017-2018 for all the tropical, temperate and boreal regions; (2) it has been evaluated against in situ data at various scales and appears to provide a reliable spatial characterization of AGB density; (3) it is available at a spatial resolution of 100 m, much finer than other published datasets of AGB density, allowing a precise calculation of biomass density per forest area to match model output; (4) it comes with per-pixel estimates of AGB density uncertainty and error spatial correlation structure, allowing us to aggregate uncertainty from 100 m to the spatial resolution of global models, typically 0.5°.

The previous GlobBiomass dataset of AGB density was estimated from GSV derived from spaceborne Synthetic Aperture Radar (SAR), LiDAR (Light Detection And Ranging) and optical remote sensing observations for the year 2010 in a multi-model retrieval framework. The GlobBiomass retrieval algorithm is the starting point for the development of the CORE retrieval algorithm used in CCI Biomass. For CCI Biomass, vegetation heights are included in the retrieval models and allometries between height and biomass are used to directly map the biomass instead of GSV. The estimation of AGB was supported by forest inventory datasets, additional remote sensing data products and climatological variables (Santoro et al., 2018; Santoro et al., in preparation). Forest AGB density and retrieval error was generated at the highest spatial resolution of the remote sensing datasets, i.e., 25m. However, the large uncertainty of 25 m pixel estimates due to imperfections in the remote sensing data and the weak sensitivity of the data to biomass, suggested provision of spatially explicit estimates of AGB density at an aggregated scale of 100 m. The 100 m standard deviation (SD) of AGB density from the CCI Biomass data set is obtained by propagating individual uncertainties of the remote sensing measurements, retrieval model parameters and ancillary data sets (see details in ATBD), which are at most 30% at 100 m spatial resolution.

Table 3-1: A brief summary of different regional/global above-ground biomass datasets.

Regions	Approaches	Study epoch	Spatial resolution	References /Sources
Global	SAR image-based growing stock volume, which is converted to global AGB carbon	2010	100m × 100m	GlobBiomass Santoro et al. (2018)
	SAR image-based AGB carbon using CCI CORE retrieval algorithms	2017	100m × 100m	CCI Biomass
	C-band Passive microwave-based global AGB carbon	1993-2012	0.25o × 0.25o	C-VOD AGB Liu et al. (2015)
	L-band Passive microwave-based global AGB carbon	2010-2019	0.25o × 0.25o	L-VOD AGB Fan et al. (2019)
	A global forest biomass dataset generated from three existing biomass maps. Tropical: Saatchi + Baccini Temperate + Boreal: Santoro	Saatchi: 2000 Baccini: 2007/8 Santoro: 2010	0.01o × 0.01o	GEOCARBON
	Forest inventory data-based; including above and below ground biomass	1990-2007	Global/ regional averages	Pan et al. (2011)
Tropical	A combination of forest inventory data and satellite Lidar samples of forest structure	2000	0.01o × 0.01o	Saatchi et al. (2011)

	Ref	CCI Biomass Climate Assessment Report v3		
	Issue	Page	Date	
	3.0	21	14.07.2021	

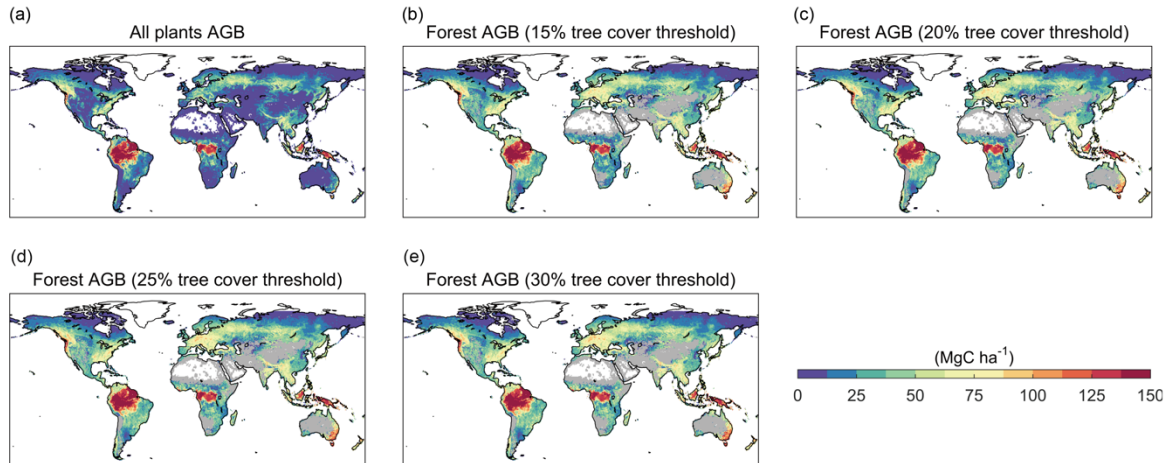




Figure 3-1: Spatial patterns of 0.5-degree above-ground biomass circa the year 2017 derived from the CCI Biomass product, defined by tree cover thresholds of 0%, 15%, 20%, 25% and 30%.

To be consistent with the spatial resolution of the majority of the DGVMs, the estimates of AGB density and its standard error from CCI Biomass were aggregated to 0.5 degree. The original CCI Biomass data were provided for each 100 m pixel regardless of land-cover type, thus, to estimate the 0.5° AGB values for all plants and forest, we first label each 100 m pixel of ‘forest’ using the Hansen tree cover map (Hansen et al., 2013), depending whether the tree cover is above or below a given threshold, respectively. We then calculate an average of all AGB values labelled as ‘forest’ within the averaging spatial window of 0.5° × 0.5°. Five different thresholds of tree cover fraction of 0%, 15%, 20%, 25% and 30% are used in aggregating AGB per forest area at 0.5° (Figure 3.1). Here, using the tree cover threshold of 0%, we obtain the 0.5-degree AGB density for all plants, while we obtain the 0.5-degree AGB density for forests using the thresholds of 15%, 20%, 25% and 30%. Additionally, considering the error covariance in the GlobBiomass data, the SE of the average of AGB at 0.5° is calculated as

$$\delta(AGB_{0.5d})^2 = \frac{1}{N^2} \cdot \sum_{i=1}^N \delta(AGB_i)^2 + \frac{2}{N^2} \cdot \sum_{i=1}^{N-1} \sum_{j=i+1}^N Cov(\delta AGB_i, \delta AGB_j)$$

where $Cov(\delta AGB_i, \delta AGB_j)$ is the covariance of errors between the estimates of AGB from pixel i and pixel j within the averaging window. As shown in Figure 3.1 and 3.2, the spatial patterns of 0.5-degree AGB density and forest area are quite different based on different thresholds of tree cover fraction.

In addition, biomass density data, originally in units of Mg ha⁻¹, were converted to biomass carbon density (Mg C ha⁻¹) using a factor of 0.5 (Baccini et al., 2012; MacDicken, 2015).

	Ref	CCI Biomass Climate Assessment Report v3		
	Issue	Page	Date	
	3.0	22	14.07.2021	

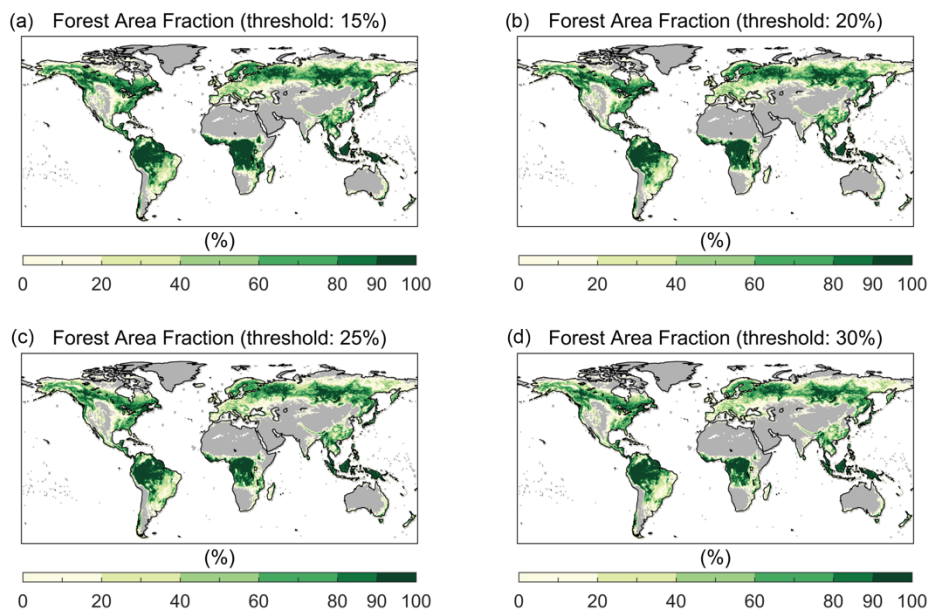


Figure 3-2: Spatial patterns of 0.5-degree forest area, defined by tree cover thresholds of 15%, 20%, 25% and 30%.

3.1. Materials and methods

3.1.1. Modelling biomass in global climate/carbon process-based models

TRENDY DGVMs

DGVMs from the TRENDY v8 project (Sitch et al., 2015) include CABLE, CLASS-CTEM, CLM5.0, DLEM, ISAM, ISBA-CTRIP, JSBACH, JULES-ES, LPJ-GUESS, LPX-Bern, OCN, ORCHIDEE, ORCHIDEE-CNP, SDGVM and VISIT (Table 3.2). All the models provided the ‘cVeg’ output, which is the total living biomass for all plant functional types (PFTs), and 8 out of 15 models provided the ‘cVegpft’, which can be used to calculate forest biomass per forest area. These models are driven by observation-based climate forcing data to reconstruct land carbon changes since 1850, and simulated land-use change emissions and biomass loss from a global harmonized land cover change dataset. In all the simulations, the climate forcing is from the CRU-NCEP v8 dataset (Viovy, 2018), including precipitation, snowfall, temperature, short-wave and long-wave radiation, specific humidity, air pressure, and wind speed at 6h resolution and for the years 1901–2018.

TRENDY DGVMs perform three factorial simulations, S3, S2 and S1 with time-varying climate, CO₂, and land-use forcings turned on or off over the historical period. Simulation S3 is driven with changes in all forcings. The changes in forest biomass and historical forest area in this simulation are the net result of the expansion of cropland and pasture, and afforestation or forest regrowth following abandonment, together with the effects of changes in observed CO₂ and climate over the historical period. Simulation S2 is driven with changes in only the climate and CO₂ over the historical period but the land cover is specified corresponding to year 1860. Finally, simulation S1 is driven with only the increase in CO₂ over the historical period while climate change and land-use change correspond to pre-industrial conditions. These simulations allow us to isolate the individual contributions of elevated CO₂ concentration (S1), climate change (S2 minus S1) and land-use change (S3 minus S2) over the historical period. The historical land-use change maps are from the LUH2v2h reconstruction (Hurtt et



al., 2011), the 1901–2018 climate forcing are from CRU-NCEP v8 data set (Viovy, 2018) which include precipitation, snowfall, temperature, short-wave and long-wave radiation, specific humidity, air pressure and wind speed at 6h temporal resolution. A short summary of processes included in each model that impact biomass is given in Table 3.2, as well as the number of different vegetation types defined as forest in each model.

Table 3-2: A brief description of 15 DGVMs from the Trendy v8 project.

Models	Number of Forest PFTs	Carbon-nitrogen interaction	Wood harvest and forest degradation	Fire as a management tool	Shifting cultivation	Resolution
CABLE	4	N	Y	N	Y	1° × 1°
CLASS-CTEM	5	N	N	N	N	2.8125° × 2.8125°
CLM5.0	-	Y	Y	N	N	0.9524° × 1.25°
DLEM	-	Y	Y	N	N	0.5° × 0.5°
ISAM	14	Y	Y	N	N	0.5° × 0.5°
ISBA-CTrip	-	N	N	N	N	1° × 1°
JSBACH	4	Y	Y	N	Y	1.875° × 1.875°
JULES-ES	2	N	N	N	N	1.875° × 1.25°
LPJ-GUESS	10	Y	Y	N	Y	0.5° × 0.5°
LPX-Bern	8	Y	N	N	N	0.5° × 0.5°
OCN	-	Y	Y	N	N	1° × 1°
ORCHIDEE	8	N	Y	N	N	0.5° × 0.5°
ORCHIDEE-CNP	8	Y	N	N	N	2° × 2°
SDGVM	-	Y	N	N	N	0.5° × 0.5°
VISIT	-	N	-	-	-	0.5° × 0.5°

According to the TRENDY protocol the biomass simulated by a DGVM is provided as total biomass, including above- and belowground pools. Before further analysis, total biomass outputs from all the models are first remapped to the same spatial resolution of 0.5° × 0.5°. Following Liu et al. (2015), we use biome-specific ratios of total and AGB carbon (i.e. 1.24 for the boreal and temperate forests; 1.26 for the tropical forests) to infer AGB in order to match the GlobBiomass AGB data. Specifically, the values of forest AGB density (AGB, gC/ha) and forest area (A, ha) are calculated as:

$$AGB = \frac{\sum_{i=1,2,\dots} \beta \times b_i \times f_i}{\sum_{i=1,2,\dots} f_i}$$

	Ref	CCI Biomass Climate Assessment Report v3		
	Issue	Page	Date	
	3.0	24	14.07.2021	

$$A = \sum_{i=1,2,\dots} a_i \times f_i$$

where β is the ratio of above-ground to total biomass, b_i (MgC ha^{-1}) is forest PFT-specific above-ground biomass, a_i (ha) is the area of the grid cell, and f_i is the land cover fraction of the i th PFT provided by the individual DGVM. In addition, we also evaluate the biome mean forest AGB from DGVMs. Global forest AGB is split into the six climate zones of the Köppen-Geiger climate classification: tropical wet, tropical dry, arid, temperate, boreal and polar (Figure 3.3).

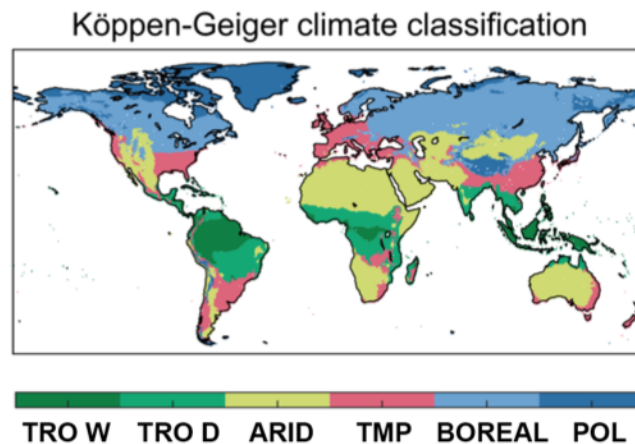


Figure 3-3: Map of six Köppen-Geiger climate biomes. TRO W = wet tropical, TRO D = dry tropical, ARID = arid, TMP = temperate, BOREAL = boreal, POL = polar.

CMIP5 ESMs

We have collected monthly biomass outputs from CMIP5 ESMs during AGB observation epochs from the IPCC data distribution center. In ESMs, biomass is simulated by land surface models coupled with climate models. In addition, we plan to use available AGB outputs of the CMIP6 ESMs that will provide simulations to the upcoming IPCC exercise during the course of the project. The evaluation of CMIP5 and CMIP6 models is not presented here given their larger uncertainty due to uncertainty in climate drivers but will be provided in a future version of the CAR.

3.2. Evaluation of DGVMs using CCI Biomass dataset

3.2.1. Global and Biome estimates

Figure 3.4a compares the global mean all plants AGB and forest AGB for 2017 from the CCI Biomass dataset and the 15 DGVMs. The AGB of each DGVM stems from the Trendy v8 S3 simulation (driven by varying CO_2 , climate change and land-use change). The global all plants AGB from the CCI Biomass dataset is 328 PgC, but all DGVMs predict lower global AGB for all PFTs, except for the DLEM model. The average global AGB from the 15 DGVMs is 230 ± 63 PgC, the spread corresponding to the 1-sigma standard deviation between models, while the individual value ranges from 153 PgC in JSBACH to 363 PgC in DLEM. The global forest AGB from the CCI Biomass dataset varies slightly from 263 to 278 PgC, corresponding to an increase of 6%, for decreasing tree cover thresholds (from 30% to 15%) used to define forest area (Figure 3.4a). The global forest area is more sensitive to the choice of the threshold (Figure 3.4b), with an increase of 15% (when applying the 30% vs. 15% tree cover threshold). The forest

AGB from the eight DGVMs (excluding ORCHIDEE) is 195 ± 71 PgC, the spread corresponding to the 1-sigma standard deviation between models. The global forest AGB from the CLASS-CTEM, ORCHIDEE-CNP and JULES-ES models is very close to the CCI Biomass estimates. We found the “cVegpft” output from the ORCHIDEE model to be faulty, so the results of ORCHIDEE are excluded from the analysis.

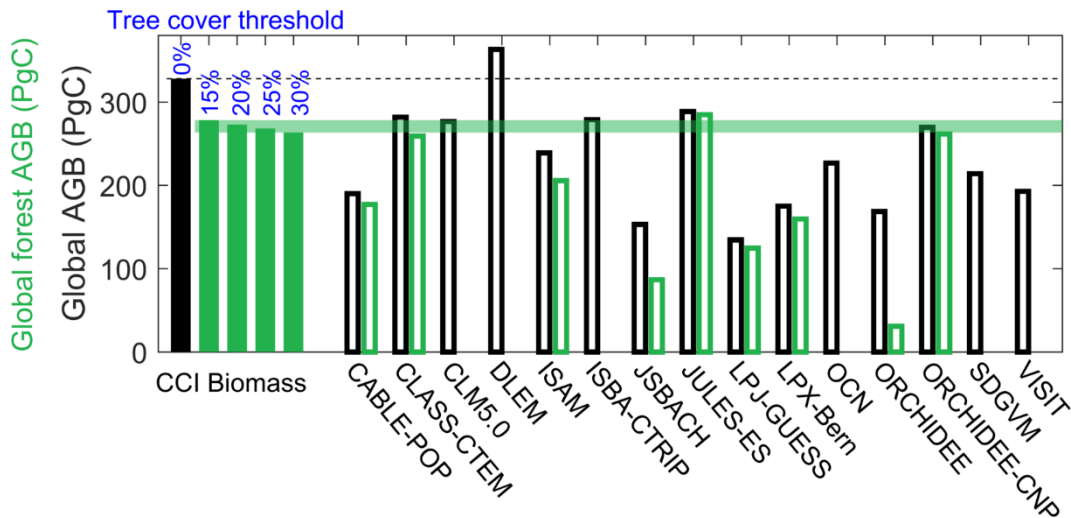


Figure 3-4: Global total all plants AGB (black bars) and forest AGB (green bars) circa the year 2017 derived from the CCI Biomass dataset and DGVMs. Based on the Hansen dataset, forest pixels are defined in the CCI Biomass dataset by the tree cover thresholds of 15%, 20%, 25% and 30%.

TRENDY DGVMs were forced by the same land-use change dataset, LUH2v2h. The reasons for different modelled forest areas are (a) models use different rules used to translate land cover to different PFTs (Table 3-2), i.e., models have different distributions of natural vegetation; (b) some models represent dynamic vegetation and shifting cultivation processes, others don't (Table 3-2). In addition, the LUH2V2h data may not match the forest area from the CCI Biomass data set.

Some models can reproduce global AGB values, but they are not exempt from regional biases. For all plants AGB, as shown in Figure 3-5a, all the models show lower all plants AGB than the CCI Biomass product in the wet tropics, temperate and boreal regions. Only the DLEM, CLASS-CTEM and JULES-ES models provide higher all plants AGB than CCI Biomass in the dry tropics, the others give lower estimates. For the forest AGB, as shown in Figure 3-5b, large differences between DGVM estimates and CCI Biomass with a 30% tree cover threshold can be found in the wet tropics. DGVMs provide lower forest AGB than CCI Biomass. JSBACH, JULES-ES, CABLE-POP and ISAM also underestimate forest AGB in the boreal region compared to CCI Biomass. Only CLASS-CTEM and ORCHIDEE-CNP overestimate forest AGB relative to CCI Biomass in temperate forests.

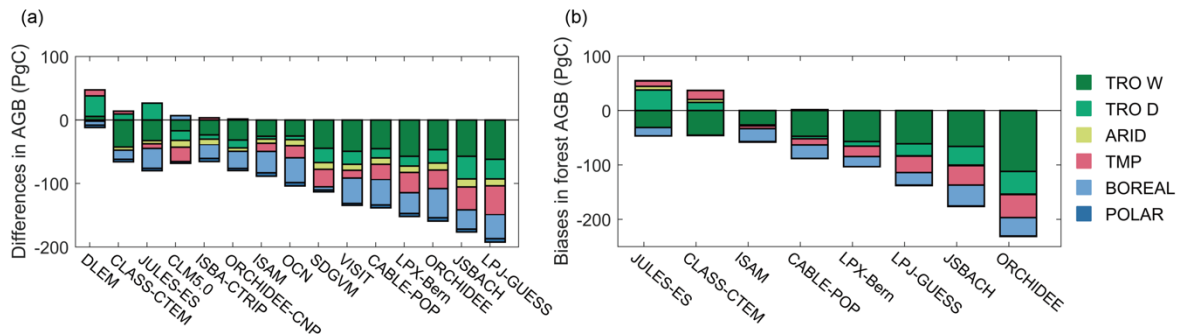


Figure 3-5: (a) Biases in the total all plants and forest AGB (simulated minus CCI Biomass data) in six biomes circa 2017. The Köppen-Geiger climate classification map (see Figure 3-3) is used to determine biome types. TRO W = wet tropical, TRO D = dry tropical, ARID = arid, TMP = temperate, BOREAL = boreal, POL = polar.

To understand the reason for the discrepancy between modeled and observed AGB at the biome scale, we compare AGB density from CCI Biomass and the ensemble mean of Trendy DGVMs. Figure 3-6a and 3-6b show the differences in AGB density of all plants and forests. This shows that the forest AGB is the most uncertain component, and contributes most of the biases in all plants AGB. Large differences in AGB density can be found in wet tropical forests and forests in Europe and North America.

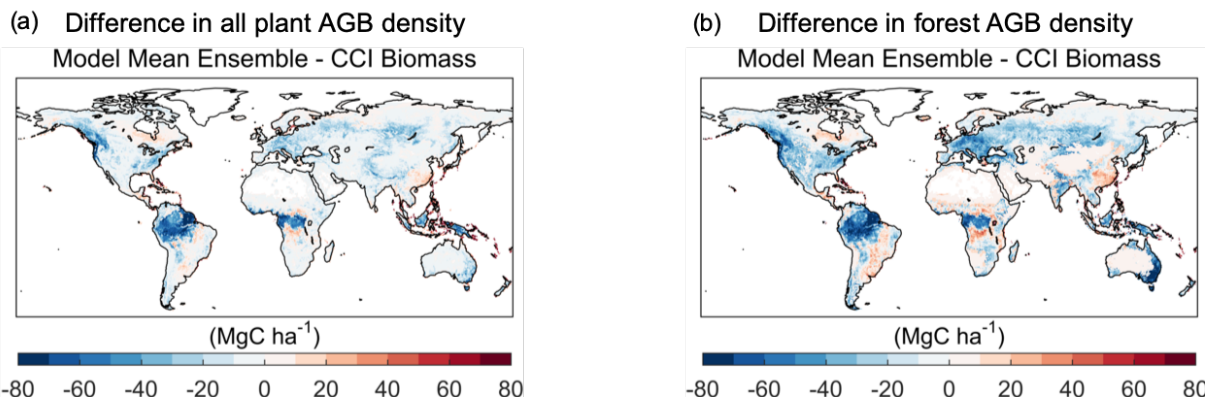


Figure 3-6: (a) Difference in AGB density of all plants between the multi-model ensemble of Trendy DGVMs and CCI Biomass. (b) Difference in AGB density of forests between the multi-model ensemble of Trendy DGVMs and CCI Biomass. Forest AGB density from CCI Biomass are defined using 30% tree cover threshold.

3.2.2. Global, regional and local spatial variability of AGB density

To investigate how DGVMs reproduce global and local spatial gradients of AGB density, we calculated 1) global spatial correlations (R) between observed and modeled AGB density of all plants and forests, 2) regional spatial correlation between observed and modeled AGB density of all plants and forests in six biomes, and 3) local spatial correlation (r) between observed and modeled AGB density across 0.5° grid cells within super-grid-cells of 10° . The first and second metrics give an evaluation of how well models reproduce the global and regional gradients of AGB density. The third one reflects the similarity of spatial variability of AGB density, and is relevant for evaluating models at local scale within biomes or ecotones ($10^\circ \approx 1,000$ km at the equator).

Most DGVMs appear to reproduce well the large-scale variations in AGB density across the globe when compared to the CCI Biomass data set (Figure 3-7). In particular, DGVMs show stronger agreement with the CCI Biomass in simulating the spatial variability of AGB density of all plants ($R = 0.85$, multi-model ensemble mean) than of forests ($R = 0.70$, multi-model ensemble mean). For the regional spatial variability of AGB density, DGVM estimates show strong agreement with CCI Biomass in simulating the variations of all plants AGB density in the wet and dry tropics and boreal regions. DGVMs also show good agreement in simulating the variations of forest AGB density in the wet tropics, boreal and polar regions. However, relatively poor skills of DGVMs in simulating the AGB density of forests can be found in arid, temperate and dry tropics, particularly the OCN model in arid and temperate areas and the CLASS-CTEM model in the tropics and temperate regions.

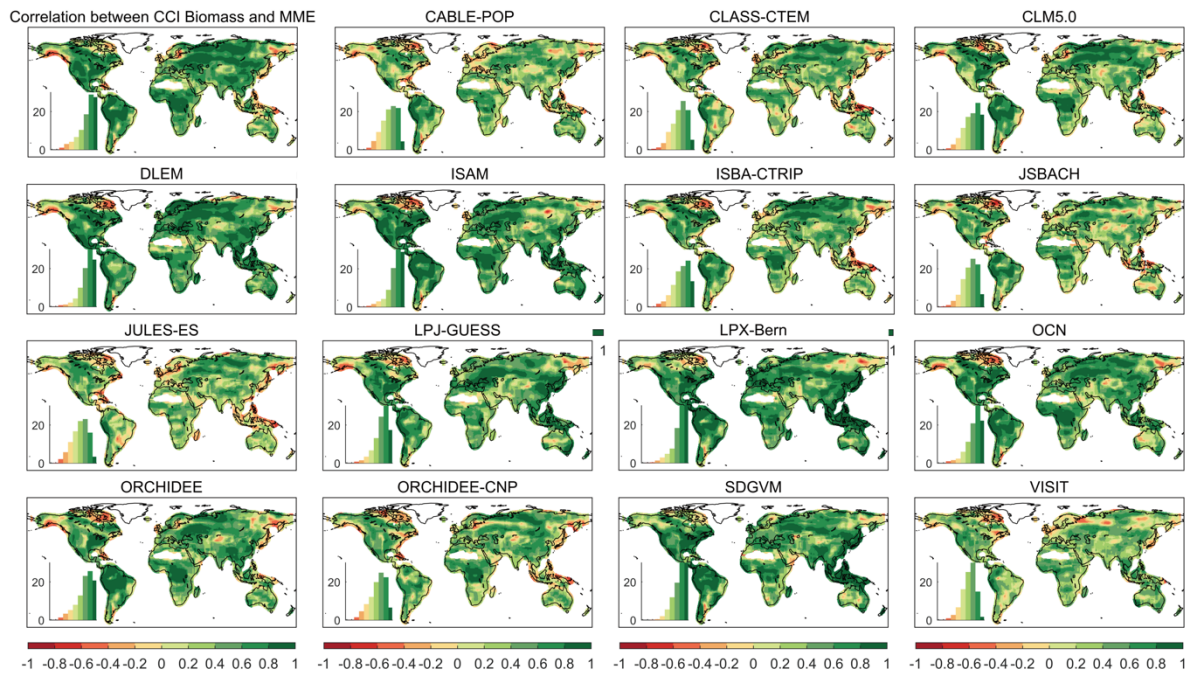


Figure 3-7: Spatial patterns of correlation coefficients between the CCI Biomass and simulated spatial local variation of all plants AGB density (individual panels labelled by model name). The correlation coefficients are calculated using all 0.5° grid cells of AGB density within super-grid-cells of 10° .

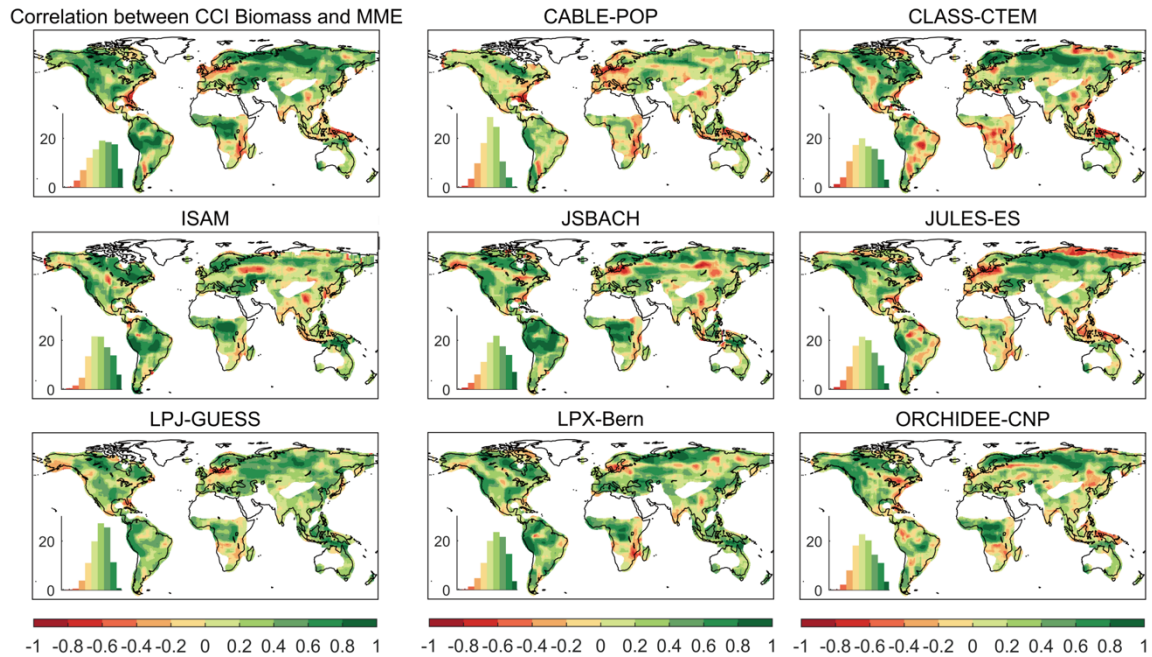
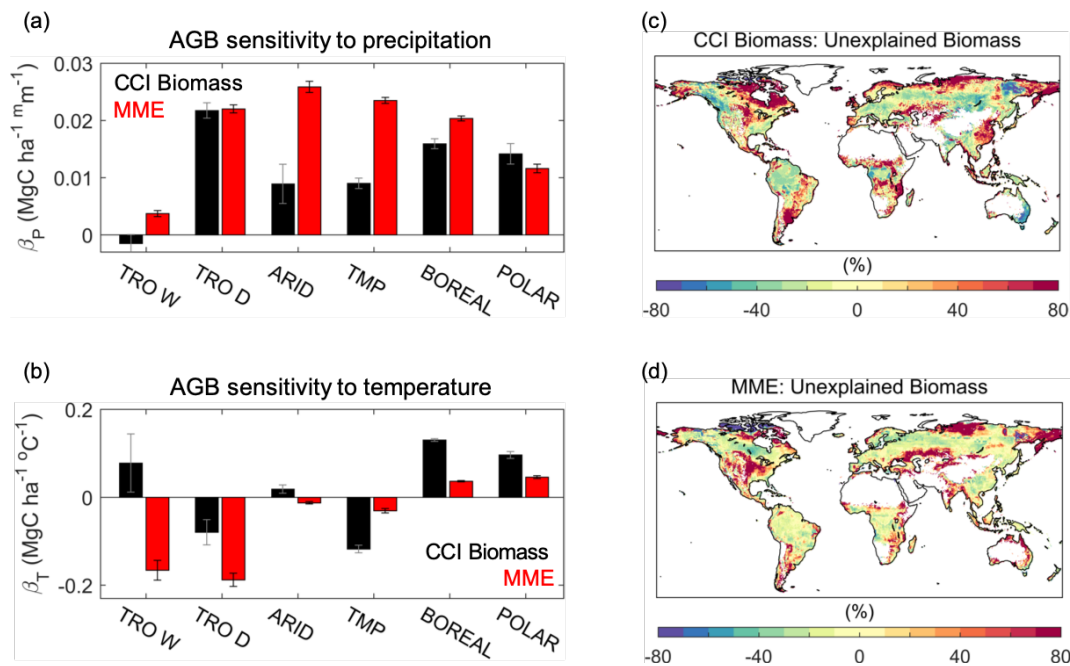


Figure 3-8: Same as Figure 3-8, but for forest AGB density.

The local spatial correlation coefficient r between the reference and simulated spatial local variation of all plants AGB density and forest AGB density is shown in Figures 3-8 and 3-9. These show that DGVMs can well capture the spatial variations of all plants derived from CCI Biomass, but the JULES-ES and VISIT models show a relatively low value of r for both tropical and high latitude regions (Figure 3-8). Generally, DGVMs show lower local correlation with forest AGB density from CCI Biomass than with all plants AGB density from CCI Biomass, particularly in some dry tropics, arid and temperate regions (Figure 3-9). This is probably due to the difference in definition of forest between CCI Biomass data (using tree cover map) and DGVMs (based on their own Plant Functional Type map).





	Ref	CCI Biomass Climate Assessment Report v3		
	Issue	Page	Date	
	3.0	29	14.07.2021	

Figure 3-9: The observed and simulated sensitivity of AGB density to precipitation (a) and temperature (b) in six biomes. MME is the multi-model ensemble mean of 15 DGVMs. The sensitivities are calculated using linear regression, $AGB = \beta_0 + \beta_1Pre + \beta_2Tmp$. The residuals in AGB density of the fitting regression model are in (c) and (d). AGB density are from (c) CCI Biomass and (d) the multi-model ensemble mean (MME) of 15 DGVMs.

In addition to correlation coefficient statistics, we diagnosed the modelled and CCI Biomass-based spatial sensitivity of AGB density to temperature and precipitation in six biomes using multiple linear regressions (Figure 3-10a and 3-10b). The sensitivity of AGB density from CCI Biomass to precipitation is positive in five biomes except in the wet tropics. DGVMs show a higher positive sensitivity of AGB density to precipitation in arid and temperate regions than the sensitivity derived from CCI Biomass (Figure 3-10a). This overestimated sensitivity of AGB density to precipitation relative to CCI Biomass parallels the fact that models also overestimate the precipitation sensitivity of GPP (Beer et al., 2010; their Figure 2). This implies that the overestimated spatial sensitivity of AGB density to precipitation in Figure 3-10 reflects how models simulate C inputs rather than mortality in response to the climatic driver. For the sensitivity of AGB density to temperature, CCI Biomass shows positive sensitivity in polar, boreal and wet tropics, and negative sensitivity in the dry tropics and temperate regions. DGVMs can reproduce the sign of sensitivity (except for the wet tropics) but underestimate its magnitude (Figure 3-10b). We also compare the AGB unexplained by climate from CCI Biomass and from the multi-model ensemble mean of Trendy. As shown in Figures 3-10c and 3-10d, the regions with high unexplained AGB exhibit similar patterns in CCI Biomass data and from the ensemble mean of Trendy models, and might be affected by natural/human disturbance.

3.3. Conclusions



All plants and forest above-ground biomass estimated by an ensemble of 15 DGVMs from the TRENDY v8 project are compared with the recently published CCI Biomass dataset of AGB density estimated from remote sensing observations. The main findings of the analysis are:

The 15 DGVMs display a wide range for the global and biome total all plants and forest AGB. The difference of total regional AGB between the CCI Biomass dataset and DGVMs stems from forest AGB density, in particular in the wet tropics and boreal regions. This might be due to different definitions of forests between data and models.

The CCI Biomass AGB estimates reflect the impact of natural and/or human disturbances, e.g. fire disturbance, human and livestock activity, and land use change on determining AGB density. However, such effects are largely underestimated or are not included in the current TRENDY DGVMs.

TRENDY DGVMs are limited in their ability to reproduce the magnitude of local spatial variations in forest AGB density. The model discrepancy in the magnitude of local spatial variations is partly due to overestimation of the sensitivity of biomass to local variability in precipitation.

Overall, for development and improvement of DGVMs, our findings show: (1) higher accuracy of model predictions of forest cover and forest cover changes is required, as these variables are directly related to the prediction of forest biomass carbon sequestration capacity; (2) the importance of improving the representation of human, livestock and fire disturbances in the DGVMs; (3) a high-resolution biomass dataset allows us to precisely calculate and evaluate biomass density of forest; (4) model skills in reproducing forest biomass density variability should be refined through further studies. In addition, a time series of global maps of AGB is necessary to evaluate the temporal variability of AGB derived from DGVMs.

	Ref	CCI Biomass Climate Assessment Report v3		
	Issue	Page	Date	
	3.0	30	14.07.2021	

4. Towards an evaluation of carbon allocation and turnover times in models

Variations in land carbon fluxes are related to the rate of carbon assimilation by plants, the fraction of carbon allocated to living plant tissues, and the time that carbon resides in living plant tissues before mortality and the carbon is respired back to the atmosphere (Malhi et al., 2009). The allocation of non-respired photosynthates, i.e. NPP, to various biomass pools and their individual turnover are described in far less detail in state-of-the-art dynamic global vegetation models (DGVMs) and Earth system models (ESMs) than the processes controlling canopy photosynthesis (Friend et al., 2014). Such structural model deficiencies limit the ability of these models to simulate terrestrial ecosystem carbon sequestration and to accurately predict its response to climate change (Friend et al., 2014; Negrón-Juárez et al., 2015; Wu et al., 2018).

In recent years, several studies used Earth Observation (EO) to infer forest carbon turnover times as the ratio of biomass and plant productivity under steady state assumptions (Carvalho et al., 2014; Thurner et al., 2016; Wang et al., 2018). This approximation reflects the overall turnover times of all plant carbon pools (including above- and below-ground). Yet the turnover times of different living plant tissues (e.g. leaves, roots and wood) vary greatly and allocation patterns differ in time and space (Hofhansl et al., 2015; Xia et al., 2019). Thus, it is useful to compute carbon allocation and turnover time of individual pools separately. At plot level, carbon allocation and turnover time within the major carbon pools have been measured (Chen et al., 2013; Xue et al., 2017), but information on large-scale patterns of carbon allocation and turnover are still lacking.



The first objective of this study is to generate gridded (25 × 25 km) pantropical maps of the partitioning of forest NPP to wood and leaves, and the turnover times of the wood and leaf carbon pools. We produce such estimates based on satellite-based or observation-based productivity, biomass, leaf area, fire and grass grazing emission data. Such purely data-driven carbon allocation fraction and turnover time are evaluated using ground measurements. Secondly, we explore the link between forest growth and mortality using data-driven carbon allocation and turnover estimates. Finally, we investigate the climate conditions and vegetation properties influencing the spatial gradients of carbon allocation fractions and turnover time. This work is viewed as a methodology to infer parameters relevant to the carbon cycle using maps of biomass change and productivity in a single data assimilation system, that can be extended to CCI Biomass change maps when they become available for different epochs.

The results of Section 4 have been recently published as a journal paper (Yang et al., 2021)

4.1. Data assimilation of carbon allocation and turnover times from EO data

4.1.1. Parameter optimization

The data assimilation system, hereafter referred to as the Carbon Assimilation in the Tropics (CAT), follows a Bayesian formalism to optimize six unknown parameters, viz. carbon allocation fraction ($a_{f,w}$, $a_{f,l}$ and $a_{g,l}$), turnover rates ($r_{f,w}$ and $r_{f,l}$) and ratio of the initial stock of forest wood pool to leaves pool ($S_{f,w}/S_{f,l}$), using satellite-based continuous annual AGB and derived leaf mass from leaf area index (LAI) and specific leaf area (SLA) over the period 2011-2016. Within each 25km × 25km grid cell (the original

	Ref	CCI Biomass Climate Assessment Report v3		
	Issue	Page	Date	
	3.0	31	14.07.2021	

resolution of the L-VOD dataset calibrated against biomass maps), we define a quadratic cost function $J(x)$ which describes the misfit between the observation-based and model-estimated AGB and leaf mass, taking their uncertainties and prior values into account. The expression for $J(x)$ is given by

$$J(x) = (x - x_b)^T B^{-1} (x - x_b) + (H(x) - y)^T R^{-1} (H(x) - y)$$

where x are the optimized parameters, x_b are their prior values, and B is the error covariance matrix for the prior parameters. The priori values, the ranges of the optimized parameters, and the uncertainty of their prior values are given in Table 4-1. y and $H(x)$ are the observation-based and model-estimated AGB and leaf mass. R is the error covariance matrix of y , which is assumed to be diagonal and 10% of the mean value of y . The function $J(x)$ is iteratively minimized by the sequential quadratic programming (SQP) algorithm. At each iteration, an approximation is made to the Hessian of the Lagrangian function using a quasi-Newton updating method.

A box model is used to describe the carbon state and dynamics of individual biomass carbon pools in two cover types, forest and grass. Forests have three carbon pools, i.e. wood ($S_{f,W}$), leaves ($S_{f,L}$) and roots ($S_{f,R}$), whereas grasses have only leaves ($S_{g,L}$) and roots ($S_{g,R}$). This box model has a generic conceptual structure, identical to that adopted by any carbon cycle model. The change in carbon stock of each pool over time (on a yearly time step) is calculated by the differences between the incoming and outgoing fluxes, represented as:



$$\begin{cases} \frac{dS_{f,W}}{dt} = a_{f,W} \times NPP_f(t) - r_{f,W} \times S_{f,W}(t) \\ \frac{dS_{f,L}}{dt} = a_{f,L} \times NPP_f(t) - r_{f,L} \times S_{f,L}(t) \\ \frac{dS_{g,L}}{dt} = a_{g,L} \times NPP_g(t) - r_{g,L} \times S_{g,L}(t) \end{cases}$$

where $S_{f,W}$, $S_{f,L}$ and $S_{g,L}$ is the carbon stock of a certain pool, the incoming flux is the product of the associated carbon allocation fraction ($a_{f,W}$, $a_{f,L}$ and $a_{g,L}$) and Net Primary Productivity (NPP_f and NPP_g), and the outgoing flux from each pool is assumed to be proportional to the carbon stock of the pool, with a proportionality constant given by the turnover rate ($r_{f,W}$, $r_{f,L}$ and $r_{g,L}$). The turnover time of the grass leaf biomass pool ($1/r_{g,L}$) is assumed to be one year, following Erb et al. (2016). Note that if the optimized turnover time of the forest leaf biomass pool ($1/r_{f,L}$) were shorter than one year, the carbon stocks would be calculated as $S_{f,L}(t) = a_{f,L} \times NPP_f(t) \times 1/r_{f,L}$, based on the steady-state assumption.

The outgoing fluxes in the box model include loss of biomass due to natural and climate-induced plant mortality. Additionally, we account as a removal flux for disturbance-induced loss, i.e., the biomass of grass and leaves consumed by livestock, the biomass of leaves consumed by herbivory (like insects, wild grazers, or browsers), and the fire-driven biomass loss to match observation-based values of AGB and leaf mass (Figure 4-1). H is defined by the following:

$$H(x) - y: \begin{bmatrix} (S_{f,L} \times (1 - c) + S_{f,W}) \times f_f + S_{g,L} \times f_g - F - G \\ S_{f,L} \times (1 - c) \times f_f + S_{g,L} \times f_g - G - F_g \end{bmatrix} - \begin{bmatrix} AGB \\ LAI \times SLA \end{bmatrix}$$

where f_f and f_g are forest and grass cover fractions in the year of 2011 derived from the MODIS land cover map (i.e. MOD12Q1). G is the grass biomass consumed by livestock, F is the total fire-induced biomass losses, and F_g is the biomass removed from the grass carbon pools due to fires. The parameter c is the total leaf consumption rate by tropical herbivores, with an approximate value of 0.2 (Coley et al., 1996).

	Ref	CCI Biomass Climate Assessment Report v3		
	Issue	Page	Date	
	3.0	32	14.07.2021	

We use two gridded NPP and one gridded GPP dataset, three L-VOD AGB datasets and two LAI datasets (see Section 4.1.2 and 4.1.3) in the data assimilation system to optimize the estimates of carbon allocation and turnover.

Table 4-1: The prior value of the optimized parameters and their uncertainties.

Parameters	Prior value	Prior range	Uncertainty of prior	
<i>Allocation fractions</i>				
Leaf	0.33 ^a	0.001-0.882 ^b	0.2 ^a	
Forest	Wood	0.32 ^a	0.008-0.954 ^b	0.15 ^a
	Leaf + Wood	-	< 1	-
Grass	Leaf	0.3	0-1	0.4 ^c
<i>Turnover rates</i>				
Forest	Leaf	0.64	0.04-12 ^d	0.02 ^e
	Wood	0.021 ^e	0.0025-1 ^f	0.02 ^e

^aThe prior values of NPP allocation fractions and their uncertainty (1σ) are derived from the measurements in the tropics collected by Xia et al. (2019).

^bThe ranges of allocation fractions are derived from a global database for leaf, stem and root biomass (Chen et al., 2013). Such ranges are estimated using observations from all over the world.

^cThe uncertainty of the grass leaf allocation fraction is set to 40% of its range.

^dThe range of turnover rate of forest leaf pool stem is from the 2207 leaf longevity records from TRY dataset. The longevity of tropical forest leaves range from 1 month to 24 years.

^eThe prior value of turnover rate of the forest wood biomass pool and its uncertainty are estimated using plot data from Galbraith et al. (2013). For the uncertainty of turnover rate of the forest leaf biomass pool, we use the same value as the forest wood biomass pool.

^fThe range of turnover rate of the forest wood pool is estimated by Martínez-Ramos and Alvarez-Buylla (1998); the longevity is estimated to be less than 400 years.

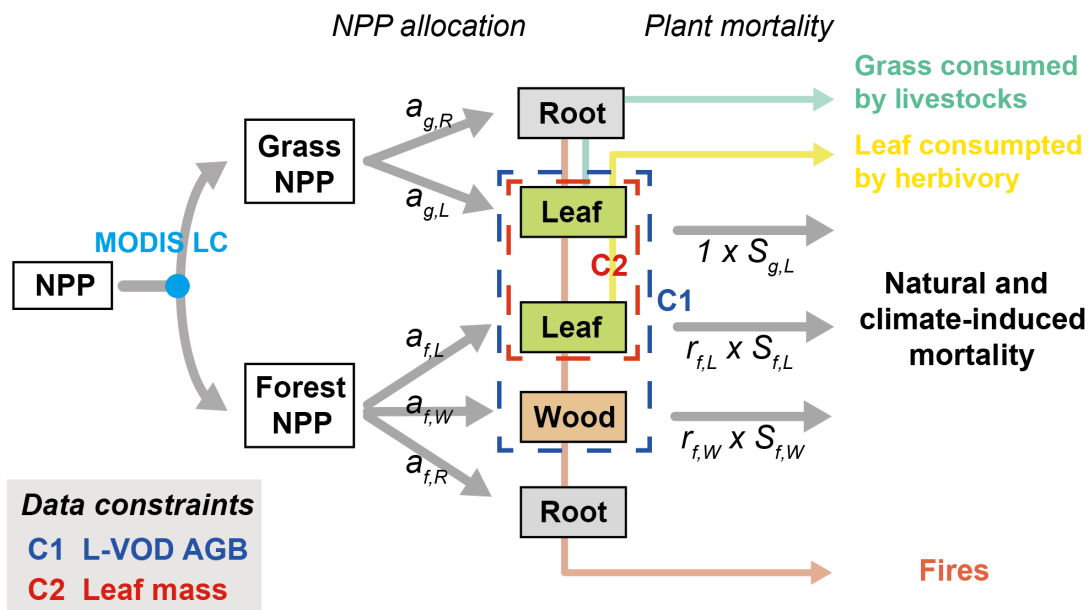




Figure 4-1: The structure of the carbon emulator and data used to retrieve $25\text{km} \times 25\text{km}$ carbon state and process variables. Within each $25\text{km} \times 25\text{km}$ grid cell, satellite-based NPP over forest and grassland are partitioned into the live biomass pools. Natural and climate-induced plant mortality are the output of the live biomass pools. Fire fluxes are derived from the GFED dataset. Grass grazing fluxes are from the ISIMIP2 project. Data constraints include L-VOD above-ground carbon and leaf mass. Here, leaf mass is obtained by multiplying specific leaf area (SLA) from Butler et al. (2017) and leaf area index from MODIS, GIMMS and GlobMAP datasets. a_x is the allocation fraction; S_x is the biomass stocks; and r_x is the rate of turnover. Details are provided in section 4.1.

4.1.2. Input data to the carbon cycle data assimilation system

NPP and GPP. We use two satellite-based NPP datasets for the period 2010-2016 from MODIS (Zhao et al., 2010) and GIMMS (Smith et al., 2016). The former is provided at a spatial resolution of $1\text{km} \times 1\text{km}$, whereas the latter has a spatial resolution of $0.5^\circ \times 0.5^\circ$. The GIMMS NPP was calculated by using GIMMS photosynthetically active radiation and leaf area index data, based on the same algorithm as the MODIS NPP product. We also use a global GPP dataset based on a hybrid EO-driven mechanistic model, the Breathing Earth System Simulator (BESS). The BESS couples an atmospheric radiative transfer module, a two-leaf canopy radiative transfer module, and an integrated carbon assimilation-stomatal conductance-energy balance module (Jiang et al., 2016). The spatial resolution of the derived GPP is $0.5^\circ \times 0.5^\circ$. In the tropics, and a constant carbon use efficiency (CUE) of 0.4 (Malhi et al., 2012) is used to convert GPP into NPP (hereafter referred to as BESS NPP).

Table 4-2: The definition of forest and grass.

Types	Land cover types	Tree cover fraction
Forest	Evergreen Needleleaf Forest (ENF)	-
	Evergreen Broadleaf Forest (EBF)	
	Deciduous Needleleaf Forest (DNF)	
	Deciduous Broadleaf Forest (EBF)	

	Ref	CCI Biomass Climate Assessment Report v3		
	Issue	Page	Date	
	3.0	34	14.07.2021	

Grass	Mixed Forest (MF) Shrub	
	Woody Savanna Savanna	> 25%
	Woody Savanna Savanna	≤ 25%
	Grassland Cropland	-

By averaging high-resolution data over neighboring pixels, it is possible to generate aggregated forest and grass NPP at coarser spatial resolution. This requires that each pixel is pre-labelled as “forest” or “grass”. In this study, using a 1 km MODIS land cover map and 30 m Landsat tree cover map (Hansen et al., 2013), we assign each 1km pixel to a “forest” or “grass” category based on the following rules (Table 4-2): (1) If the land cover type is one of six forest and shrub types (i.e. Evergreen Needleleaf Forest, Evergreen Broadleaf Forest, Deciduous Needleleaf Forest, Deciduous Broadleaf Forest, Mixed Forest and Shrub), we classify this pixel as “forest”; (2) If the land cover type is Grassland or Cropland, we classify the pixel as “grass”; (3) If the land cover type is woody savanna or savanna, the category of the pixel depends on the tree cover fraction. If tree cover fraction is greater than 25%, we classify this pixel as “forest”; if not, classify it as “grass”. The 30m Landsat tree cover map is first aggregated to 1 km resolution. Within each 25 × 25km spatial window, forest NPP is then computed as the average of NPP values of 1-km pixels that are classified as “forest”, and grass NPP is computed in the same manner (Figure 4-2); the forest (grass) cover fractions are calculated as areal fraction of pixels labelled “forest” (“grass”). Note that we use land cover and tree cover maps for the year 2010, and all the areas that experienced a decrease of tree cover fraction of more than 5% over the period of 2010-2016 are masked, because we focus in this study on estimating carbon allocation and turnover times that were unaffected by forest loss disturbances.

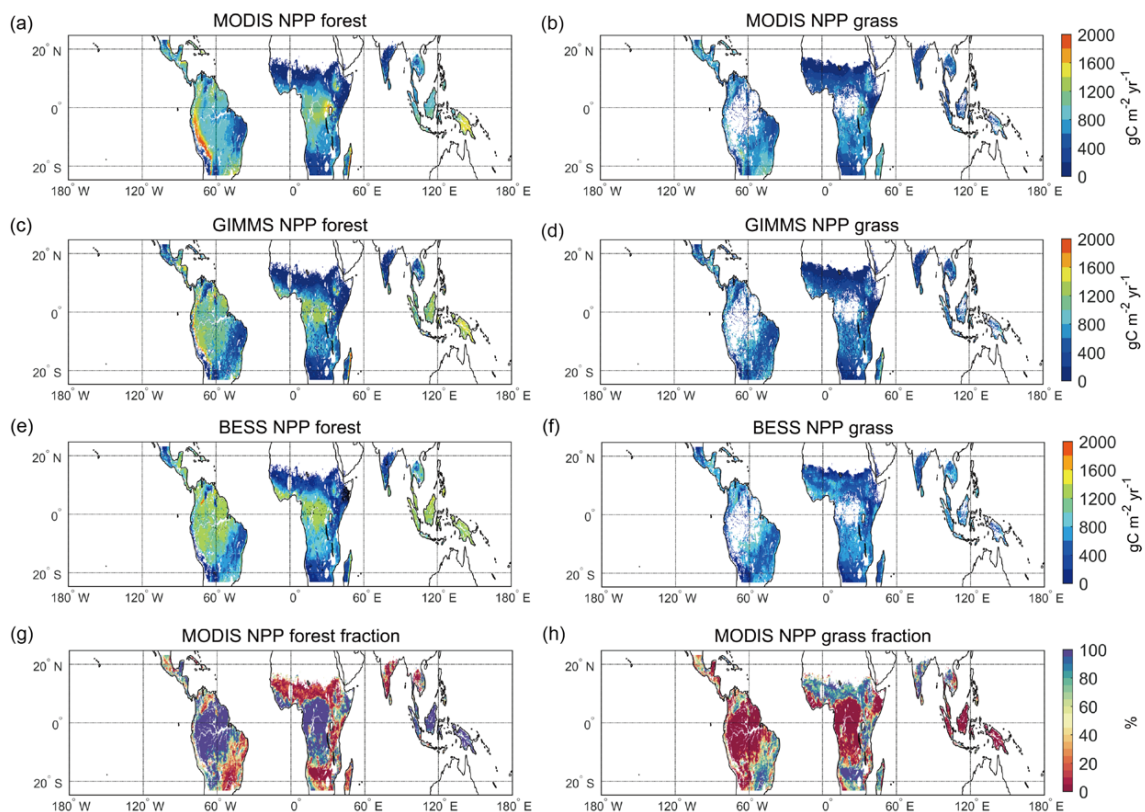


Figure 4-2: Forest NPP, grass NPP, forest and grass cover fraction. Spatial patterns of (a) MODIS forest NPP, (b) MODIS grass NPP, (c) GIMMS forest NPP, (d) GIMMS grass NPP, (e) BESS forest NPP, and (f) BESS grass NPP during the period 2011-2016, and spatial patterns of (e) forest cover fraction and (f) grass cover fraction from MODIS land cover data.

For the GIMMS and BESS NPP data, the values of NPP at 0.5° resolution are downscaled to 25 km resolution. Then, we use the ratio of grass NPP to forest NPP (γ), and the forest cover fraction (f_f) and grass cover fraction (f_g) from the MODIS land cover map to estimate GIMMS (and BESS) forest NPP and grass NPP (Figure 4-2), as follow:

$$NPP_f = NPP / (f_f + \gamma f_g)$$

$$NPP_g = NPP / (f_f + \gamma f_g)$$

Fire-induced biomass losses. Annual fire carbon emissions during the period 2011-2016 are from the fourth-generation Global Fire Emission Database (GFED4s, <https://www.globalfiredata.org/index.html>), based on satellite information on fire activity and vegetation parameters. The original data at 0.25° resolution are re-gridded to the 25×25 km working resolution of the data-assimilation system.

Grass biomass consumed by livestock. The grass biomass consumed by livestock data originate from Herrero et al. (2013) for the year 2000, and are extrapolated to the period 1900-2012 using gridded changes in livestock density (Chang et al., 2016). The original data at 0.5° resolution are downscaled to 25×25 km resolution. In this study, we use the multi-year averages of grass biomass consumption for the period 2011-2012.

4.1.3. Input data to constrain carbon allocation and turnovers

Satellite-based AGB. Satellite-based tropical above-ground biomass (AGB) data at 25×25 km resolution covering the period from 2010 to 2017 are from Fan et al. (2019). These data (hereafter referred to as L-VOD AGB) are produced by using vegetation optical depth at L-band (L-VOD) from the passive microwave Soil Moisture and Ocean Salinity (SMOS) satellite. Three L-VOD AGB maps are available, corresponding to the calibrations from previous AGB maps by Saatchi et al. (2011), Avitabile et al. (2016), and Baccini et al. (2012). In the update of this work the CCI biomass map will be used to calibrate L-VOD. These three sets of L-VOD AGB are used to constrain the model-estimated AGB.

Satellite-based LAI. Satellite-based Leaf Area Index (LAI) is obtained from the GIMMS3g (Zhu et al., 2013) and GlobMAP datasets (Liu et al., 2012). GIMMS3g LAI is available at $1/12$ -degree spatial resolution and GlobMAP LAI at 8km spatial resolution. Both products are aggregated to 25km spatial resolution. To avoid saturation effects over dense forests, GIMMS and GlobMAP LAI are calibrated against a limited amount of LAI data from field measurements obtained between 1982 and 2000 and compiled by the Oak Ridge National Laboratory (ORNL) (Scurlock et al., 2001). In tropical regions, linear calibration coefficients for GIMMS and GlobMAP LAI are 0.95 and 0.89, respectively (Figure 4-3).

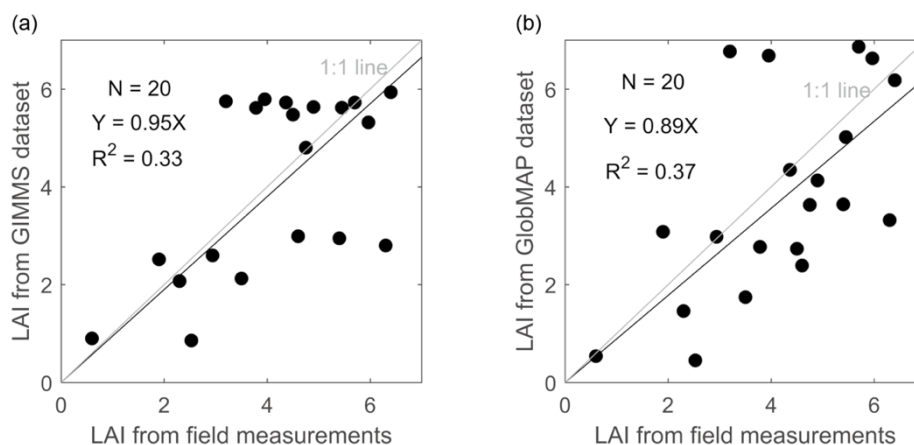




Figure 4-3: Comparison between satellite-based and measured LAI from field sites in the tropics. LAI measurements cover the period 1982-2000. The linear calibration coefficients are estimated by linear regression through the origin; they are 0.95 for the satellite-based LAI from (a) GIMMS and 0.89 for those from (b) GlobMAP datasets.

Observation-based SLA. The global map of SLA is generated from optimal interpolation of the global plant trait TRY database using Bayesian modelling (Butler et al., 2017). These data are at 0.5-degree spatial resolution, and in this study are used to calculate leaf mass, combined with calibrated satellite-based LAI data.

	Ref	CCI Biomass Climate Assessment Report v3		
	Issue	Page	Date	
	3.0	37	14.07.2021	

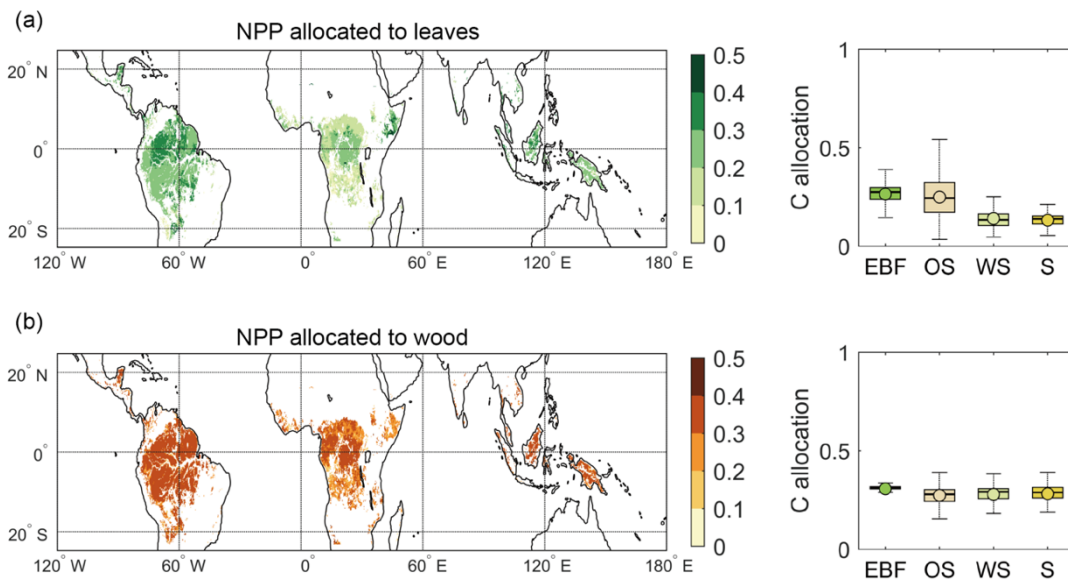


Figure 4-4: Forest NPP allocated to leaf and wood carbon pools. The left column panels show the spatial distributions of forest NPP allocation to (a) leaf (af,L) and (b) wood (af,W) carbon pools. The right column panels show the boxplots of af,L and af,W estimates per vegetation type according to the MODIS land cover map. Vegetation types are evergreen broadleaf forest (EBF), open shrublands (OS), woody savannas (WS) and savannas (S).

4.1.4. Uncertainties in carbon allocation and turnover times

An ensemble of 18 sets of carbon allocations and turnover times maps are estimated from three NPP, three L-VOD AGB datasets, and two LAI datasets. The standard deviations of different combinations are used to estimate parameter uncertainties associated with the spread between those different input fields. For example, we calculate the standard deviation of carbon allocation and turnover times associated with NPP data when fixing each LAI and each AGB value. This value reflects the uncertainties in the optimized parameters due to using different NPP products. We perform the same analysis for different LAI and AGB products. The average uncertainties associated with the NPP, LAI and AGB products are computed.

4.2. Spatial patterns of carbon allocation and turnover

Using the Carbon Assimilation in the Tropics (CAT, Figure 4-1), we first optimize the allocation of forest NPP to leaf and wood carbon pools. As shown in Figure 4-4, for the tropical forest, on average NPP allocations to wood (0.30 ± 0.04) are significantly higher than to leaves (0.24 ± 0.07) (p -value < 0.05 , according to the t-test). From the wet tropics to the dry tropics, both forest NPP allocation into wood and leaves declines slightly. For forest NPP allocation to wood, there are minor differences between different vegetation types. By contrast, for the forest NPP allocation to leaves, evergreen broadleaf forest (median and interquartile range: $0.27^{+0.03}_{-0.03}$) and open shrublands ($0.24^{+0.08}_{-0.07}$) exhibit higher fractions than for woody savannas ($0.13^{+0.03}_{-0.02}$) and savannas ($0.14^{+0.01}_{-0.03}$). This is consistent with the expectation that more carbon would be allocated to below-ground biomass in biomes more limited by water availability.

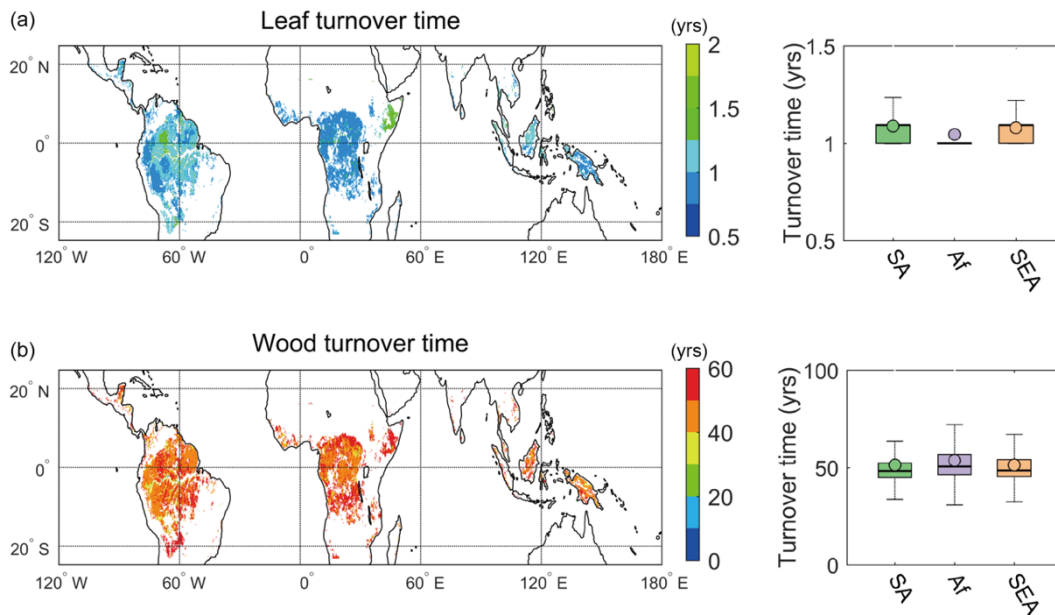


Figure 4-5: Turnover time of forest leaf and wood carbon pools. The left column panels show the spatial distributions of turnover time of forest (a) leaf carbon pools ($1/r_{f,L}$) and (b) wood carbon pools ($1/r_{f,W}$) in each 25×25 km grid cell. The right column panels show the boxplots of $1/r_{f,L}$ and $1/r_{f,W}$ estimates for different tropical continents, including South America (SA), Africa (Af), and Southeast Asia (SEA).

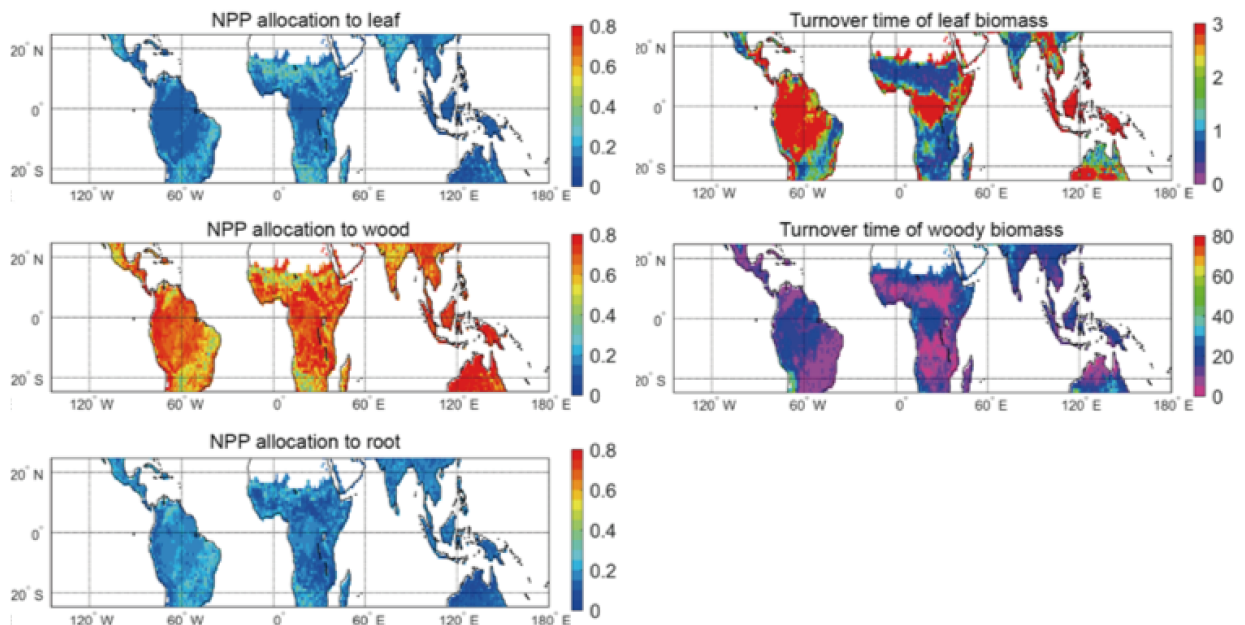


Figure 4-6: Carbon allocation and turnover time from CARDAMOM. Spatial patterns of forest NPP allocation to leaf, wood and root pools, and the turnover times of forest leaf and wood carbon pools.

The optimized turnover times of forest leaf and wood pools presented in Figure 4-5 are spatially homogeneous. Leaf turnover times of tropical forests vary little across the three continents, while wood turnover times in Africa (median and interquartile range: $50.1^{+5.5}_{-4.0}$ yr) are slightly longer than in South America ($48.2^{+4.0}_{-3.3}$ yr) and Southeast Asia ($48.3^{+5.4}_{-3.1}$ yr). This is consistent with results from

permanent plot measurements, reporting longer carbon residence times in Africa (Sullivan et al., 2020). Our estimates of wood turnover are double those from the CARDAMOM model-data fusion framework (Figure 4-6), which combined the DALEC carbon balance model with satellite-based LAI and biomass data (Bloom et al., 2016) and allometric criteria to select plausible solutions for ill-constrained parameters.

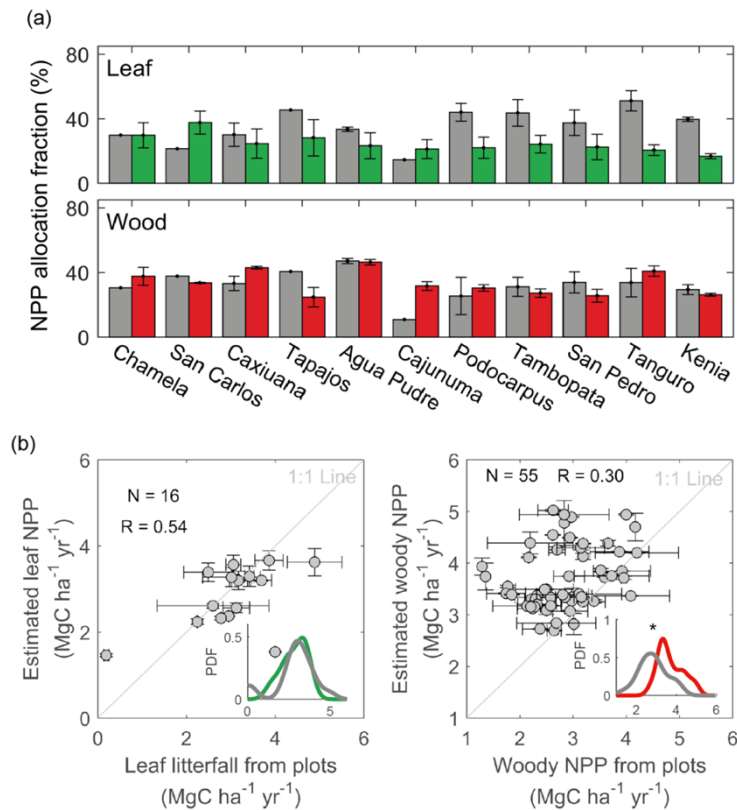


Figure 4-7: Evaluation with ground-based NPP allocation to leaf and wood, leaf NPP and woody NPP. (a) CAT-estimated and measurement-based carbon leaf and wood allocation fractions in Amazon. Grey bars show ground measurements, while colored bars show the estimates from CAT. The errorbars for grey bars are one standard deviations of the repeated measurements from different years and plots; and the errorbars for colored bars are one standard deviations of CAT estimates resulted from different input and constraint data. (b) The comparison of plot-scale leaf litterfall and CAT-estimated leaf NPP, which are obtained as the product of leaf allocation and mean forest NPP. (c) The comparison of plot-scale woody NPP and CAT-estimated woody NPP (the product of wood allocation and mean forest NPP). The insets in (b) and (c) show the probability density function of measured and estimated leaf NPP and woody NPP. Horizontal error bars show 1 standard deviations across plots within one 25×25 km grid cell. Vertical error bars show 1 standard deviation stem from different input and constraint data.

4.3. Evaluation using ground-based measurements

We compare independent plot-scale forest wood and leaf allocation fractions from Xia et al. (2019) with CAT results. As shown in Figure 4-7, the CAT-optimized wood allocation fractions agree fairly well with the mean of ground measurements, but leaf allocation fractions in southern Amazonia plots are slightly underestimated compared to ground measurements. Here, plot-scale leaf allocation fractions were calculated as the ratios of leaf NPP, wood NPP to total NPP. The underestimation of leaf allocation fraction in CAT may reflect the different total NPP between our satellite fields and plot data. Thus, we

further directly compare plot-scale independent leaf litterfall and above-ground woody NPP from plots with CAT results. As shown in Figure 4-7b, our estimated leaf NPP agrees fairly well with plot-scale independent leaf litterfall data (correlation $R = 0.54$, p -value < 0.05) from Chave et al. (2010). Woody NPP is calculated as the product of wood allocation and total NPP, the latter from the average of three NPP products MODIS, GIMMS and BESS. The range of our estimates is similar to plot-scale data (ranging from 1 to 5 $\text{MgC ha}^{-1} \text{ yr}^{-1}$), but mean plot-scale woody NPP is $0.8 \text{ MgC ha}^{-1} \text{ yr}^{-1}$ smaller than our estimates. This also confirms that plot-scale total NPP (e.g. sum of leaf NPP, woody NPP and root NPP) is smaller than the satellite-based estimates.

In old-growth forest plots, woody turnover times are calculated as the ratio of above-ground woody biomass and above-ground woody productivity, assuming steady state, and this gives values comparable to our turnover times estimates. Gridded woody turnover time has a significant positive, but weak, spatial correlation with plot data (Figure 4-8; spatial correlation $R = 0.25$, p -value < 0.05). However, CAT systematically underestimates high values of wood biomass turnover time. This may be partly due to underestimation of carbon stocks in high vegetation density areas (Figure 4-8b) because of a possible saturation of L-VOD to biomass in high biomass regions (Fan et al., 2019), the mismatch of the spatial scales of satellite and plot data, and the proportion of degraded and deforested area.

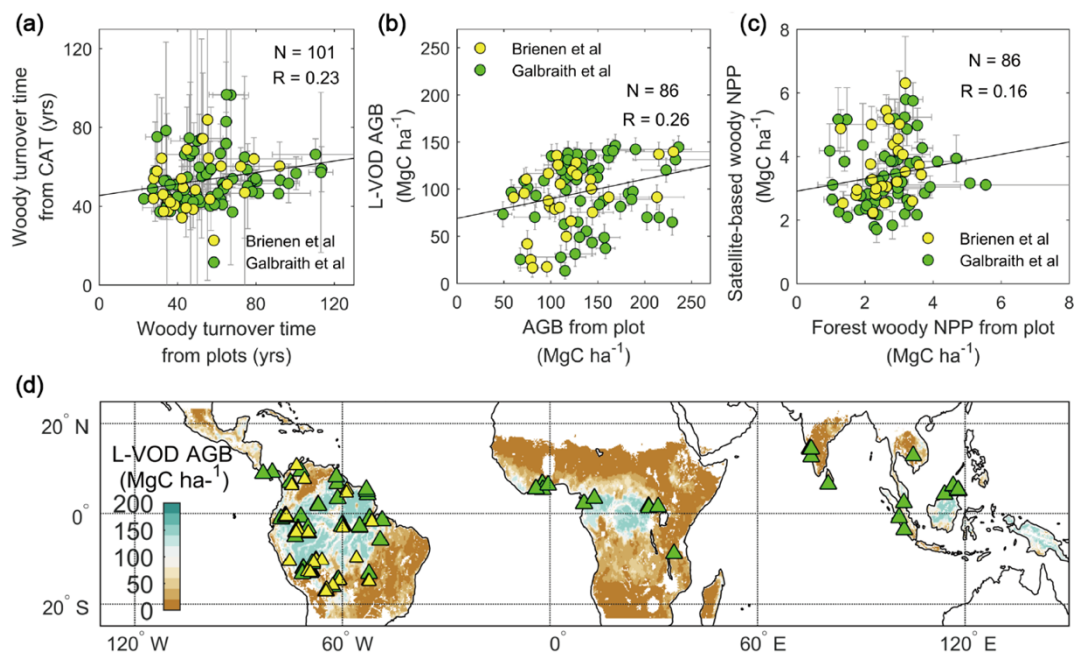


Figure 4-8: Validation with measured turnover times of wood biomass pools at the mature forest plots. (a) CAT-estimated and measurement-based turnover times of wood biomass pools in the tropics. Measurement-based woody turnover time were calculated by the ratio of woody biomass and woody productivity from Brienen et al. (2015) and Galbraith et al. (2013). (b) The comparison between measurement-based and L-VOD AGB. (c) The comparison between measurement-based and satellite-based forest woody NPP. Horizontal error bars show the one standard deviations across plots within one $25 \times 25 \text{ km}$ grid cell. Vertical error bars show the uncertainty stem from different input or constraint data. (d) The locations of forest plots. Background color reflects the mean annual L-VOD AGB for the period 2010-2016.

4.4. Trade-offs between allocation to growth and turnover time

Here we analyze emergent relations between wood/leaf growth (defined as woody/leaf productivity) and wood/leaf turnover times. Figure 4-9a shows a general inverse relation between leaf growth and leaf turnover time, and also an inverse relation between wood growth and wood turnover time, across tropical forests (Figure 4-9b). Previous studies using tree-ring data or ground measurements also found this trade-off between growth and tree lifespan (Brienen et al., 2020; Büntgen et al., 2019; Wright et al., 2011). But our analysis suggests that this trade-off exists not only at the tree level but also at the organ level. Figure 4-9c and 4-9d show that leaf turnover times decrease by less than 40% when leaf productivity increases by 50%, while wood productivity increases in the same proportion (50%), corresponding to a larger reduction in wood turnover times, especially in the wet tropics. Several possible theories explaining growth-lifespan trade-offs have been proposed. Some believe that faster growth is a direct or indirect reason for shorter lifespan: faster growth requires higher metabolic rate, which may have negative effects on lifespan (Issartel and Coiffard, 2011); or under the fixed-size hypothesis: when trees grow faster, they will die early once they reach a maximum size (Büntgen et al., 2019). Others, however, think that this trade-off is in line with plant investment strategies, i.e., plants adjust allocation to balance growth against security (e.g. safer mechanical and hydraulic architecture) (Wright et al., 2011).

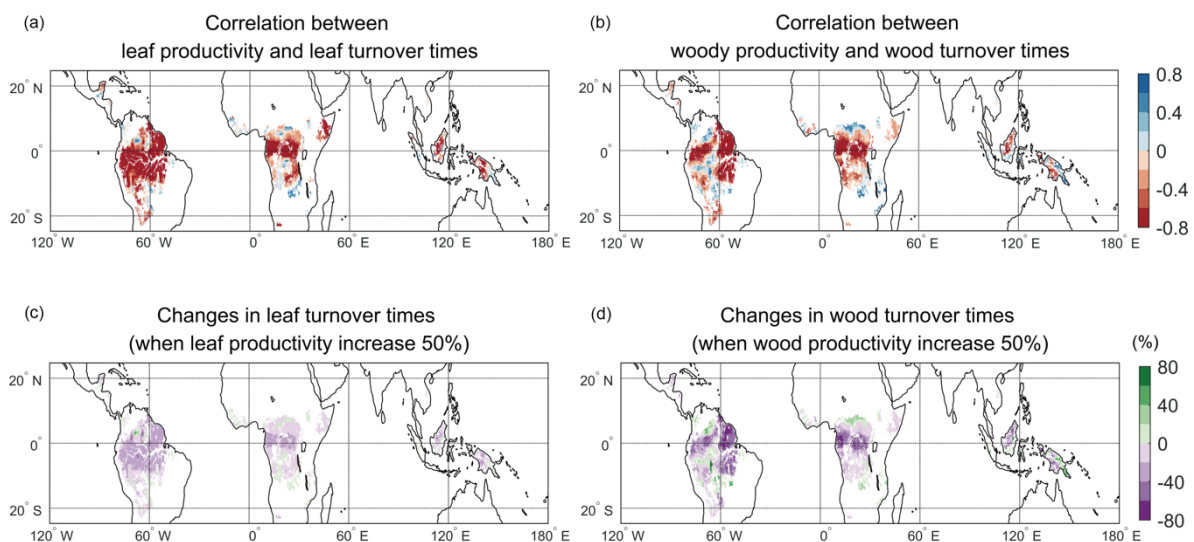


Figure 4-9: Relationship between leaf/wood growth and wood/leaf lifespan. Correlation coefficients between (a) leaf productivity and leaf turnover times, (b) wood productivity and wood turnover times. (c) (d) The percentage of changes in leaf and wood turnover times when leaf and wood productivity increase by 50%. These percentages are calculated using least-squares regression. Correlation and regression analysis are applied to each spatial window of $5^{\circ} \times 5^{\circ}$.

4.5. Factors influencing spatial gradients of carbon allocation and turnover times

Carbon allocation fraction.

We observe in Figure 7 that the most important factor influencing the changes of carbon allocation fraction to leaves and wood is canopy height. Our results show that carbon allocation fraction to leaves increases significantly with canopy height. As shown in Figure 7a, for young and short forests, more

carbon tends to be allocated to wood for stem growth, the carbon allocated to wood being double that to leaves. Old and tall forests adjust their carbon allocation coefficient to leaves to be close to the carbon allocation fraction to wood. Fig. 7b shows the relationship between canopy height and carbon allocation fraction to leaves and wood for evergreen broadleaf forests, wood savannas and savannas, respectively. We found no significant difference in wood allocation fraction for different vegetation types, whereas woody savannas and savannas have a lower carbon allocation fraction to leaves than evergreen broadleaf forests. Nevertheless, different vegetation types have similar increases in carbon allocation fraction to leaves with increasing canopy height.

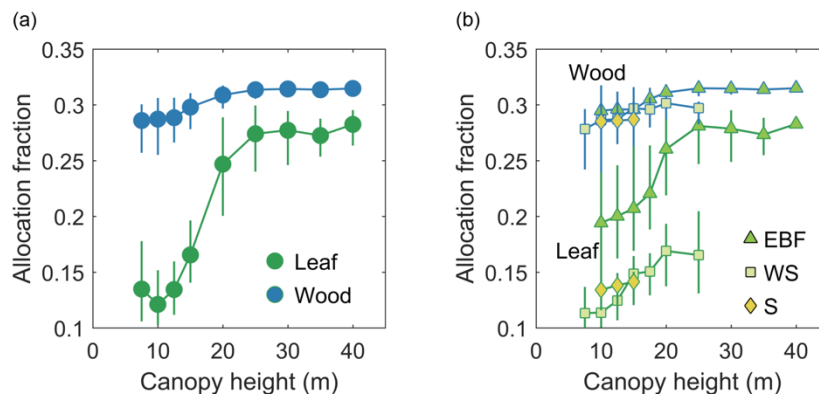


Figure 4-10: The relation between carbon allocation and canopy height. (a) Median of leaf and wood allocation fraction for each percentile bin of canopy height. (b) Same as (a), but for evergreen broadleaf forests, woody savannas and savannas respectively. The vertical errorbars in (a) and (b) show interquartile range of allocation fractions.

In addition to canopy height, we observe in Figure 4-11 that background climate (mean annual temperature, precipitation and radiation) controls forest NPP allocated to leaves and wood. Figure 4-11a, b, e, f show that carbon allocation fraction to leaves and wood are both positively related with temperature and precipitation. The median leaf and wood allocation increases significantly with increasing temperature and precipitation. Our results also show that the sensitivity of leaf allocation to background temperature and precipitation is higher than that of wood allocation (Fig. 8). Elevated air temperature could increase photosynthetic capacity, while temperatures below the physiological optimum (typically 30-40 oC) and increasing temperature may accelerate leaf ageing or increase leaf thickness (Huang et al., 2019; Niinemets, 2001). Thus, plants in a high temperature environment with no water limitation tend to allocate more carbon to leaves. Another possible mechanism for the relationship mentioned above is in line with functional balance theory (Franklin et al., 2012; Hofhansl et al., 2015), namely that plants adjust their biomass among various tissues in response to environmental changes to obtain the most growth-limiting resource. Water is the main limitation resource for growth in the dry tropics (Nemani et al., 2003). For plants in water-limited environments, more carbon is allocated to roots, therefore less carbon to wood and leaves, as shown in Fig. 8b and f. The effect of radiation on regulating carbon allocation is relatively weak: only wood allocation for short trees slightly decreases with radiation increase (Fig. 4-11g).

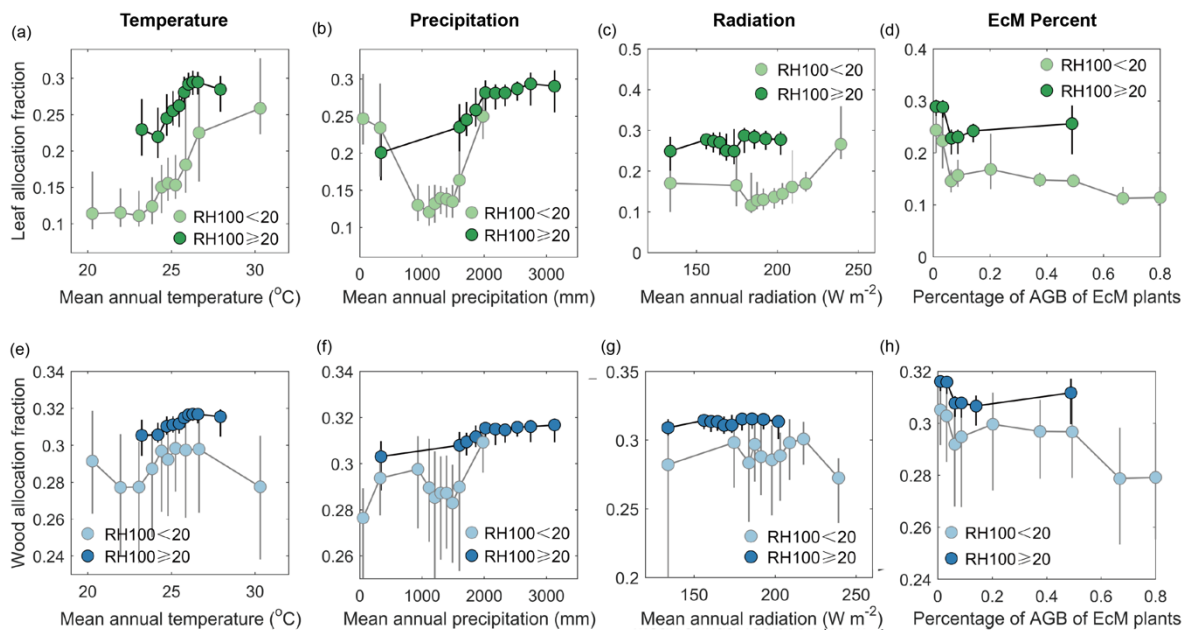


Figure 4-11: The relation between carbon allocation and climate and vegetation factors. Median of leaf allocation fraction for each percentile bin of (a) temperature, (b) precipitation, (c) radiation and (d) the percentage of forests associating with ectomycorrhizal (EcM) fungi. Lines with light color dots represents trees with height being less than 20 m, while lines with dark color dots represents trees with height being more than 20 m. (e)-(h) Same as (a)-(d), but for wood allocation fractions. The vertical error bars show the interquartile range of allocation fractions.

Last, we observe in Figure 4-11d and 4-11h that carbon allocation fractions are related to the mycorrhizal associations of plants: carbon allocated to wood and leaves decreases with the percentage of forests associating with ectomycorrhizal (EcM) fungi. This implies that forests with high ectomycorrhizal (EcM) fungi allocate more carbon to below-ground roots rather than above-ground leaves and wood. Previous studies suggested that high EcM forests have high nitrogen demand, and EcM fungi are more efficient in taking up nitrogen but in exchange for carbon (Sulman et al., 2017). This is why carbon allocated to below-ground increases with increasing EcM percentage.

Turnover time.

For wood turnover time, we observe in Figure 4-12 that background climate (especially precipitation) plays an important role in influencing its spatial variation. Wood turnover time decreases with precipitation, especially in the transitional wet-to-dry region (mean annual precipitation around 2000 mm yr⁻¹). For leaf turnover time, as shown in Figure 4-12, leaf turnover time is negatively correlated with SLA and leaf phosphorus concentration. This suggests that the “leaf economic spectrum” (e.g. trade-offs between SLA and leaf phosphorus concentration) rather than climate conditions regulate its spatial variation. This is consistent with the findings of Shiodera et al. (2008) and Xu et al. (2017), indicating the observed leaf longevity in tropical evergreen forests is positively correlated with leaf mass per area (LMA, i.e. the inverse of SLA). These relations may be driven by ecological coordination with plant growth strategies. An increase in leaf phosphorus concentration can enhance the photosynthetic capacity, and forests with high photosynthetic capacity usually belong to fast-growing species, because they can benefit from fast nutrient resorption and high photosynthesis.

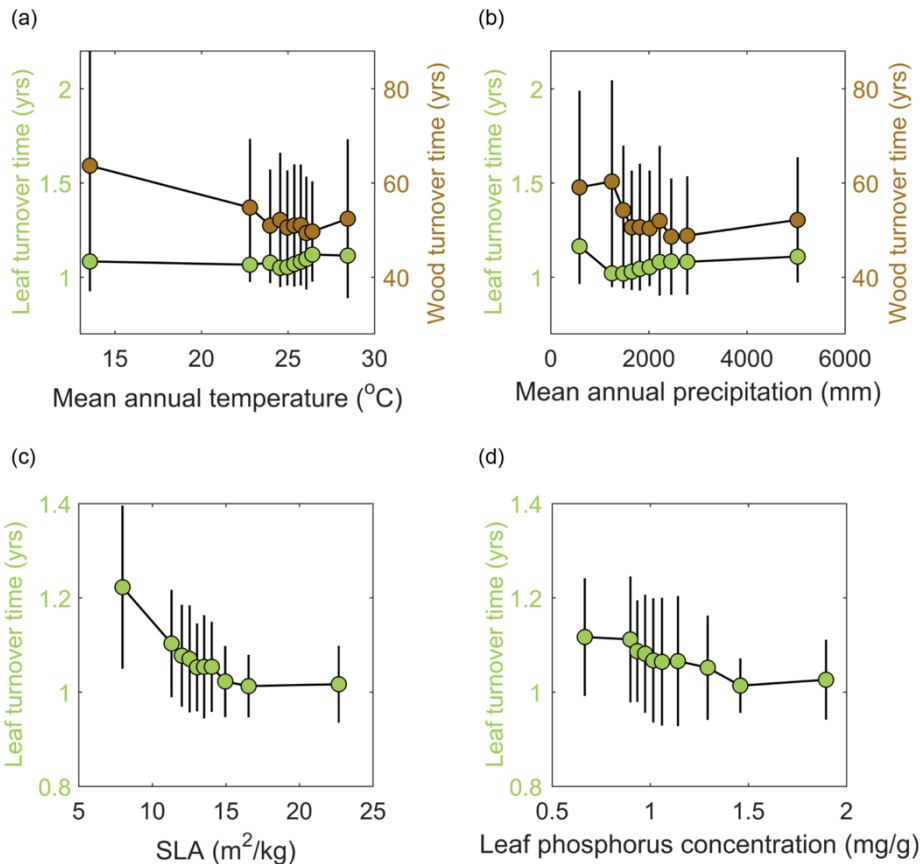


Figure 4-12: The relation between carbon turnover times and climate and leaf traits. Median of leaf and wood allocation fraction for each percentile bin of (a) temperature, (b) precipitation, (c) specific leaf area (SLA) and (d) leaf phosphorus concentration. The vertical error bars show interquartile range of allocation fractions.

Implications for Land Surface Models

Carbon allocation, stocks and turnovers are poorly constrained in dynamic global vegetation models (DGVMs) (Friend et al., 2014; Negrón-Juárez et al., 2015; Malhi et al., 2011). Malhi et al. (2011) noted that a large dispersion in the allocation of NPP in tropical forests across models and a model bias towards high wood allocation. DGVMs allocate NPP to different carbon pools using three types of approaches: (1) a fixed allocation scheme; (2) dynamic allocation driven by allometric constraints; (3) dynamic allocation driven by resource availability (i.e. nutrients, water and light). The first approach sets fixed allocation coefficients for a given PFT, but large differences in allocation fractions within a PFT are reported (our Figure 4-4) (Taylor et al., 2019). De Kauwe et al. (2014) performed a model-data intercomparison at forest free-air CO₂ enrichment sites, and found that the models using the second approach fail to reproduce the observed response of carbon allocation fraction to water and nutrient limitations, whereas those using the third approach are unable to estimate biomass accurately.

In addition to allocation, processes related to turnover, in particular woody turnover times, determine carbon storage in biomass. Most of the current DGVMs use a fixed turnover rate (or mortality rate) for wood biomass and they do not explicitly simulate tree mortality due to fire, competition, insects and pathogens, etc. A few exceptions (e.g. LPJ and LPJ-GUESS) do not use a simple fixed value, and calculate mortality rate due to negative carbon balance, competition, harsh climate and fire (Xue et al., 2017).

Our gridded turnover time/rate of carbon pools may help improve model structure or parameterization schemes.

Uncertainties and Limitations

As any uncertainty in EO data used as input to CAT propagates into our optimized parameters, we estimate uncertainties in carbon allocation and turnover times (defined here as the ratio of the standard deviation and mean value, %) by using different NPP, AGB and LAI datasets in carbon allocation and turnover times. The uncertainties tend to be large in semi-arid and arid tropical regions, especially for woody turnover times (Figure 4-13). For wood allocation and turnover, large uncertainties in the dry tropics arise mainly from L-VOD AGB data, whereas uncertainty in leaf allocation and turnover come from NPP products. In the wet tropics, the uncertainty of NPP and LAI data make the major contribution to uncertainty of leaf allocations, leaf turnover and wood allocation, while uncertainty in wood turnover times is primarily attributed to uncertainty in NPP products. This implies that improved confidence in the observed tropical vegetation productivity and biomass would help us to better understand NPP–carbon cycle–climate interactions (Piao et al., 2020).

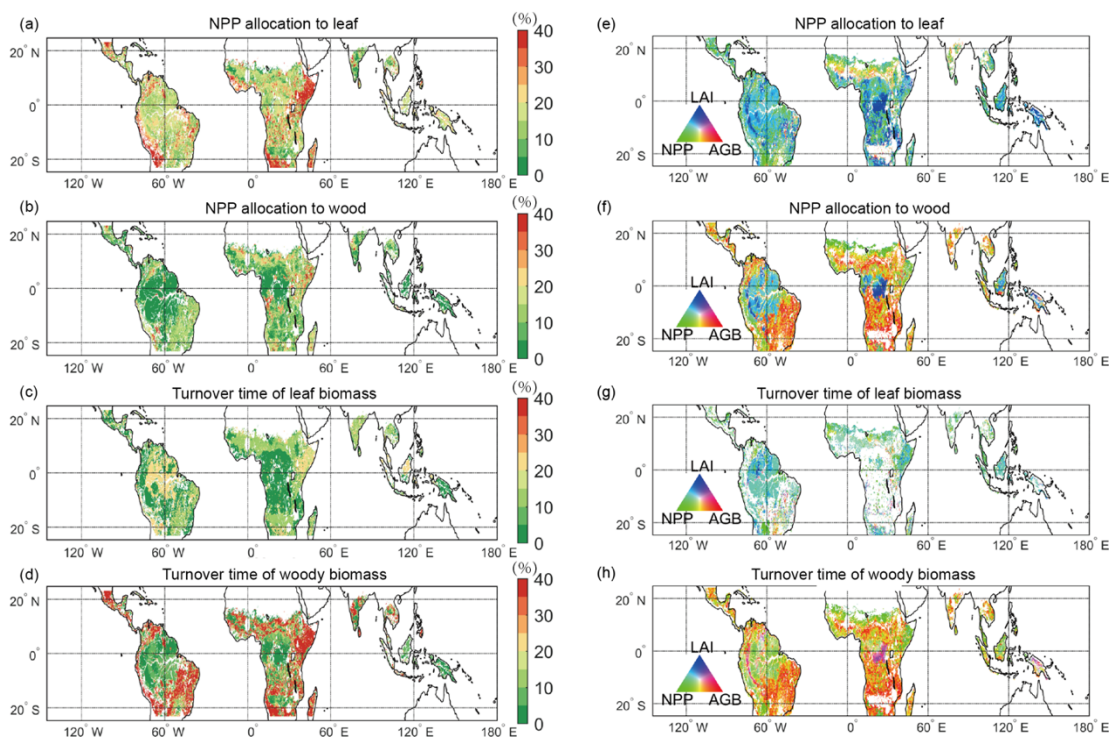




Figure 4-13: The contribution of the uncertainties of carbon allocation and turnover time. (a)-(d) The percentage of standard deviation (%), relative to the mean values) of forest NPP allocation fractions, turnover time of biomass pools. (e)-(h) The contribution of uncertainty derived from the different sources of LAI (blue), NPP (green) and L-VOD AGB (red) datasets. Contribution from a certain variable is represented by a specific color, e.g. the red colored regions indicates the uncertainty is mainly from the L-VOD AGB datasets.

It is important to recognise some caveats in our approach. The most critical one is that we only provide multi-year averages of carbon allocation and turnover times due to data limitations, but we know that allocation of carbon and its turnover time vary with climate and extreme events (Doughty et al., 2015; Phillips et al., 2004). We only analyzed the large-scale spatial variation of allocation and turnover in response to environmental conditions and plant traits, but more work should be done to explore temporal variations. Another caveat is that the grass NPP allocation and turnover time are less

	Ref	CCI Biomass Climate Assessment Report v3		
	Issue	Page	Date	
	3.0	46	14.07.2021	



constrained than the forest ones, because specific constraint data for grass is lacking. Furthermore, we did not address soil carbon storage, as we focus on the processes related to plant carbon allocation and turnover. Soil is a major store for carbon, and soil carbon storage will be influenced by the input of carbon to the soil compartment. Future work should investigate the interactions between plant allocation and soil processes. In addition, in this study carbon turnover times are assumed to be caused by natural and climate-induced mortality, but they are also partly affected by human disturbance and degradation, so high-resolution satellite imagery is needed to quantify forest loss.

In this study, six years (from 2011 to 2016) of satellite-based biomass, NPP and LAI data have been amalgamated to constrain the underlying processes of the vegetation carbon cycle. Therefore, we generate pan-tropical maps at 25km resolution of forest and grass carbon allocation and turnover times, in which the parameter estimates are purely data-driven, and independent of plant functional types. The spatial variations of our data-driven carbon allocation and turnover times are in good overall agreement with observed estimates from forest plots. Our data-driven estimates show a universal trade-off between leaf productivity and leaf turnover times, as well as between wood productivity and wood turnover times. Moreover, we find canopy height is the most important factor influencing spatial gradients of wood and leaf carbon allocation, which are partly associated with temperature, water and nutrient availability. For the spatial variation of turnover times, abiotic factors, such as temperature and precipitation, play major roles in regulating wood turnover times, whereas biotic factors, such as SLA and leaf phosphorus concentration affect leaf turnover times. Our data-driven estimates of carbon allocation and turnover times provide a basis for more detailed exploration of these mechanisms in field studies, and may ultimately help improve model structure and the parameterization schemes used in Earth System Models.

5. Tropical biomass change. Case study of impacts and legacy from the 2015-16 El Niño event

Tropical forests hold the largest biomass pool on Earth and account for more than one-third of the total global net primary productivity (NPP) (Pan et al., 2011). Small changes in their growth and mortality can substantially affect the concentration of atmospheric CO₂ and have a global impact (Phillips et al., 2009). The El Niño-Southern Oscillation (ENSO) leads to droughts impacting highly productive tropical forests, compounded with fires, increased diseases and insect attacks (Seidl et al., 2017), which enhance tree mortality and reduce carbon storage, weakening the tropical forest carbon sink (Brienen et al., 2015; Mitchard, 2018). Previous observational and modelling studies reported that tropical regions switched from a carbon sink to a source as a result of drought associated with the latest severe El Niño event in 2015-2016 (Liu et al., 2017; Rödenbeck et al., 2018), and the subsequent recovery of forest carbon stocks has been quantified (Wigneron et al., 2020). However, few studies have explored the factors that control the spatial and temporal variations in forest carbon stocks during and after drought.

The 2015/16 El Niño brought record-breaking temperatures and major drought in the tropics. Warmer and dryer conditions were close to those anticipated in future warming scenarios (Malhi et al., 2018). Increases in the severity, duration and frequency of drought and heat stress associated with climate change could fundamentally alter the community composition, structure, and biogeography of forests (Allen et al., 2010; Brodrigg et al., 2020). The advent of novel remote sensing data allows us to analyze the short-term and long-term responses of the biomass in tropical ecosystems to such a major climate disturbance. The short-term response, including a decline in photosynthesis due to

	Ref	CCI Biomass Climate Assessment Report v3		
	Issue	Page	Date	
	3.0	47	14.07.2021	

stomata closure, has been monitored through field and satellite observations during drought (Rifai et al., 2018; Malhi et al., 2015). The long-term response involving tree mortality, changes in forest structure and recruitment, may persist for several years after drought (Wigneron et al., 2020; Shenkin et al., 2018). Using the Random Forests (RF) model, a machine learning algorithm, we then identify the key climatic, edaphic and biotic factors controlling the regional declines and ongoing recovery of forest biomass. We also use the large-scale observation of forest vertical structure as a vegetation property to help explain the biomass variations, because drought not only impacts the mortality and growth of tree individuals, but also affects forest community composition (Brodribb et al., 2020).

5.1. Data and Methods

5.1.1. L-VOD AGB data

Satellite-based L-VOD (L-band microwave observation of vegetation optical depth) data at 25 × 25km resolution covering the period from 2010 to 2019 from the Soil Moisture and Ocean Salinity (SMOS-IC, v2) satellite is used for the analysis. The method used here to compute AGB from L-VOD in the same as the method used in Wigneron et al. (2020), Brandt et al. (2018) and Fan et al. (2019). That is, we use four different static AGB benchmark maps to calibrate the relationship between L-VOD and AGB for the entire tropical region, South America, Africa separately. The calibration process for only Southeast Asia is not used because of the limited SMOS observations in this region. The AGB benchmark maps include three pantropical maps (i.e. Saatchi et al., 2011; Baccini et al., 2012; Avitabile et al., 2016) and one map covering only the savannas and woodland of Africa (Bouvet et al., 2018). After the calibration, 10 maps of L-VOD AGB are obtained, and the median of these 10 maps of monthly L-VOD AGB covering the period 2010-2018 are used in this study. Because of the poor quality of L-VOD data over water bodies, we remove the 25km pixels where the areal fraction of regularly flooded wetlands (RFWs) is more than 80%, using a global wetland map from Tootchi et al. (2019).

5.1.2. Forest cover data



In this study, we focus on the tropical intact evergreen forests (between 25°N and 25°S), which are defined by the ESA CCI land cover map of 2015 (300m resolution), the Hansen forest cover map for the year of 2000 and annual deforestation maps from 2000 to 2018 (25m resolution; Hansen et al., 2013). First, using the 300m resolution CCI land cover map, we label the 25km pixels in which more than 50% of the 300m-sized pixels are evergreen forests (classes ID 50, 160, 170). Second, for each 25km pixel, we calculate the percentage of the 25km pixels with forest cover < 90% or affected by deforestation, using the Hansen tree cover map. The 25km pixels with forest cover < 90% or deforestation higher than 20% are removed.

5.1.3. Drought characteristics

The Cumulative Water Deficit (CWD) is widely used to describe the characteristics of meteorologically-induced drought in the tropics (Aragão et al., 2007). Based on precipitation data from NASA's Tropical Rainfall Measurement Mission (TRMM, monthly, 0.25° resolution, TMPA/3B43 v7) and evapotranspiration data from the Global Land Evaporation Amsterdam Model (GLEAM, monthly, 0.25° resolution, v3.3a), we calculate monthly CWD for each pixel, as follow:

$$CWD_m = CWD_{m-1} - E_m + P_m \text{ if } CWD_m < 0$$

$$CWD_m = 0 \text{ if } CWD_m \geq 0$$

	Ref	CCI Biomass Climate Assessment Report v3		
	Issue	Page	Date	
	3.0	48	14.07.2021	

where CWD_m is the cumulative water deficit of the current month, which is equal to the cumulative water deficit from previous months (CWD_{m-1}) plus the difference between the precipitation of the current month (P_m) and evapotranspiration (E_m). For each grid cell, the standardized anomaly of CWD (ACWD) at the i th grid for the t th month ($t = 1, 2, \dots, 12$) is calculated as:

$$ACWD_{i,t} = \frac{CWD_{i,t} - \overline{CWD_{i,t}}}{\sigma(CWD_{i,t})}$$

where $\overline{CWD_{i,t}}$ and $\sigma(CWD_{i,t})$ are the mean value and standard deviation (SD) of CWD at the i th grid for the t th month during the reference period (2000-2019).

We use the monthly ACWD to identify the spatial extent, duration, severity, onset and end of the 2015/16 drought in the tropical forest. For each grid cell, the ACWD is smoothed using the three-month running average to avoid a single wet month interrupting a long and consecutive dry period. The drought events which last < 3 months are not included in this study. Drought onset is defined as the first month with ACWD below the threshold of -1 SD, and the drought end is defined as the first month when ACWD exceeds the threshold of -1 SD. We defined the duration of drought as the period between the start and the end months of the drought event and the severity of drought as the median of ACWD during the drought period.

5.1.4. AGB response and recovery

We calculate the average monthly L-VOD AGB for the whole drought period, which lasted from Oct 2015 to Mar 2016, so $AGB_{15/16} = \overline{AGB}_i$ ($i = \text{Oct, Nov, Dec 2015, Jan, Feb, Mar 2016}$). The response of AGB during the drought are calculated as the averages of AGB stocks during the 2015/16 drought period minus the averages of AGB stocks for the same months during the years 2014 and 2015 ($\Delta AGB_{14/15 \rightarrow 15/16}$):

$$\Delta AGB_{14/15 \rightarrow 15/16} = AGB_{15/16} - AGB_{14/15}$$

We also calculate the average of AGB for the same months during the years 2016/17, 2017/18 and 2018/19. The decrease and increase in AGB after drought are calculated as:

$$\text{Decrease in AGB after drought: } AGB_{\min} - AGB_{15/16}$$

$$\text{Increase in AGB after drought: } AGB_{\max} - AGB_{\min}$$



where AGB_{\min} is the minimum value among $AGB_{15/16}$, $AGB_{16/17}$, $AGB_{17/18}$, and $AGB_{18/19}$, and AGB_{\max} is the maximum value of AGB after reaching AGB_{\min} . The percentage of AGB recovery is the ratio of increase in AGB after the drought and the sum of decrease in AGB during and after the drought, calculated as:

$$\text{The percentage of AGB recovery: } \frac{AGB_{\max} - AGB_{\min}}{AGB_{14/15} - AGB_{\min}}$$

5.1.5. Variable importance and partial dependence

To fit the AGB response during drought and recovery after drought, we use more than 20 predictor variables, including drought characteristics, background climate, soil property, forest structure, fire occurrence, and two categorical variables (Table 5-1).

The predictor variables of drought characteristics used are pre-drought ACWD ($ACWD_{pre}$), post-drought ACWD ($ACWD_{post}$), drought severity, drought duration, soil moisture (SM) and vapor pressure

	Ref	CCI Biomass Climate Assessment Report v3		
	Issue	Page	Date	
	3.0	49	14.07.2021	

deficit (VPD) anomalies during drought and after the drought. Soil moisture data are from SMOS-IC satellite. VPD is calculated using re-analysis climate products from MERRA,



$$VPD = SVP - AVP$$

$$SVP = 0.6108 \times e^{\frac{17.27 \times T_a}{237.3 + T_a}}$$



$$AVP = SVP \times \frac{RH}{100}$$

where SVP and AVP are saturated vapor pressure and actual vapor pressure (kPa), T_a is air temperature at 2m (oC), and RH is relative humidity at 2m (%). The predictor variables of background climate used are the average of temperature, precipitation and radiation during the drought period, and precipitation seasonality (SD of 12-month precipitation). The climatological monthly temperature, precipitation, and radiation are from the WorldClim database (<https://www.worldclim.org>). The predictor variable of soil properties is soil clay content (%) from SoilGrids (<https://soilgrids.org>). The predictor variables of forest structure from the Geoscience Laser Altimeter System (GLAS) onboard ICESat (Ice, Cloud, and land Elevation Satellite; <https://nsidc.org/data/icesat>) are canopy density (the proportion of an area on the ground covered by the tree crowns), canopy height (RH100; 100% energy return height), understory height (RH25; 25% energy return height), and the ratio of understory and canopy heights (RH25/RH100). The predictor variable of the occurrence of fire disturbance is fire radiative power (FRP) observations from the Global Fire Assimilation System (GFAS, Kaiser et al., 2012). In addition, two categorical variables are Continent (SA, AF, SEA) and the start of the recovery year (15/16, 16/17, 17/18).

Table 5-1: The predictor variables used in Random Forest.

	Ref	CCI Biomass Climate Assessment Report v3		
	Issue	Page	Date	
	3.0	50	14.07.2021	

Variables	Description	Unit	Original resolution	Source
<i>Drought characteristics (8)</i>				
Drought severity	The median of anomaly cumulative water deficit (ACWD) during the drought period	1	0.25 degree	See Methods
Drought duration	The number of months with ACWD < -1 SD	months	0.25 degree	
ACWD _{PRE}	The median of ACWD during the same drought months but in 2014/15	1	0.25 degree	
ACWD _{POST}	The median of ACWD during the same drought months but in the subsequent years after 2015/16	1	0.25 degree	
$\Delta SM_{14/15 \rightarrow 15/16}$	The mean of soil moisture (SM) anomalies during the drought period	1	25 km	SMOS-IC v2
$\Delta SM_{15/16 \rightarrow 18/19}$	The mean of SM anomalies during the same drought months but in the years after 2015/16	1	25 km	
$\Delta VPD_{14/15 \rightarrow 15/16}$	The mean of vapor pressure deficit (VPD) anomalies during the drought period	1	0.5 degree	MERRA2 See Methods
$\Delta VPD_{15/16 \rightarrow 18/19}$	The mean of VPD anomalies during the same drought months but in the years after 2015/16	1	0.5 degree	
<i>Soil properties (1)</i>				
Soil clay	Soil clay content (soil depth: 30cm)	%	1/20 degree	SoilGrids database
<i>Forest structure (4)</i>				
Canopy density	The proportion of an area on the ground covered by tree crowns	%	~75 m	GLAS database
RH100	100% return energy height, or top-canopy height	m	~75 m	
RH25	25% return energy height, or understory height	m	~75 m	
RH25/RH100	The ratio of understory and canopy height	1	~75 m	
<i>Background climate conditions (4)</i>				
Temperature	The climatological temperature during the drought month	°C	1 km	WorldClim database
Precipitation	The climatological precipitation during the drought month	mm	1 km	

	Ref	CCI Biomass Climate Assessment Report v3		
	Issue	Page	Date	
	3.0	51	14.07.2021	

Radiation	The climatological radiation during the drought month	W/m ²	1 km	
Precipitation seasonality	The Standard Deviation of the climatological monthly precipitation within a year	mm	1 km	
The occurrence of fires (2)				
FRP during the drought	The mean of Fire radiative power anomalies during the drought period	MW		Global Fire Assimilation System
FRP after the drought	The mean of Fire radiative power anomalies during the same drought months but in the years after 2015/16	MW		
AGB changes (1)				
$\Delta\text{AGB}_{14/15 \rightarrow 15/16}$	Above-ground biomass changes during the drought period in 2015/16, relative to the same period in 2014/15	MgC/ha	25 km	SMOS-IC v2
Categorical variables (2)				
Continent	Three labels. SA: South America, AF: Africa, SEA: Southeast Asia	-	25 km	-
Start year of recovery	The start year of recovery is the AGB lowest year. Three labels: 15/16, 16/17 and 17/18	-	25 km	-

We use Random Forest (RF) models (Breiman, 2001) to quantify how important each predictor variable is in determining the fitted values of $\Delta\text{AGB}_{14/15 \rightarrow 15/16}$ and the percentage of AGB recovery. Model performance metrics assessed were the mean absolute error (MAE) and the R-squared value (R²). The selected model has the smallest MAE and the highest R². The spatial patterns of the RF-predicted values are compared with the observed values in Figure 5-1.

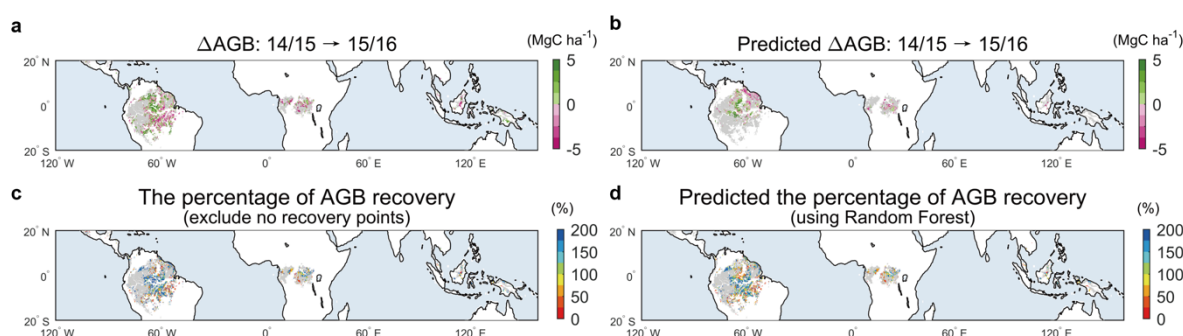


Figure 5-1: Spatial patterns of the AGB changes during the drought ($\Delta\text{AGB}_{14/15 \rightarrow 15/16}$) and the percentage of AGB recovery estimated (a), (c) by L-VOD AGB data and (b), (d) by Random Forest.

The observed recovery percentage could be classified into two categories, namely with recovery percentage less than 100% and equal to/greater than 100%. We tested if the RF-predicted recovery percentage could be classified into the proper category (Figure 5-2 and Table 5-2). Partial dependence plots based on RF are used to visualize the relationship between predictor variables and $\Delta\text{AGB}_{14/15 \rightarrow 15/16}$, the percentage of AGB recovery, independent of other predictor variables. The

predictor variables with flat response functions, i.e., no change in AGB response and recovery with the predictor variable, have negligible effect on estimation of response and recovery.

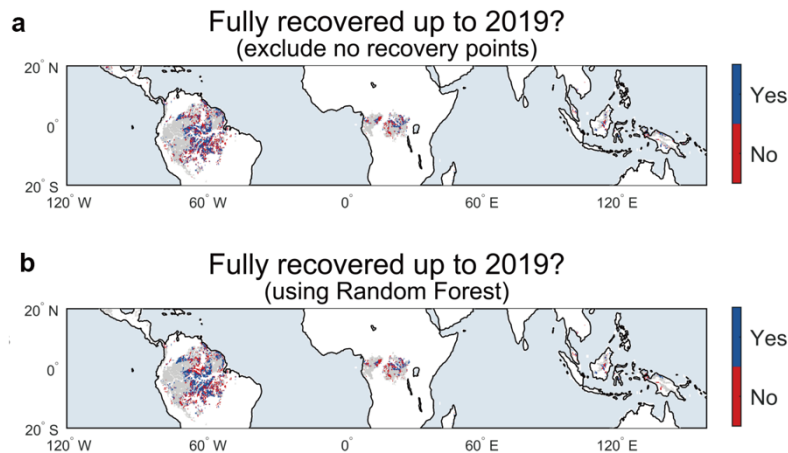


Figure 5-2: Spatial pattern of AGB fully-recovered and not fully recovered areas estimated (a) by L-VOD AGB data and (b) by Random Forest. The confusion matrix of the classification is in Table 5-2.

Table 5-2: The confusion matrix of the classification results using the Random Forest model. The classification is based on the RF-predicted and observed percentage of AGB recovery (%). “Yes” indicates that, by 2019, forest where AGB decreased has fully recovered to its pre-drought AGB level. “No” indicates that, by 2019, forest where AGB decreased has not fully recovered to its pre-drought AGB level.

	Predicted: No	Predicted: Yes
Actual: No	39.6% (Correct)	9.2% (Incorrect)
Actual: Yes	9.4% (Incorrect)	41.9% (Correct)

5.2. Severity, duration and onset timing of 2015/16 drought

Here, we assess the extent and severity of the 2015/16 drought using the standardized anomaly of cumulative water deficits (ACWD) derived from monthly precipitation measured by the Tropical Rainfall Measuring Mission (TRMM) and evapotranspiration from the Global Land Evaporation Amsterdam Model (GLEAM; Marten et al., 2017) (see section 5.1.3). This study only focuses on the tropical intact evergreen forests, using a conservative intact forest cover mask to avoid misclassification of drought over the non-forested or anthropogenic disturbance-affected regions (see section 5.1.2). Since mid-2015, more than 55% of tropical intact evergreen forests in South America (2.53 million km²), 34% in Africa (0.40 million km²) and 42% in Southeast Asia (0.19 million km²) were exposed to ACWD < -1 SD for more than three months (SD is the standard deviation during the period

2010-2019). The patterns shown in Figure 5-3 illustrate the severity (Figure 5-3a), duration (Figure 5-3b) and onset time (Figure 5-3c) of the 2015/16 drought. The drought first hit Southeast Asia, then Africa and South America (Figure 5-3c). Drought duration and severity differed spatially, and the areas under more severe drought tended to have a longer-lasting exposure. The epicenter of drought is in central Amazonia, where rainforests experienced ACWD < -2 SD for more than 8 months. By contrast, the drought was less severe for the forests in eastern Amazonia and in most parts of Africa and was relatively short-lasting (less than 6 months) in western Africa and Southeast Asia. Note that using the MODIS ET product instead of GLEAM to calculate ACWD gives similar patterns of drought severity and duration.

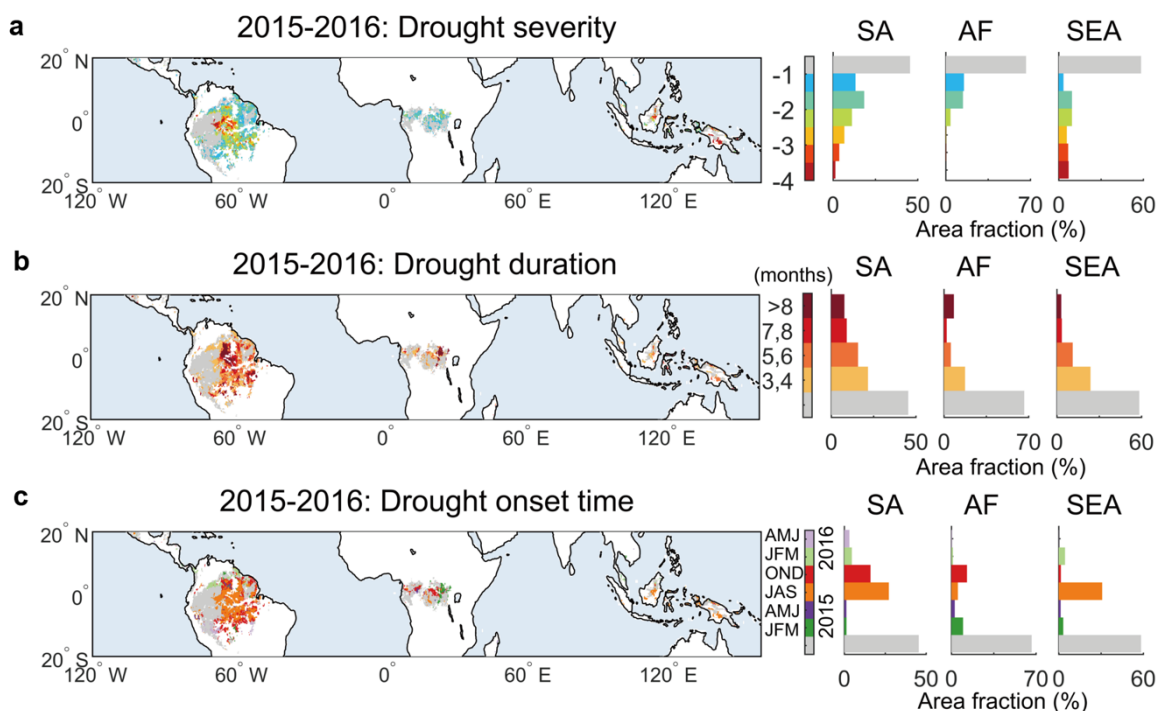


Figure 5-3: Spatial patterns of the (a) severity, (b) duration and (c) onset time of the 2015/16 drought over the tropical evergreen forests. The severity, duration and onset of drought are identified based on the standardized anomaly of monthly Cumulative Water deficit anomalies (ACWD). The left-hand panels show the fractional area of tropical forests sorted into different categories of drought severity, duration and onset time. The fractional area is split into values for three continents, i.e., South America (SA), Africa (AF) and Southeast Asia (SEA). The non-forest dominated regions, forest losses regions, flooded and lake areas are masked out.

5.3.Changes in AGB during and after drought

We examined the impact of the 2015/16 drought on forest AGB using L-VOD (L-band vegetation optical depth) data (Wigneron et al., 2017). Changes in AGB stocks during the 2015/16 drought period, relative to the same month during the pre-drought year ($\Delta\text{AGB}_{14/15 \rightarrow 15/16}$, see Method for the definition of this notation) are calculated for 25km pixels over tropical intact evergreen forests that were exposed to drought.

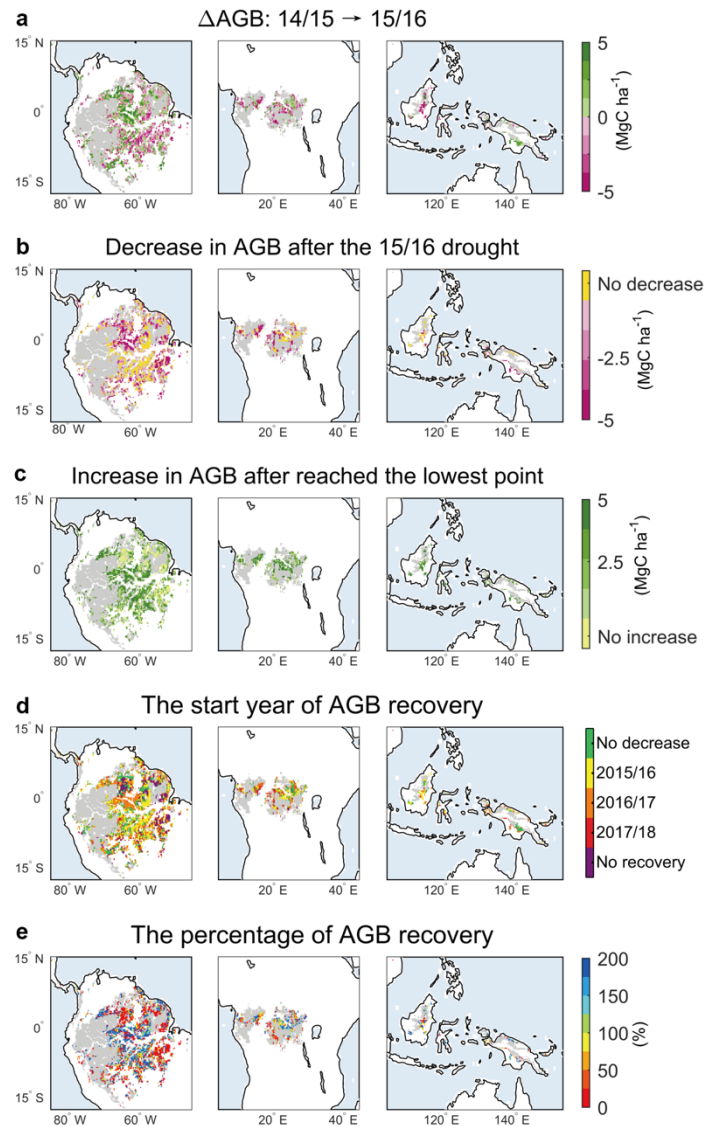




Figure 5-4: Spatial patterns of forest AGB changes during and after the drought. (a) Changes in AGB over the drought period in 2015/16, relative to AGB over the same period in 2014/15 (Δ AGB_{14/15 \rightarrow 15/16); (b) Decreases in AGB after the drought; (c) Increases in AGB after reached the lowest AGB point; (d) The start year of AGB recovery, i.e. the year with the lowest AGB value. Green areas correspond to areas where AGB has not reduced over the period of 2015 and 2016. Yellow areas correspond to areas where AGB in 2015/16 was the lowest and regrows immediately after the drought. Purple areas correspond to areas where AGB has not started to recover by 2019. (e) The percentage of AGB recovery, i.e., the increase in AGB after the lowest point divided by the sum of decrease in AGB during and/or after the drought.}

The results shown in Figure 5-4a indicate an immediate AGB reduction during the 2015/16 drought period over more than 60% of drought-affected intact wet forests, particularly in south-eastern Amazonia, and in most forests of Africa and Borneo of Southeast Asia. By contrast, wet rainforests in central Amazonia showed an increase in AGB during the drought period. Lagged tree mortality post-drought but with no significant reduction in the growth of surviving trees has been observed at one rainfall exclusion experimental site in Caxiuana (Rowland et al., 2015), at ecological monitoring sites in the Amazon during the 2010 drought (Doughty et al., 2018), and in a variety of tree genera globally

	Ref	CCI Biomass Climate Assessment Report v3		
	Issue	Page	Date	
	3.0	55	14.07.2021	

(Trugman et al., 2018). The lack of suppressed tree growth or enhanced growth during the drought may be due to increased canopy photosynthetic capacity (Saleska et al., 2016) from greater radiation availability (Guan et al., 2015), flushing of young and more efficient leaves in the early drought stages (Wu et al., 2016; Chen et al., 2020), and increased vapor pressure deficit (VPD) resulting in an increase of water use efficiency offsetting the regulation of stomatal closure, leading to a net increase of canopy photosynthesis (Green et al., in review).

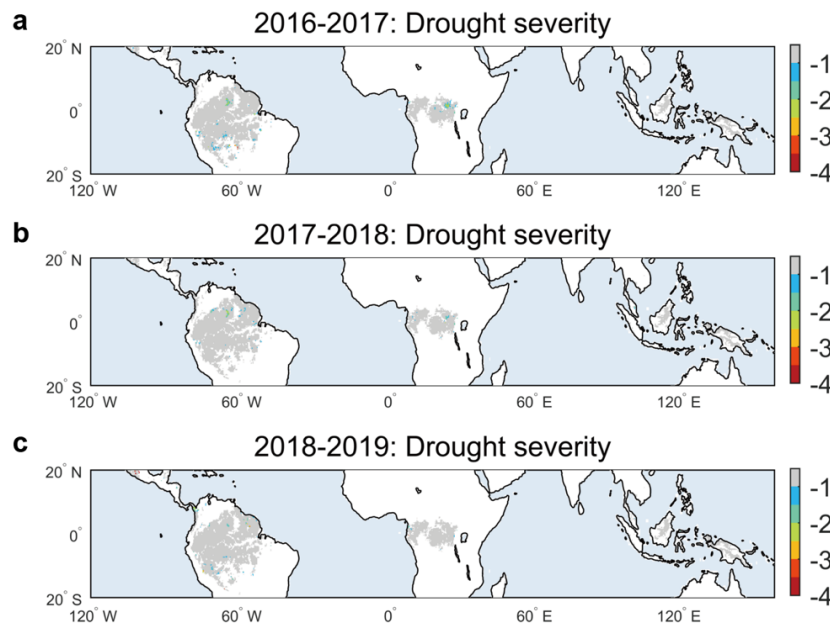


Figure 5-5: Spatial patterns of the median of ACWD (i.e. the severity of drought) over the same drought month in 2016/17, 2017/18 and 2018/19. Note that the GLEAM ET data of year 2019 are not available, so we use a constant ET of 100 mm month⁻¹ to calculate ACWD in 2019 (Aragão et al., 2007).

The post-drought trajectories of AGB shown in Figure 5-4b and 5-4c are more complex and differ among regions. On the one hand, a lagged persistent decrease in AGB can be seen in Figure 5-4b after the termination of the 2015/16 drought in north-central and eastern Amazonian and western Congo forests (Figure 5-4b), despite the gradual recovery of rainfall and no new drought event (Figure 5-5). The occurrence of fires in subsequent years, in particular during 2017/18, may be partly responsible for additional AGB reduction after the drought, for example in the eastern Amazon (Figure 5-6). A lagged decrease of AGB is consistent with findings based on satellite laser altimeter data of a lagged loss of height over intact forests in the epicenter of the 2005 drought in the Amazon (Saatchi et al., 2013; Yang et al., 2018). On the other hand, after reaching the lowest AGB point, the trend of AGB reversed and more than 80% of the regions where AGB losses occurred showed a recovery of AGB before 2019 (Figure 5-4c). Divergent post-drought recovery trajectories are also evident. Some forests regrew after the drought of 2015/16 whereas others declined in a few subsequent years. As shown in Figure 5-4d and Figure 5-6, quickly-recovering forests correspond roughly to those previously exposed to moderate or light drought in eastern Amazonia, most parts of Africa and Southeast Asia. Conversely, late-recovering forests are in south-central Amazonia where the drought was more severe. The regions where AGB started to recover earlier also show a higher recovery level (Figure 5-4e). By 2019, more than about 44% of intact forests where AGB decreased have fully recovered to their pre-drought AGB level. The regions where AGB did not show any recovery or did not fully recover in 2019 include regions in the epicenter of the drought – north-central Amazonian forests, as well as dryer eastern Amazonia and western African regions near the edge of the intact tropical forest biome. Trees near the forest

edges are most likely more vulnerable to intense fires, canopy drying, and degradation (Brando et al., 2014), which could favor tree mortality and a lack of AGB recovery.

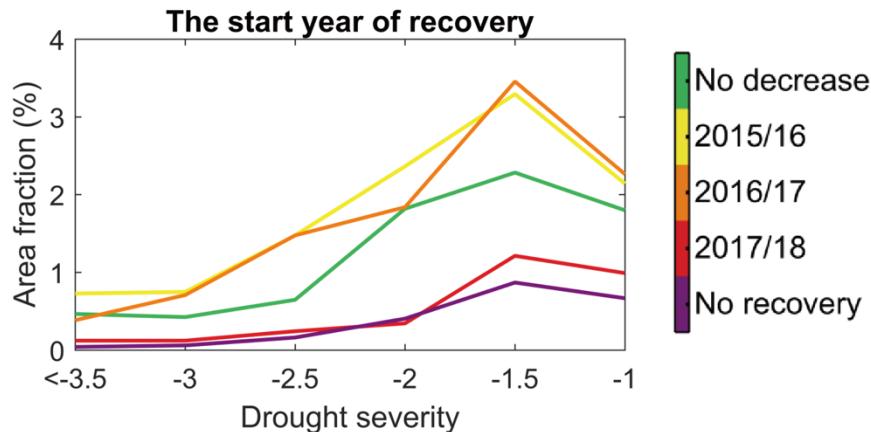




Figure 5-6: The relationship between the drought severity and the start year of AGB recovery, that is also the year with the lowest AGB value. The fractions of the study area (%) with different start year of AGB recovery are shown.

5.4. Factors influencing AGB changes during and after drought

The factors that determine AGB changes during drought and its subsequent trajectory are complex and can be related to exposure and vulnerability of forests. We used Random Forests (RF) models (ref. 28; see section 5.1.5) to investigate the importance of more than twenty factors, including drought characteristics, background climate, soil properties, forest structure and fire occurrence (Table 5-1). Altogether, these factors explained 67% of the variation of the observed changes in AGB during drought ($\Delta\text{AGB}_{14/15 \rightarrow 15/16}$; Figure 5-7) and 43% of the variation of the observed percentage of AGB recovery relative to all the losses of AGB (log-transformed) (Figure 5-8). The Random Forest models exhibit good predictive skill in reproducing the observed spatial patterns of AGB changes during drought and their recovery percentage (Figure 5-1). Despite biases in predicting locally the recovery percentage, the Random Forest model properly identified regions with full versus incomplete recovery, with 81% accuracy (Figure 5-2; confusion matrix in Table 5-2). Partial dependence plots to illustrate the non-linear dependence of AGB changes on different predictors are shown in Figures 5-7 and 5-8 for the six most influential factors in each best Random Forest model.

5.4.1. AGB changes during the drought

Figure 5-7 shows that soil moisture changes during the drought year ($\Delta\text{SM}_{14/15 \rightarrow 15/16}$) are the most influential factor associated with AGB changes of $\Delta\text{AGB}_{14/15 \rightarrow 15/16}$. Unsurprisingly, larger soil moisture deficits relative to the pre-drought level are associated with more losses of AGB during the drought. The previous study assessed the forest aboveground biomass during 2005 drought using long-term monitoring plot observations, indicating that these losses during the drought were mainly driven by large mortality increases rather than by declines in growth (Phillips et al., 2009).

	Ref	CCI Biomass Climate Assessment Report v3		
	Issue	Page	Date	
	3.0	57	14.07.2021	

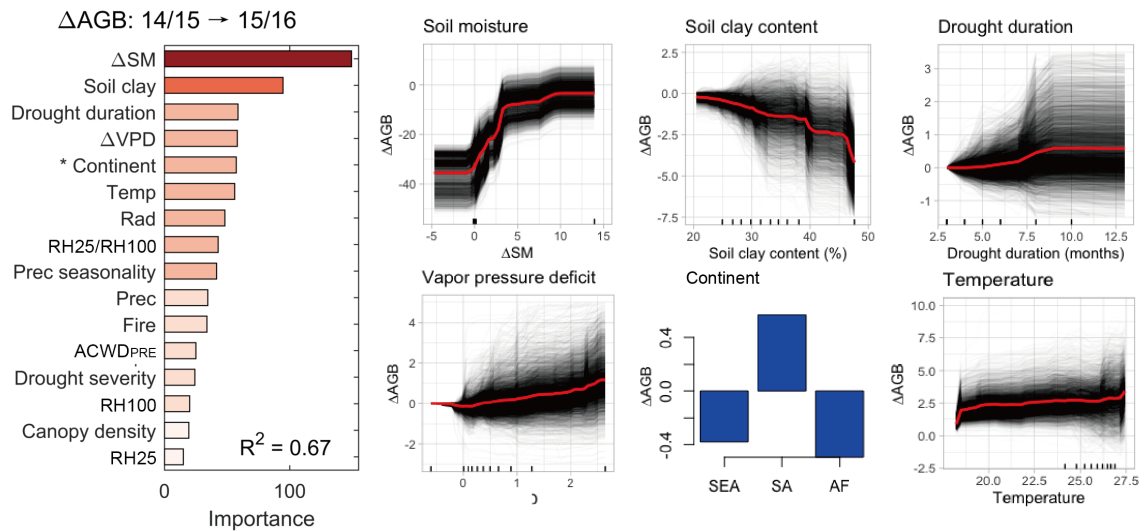


Figure 5-7: The importance of predictor variables in fitting the AGB changes during the drought ($\Delta\text{AGB}_{14/15 \rightarrow 15/16}$), and partial dependence plots for the 6 most important variables. In the partial dependence plot, the red line is the partial dependence curve, showing the relationship between one specific predictor variable and $\Delta\text{AGB}_{14/15 \rightarrow 15/16}$, independent of other predictor variables. Black lines are the individual conditional expectation curves, displaying the dependence of $\Delta\text{AGB}_{14/15 \rightarrow 15/16}$ on corresponding predictor variables for each pixel. Ticks on the x-axis show the deciles of the distribution of the predictors.

High soil clay content is also strongly positively associated with AGB reduction during drought. Two possible mechanisms may explain this. First, the higher wilting point of clay-dominated soils limits soil moisture available for plant roots (Frensham et al., 2015). Second, the higher nutrient availability in clay soils may play a detrimental role during drought, as forests growing in clay soils with a larger nutrient content, particularly phosphorus, may be adapted to higher nutrient use, leading to a higher embolism risk under severe water stress (Gessler et al., 2017; Soong et al., 2020). The RF model also indicates that a longer drought duration is associated with an AGB increase during the drought year in north-central Amazonia (Figure 5-3b and Figure 5-4a). This is likely a confounding effect of the fact that in this region, the available water resource is always high and trees have deep rooting systems, which enable them to access water at deep depths. The RF model also indicates that a higher VPD is associated with an increase of AGB during drought. A possible reason is that in the wet tropics, the increase in intrinsic water use efficiency (iWUE) coincident with higher radiation, better diffusion in dry leaves during drought may translate into high photosynthesis despite stomatal closure at high VPD levels (Zhang et al., 2019; Green et al., in review). Background mean annual temperature with little spatial variation (Burton et al., 2018) is ranked 6th in terms of importance in the RF models, thus having little effect on AGB response during drought. This differs from the results from space-for-time substitution which demonstrate a limiting long-term effect of high temperatures on photosynthesis (Huang et al., 2019), and on carbon stocks, carbon gains and carbon turnover rate (Sullivan et al., 2020).

5.4.2. AGB recovery

As shown in Figure 5-8, AGB changes during the El Niño drought year is the factor most strongly associated with the percentage of AGB recovery, according to our RF model. Pixels with a more negative $\Delta\text{AGB}_{14/15 \rightarrow 15/16}$ are generally associated with no legacy of AGB recovery after the drought (Figure 5-9) so that the minimum of AGB was reached just after the drought period.

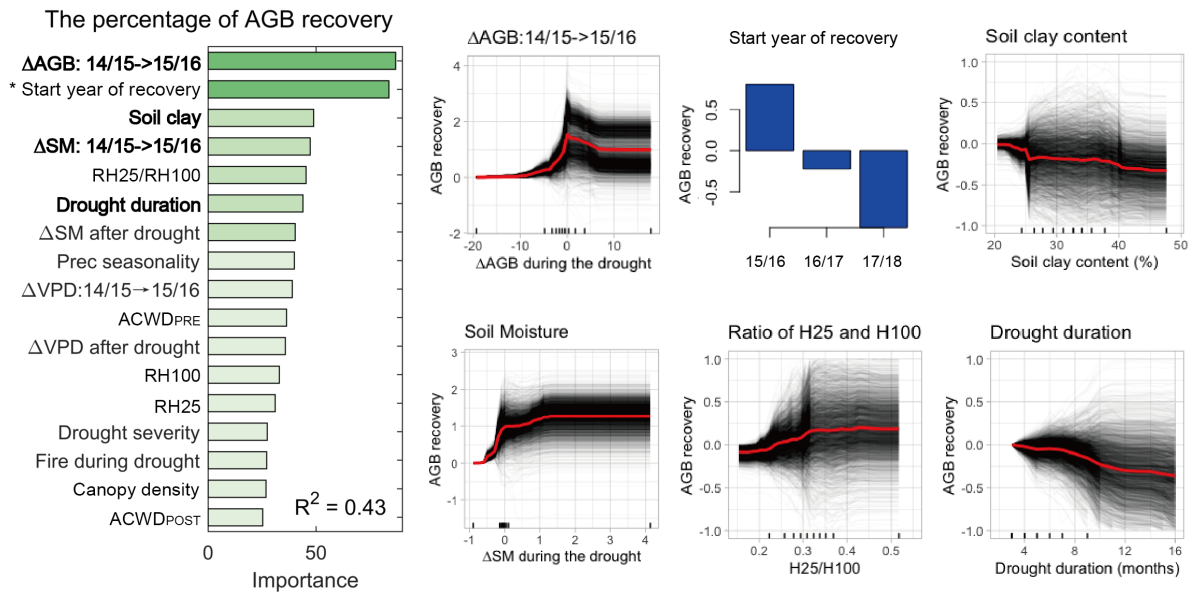


Figure 5-8: Same as Figure 5-7, but for the log-transformed the percentage of AGB recovery after drought (excluding no recovery pixels). The predictors in bold are the factors strongly associated with $\Delta\text{AGB}_{14/15 \rightarrow 15/16}$ in Figure 5-7.

Partial dependence graphs in Figure 5-8 show that greater losses of AGB during drought are associated with a lower recovery percentage (recovery percentage was calculated as the increase in AGB after the lowest AGB point divided by the sum of decreases in AGB during and after the drought, see section 5.1.4). Conversely, regions with positive $\Delta\text{AGB}_{14/15 \rightarrow 15/16}$ during the drought in central Amazon tend to show lagged AGB loss after the drought and lower recovery (Figure 5-9 and Figure 5-8). Thus, the AGB change during the drought, irrespective of its sign, is a strong predictor of the post-drought AGB recovery. Soil moisture changes during the drought year ($\Delta\text{SM}_{14/15 \rightarrow 15/16}$) and soil clay content, which were the strongest two predictors of the AGB response during drought, are also positively associated with the percentage of AGB recovery (Figure 5-8). Long-lasting drought is associated with low recovery level of AGB (Figure 5-8). Apart from those factors (i.e. $\Delta\text{AGB}_{14/15 \rightarrow 15/16}$, $\Delta\text{SM}_{14/15 \rightarrow 15/16}$, soil clay content and drought duration) found to be influential for AGB changes during drought, the start year of the AGB recovery plays the second most important role in explaining the post-drought AGB recovery percentage: the sooner forests start to recover, the higher recovery percentage they can reach within the observed time-frame.

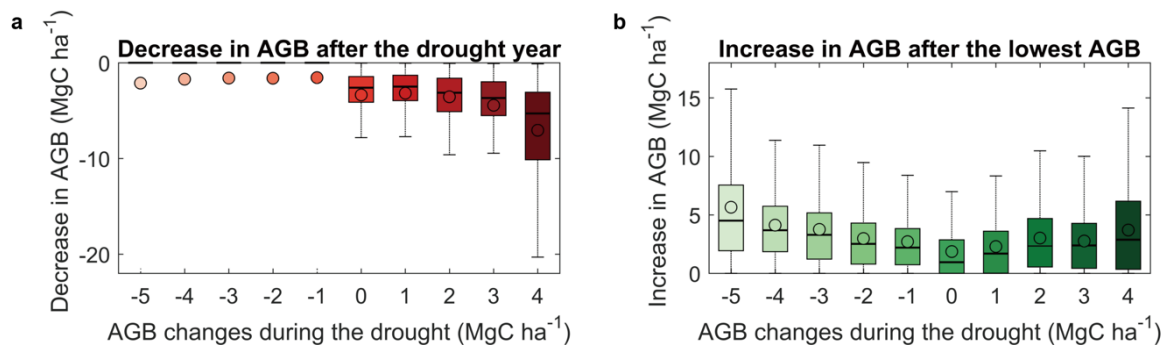


Figure 5-9: Relationship between AGB changes during the drought ($\Delta\text{AGB}_{14/15 \rightarrow 15/16}$, Figure 5-4a) and AGB changes after the drought.

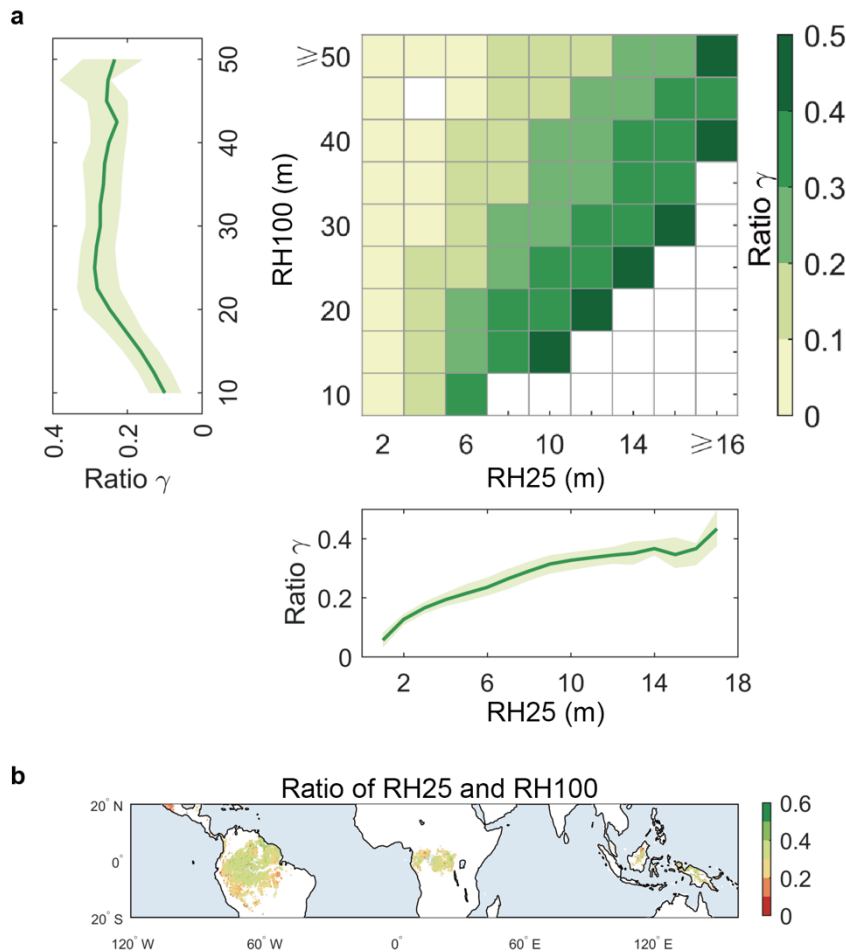


Figure 5-10: (a) The relationships between the understory height (RH25), canopy height (RH100) and their ratio γ . (b) Spatial pattern of the ratio of RH25 and RH100.

In addition, we found that the vertical structure of forests, referred as to γ and defined as the ratio of understory height (RH25) to top height (RH100) from satellite laser altimeter data (Harding and Carabajal, 2005) also positively influences the recovery of AGB after the drought. γ is higher in forests with closed canopy where the understory height is closer to the top canopy height. Generally, γ increases spatially with understory height (Figure 5-10). Some forests with high canopies (≥ 30 m) and low γ (< 0.3) are geographically distributed near to the intact forest biome edges (Figure 5-10), and may be a mosaic of forests of variable height. While most previous studies on forest dynamics looked at total canopy height only (e.g. Yang et al., 2018; Bennett et al., 2015; Stovall et al., 2019), the importance of accounting for forest structure has been increasingly recognized., and canopy structural complexity and vertical canopy profile have been used to predict forest dynamics (Condit et al., 1996; Rödiger et al., 2018; Stark et al., 2012; Fahey et al., 2015). In Figure 5-11, we compare the start year of recovery and the mean annual AGB recovery percentage between high γ (≥ 0.3) and low γ (< 0.3) forests for different levels of soil water deficit. In all cases, high γ forests have a stronger capacity to recover than low γ ones. A possible explanation is that low water availability and high evaporative demand make it difficult for tall dominant trees with crowns closing the upper canopy to maintain leaves and hydraulic safety (da Costa et al., 2010; Arellano et al., 2019). In contrast, understory/small trees are more likely to survive during and after drought, according to meta-analysis and theoretical model results (Trugman et al., 2018; Bennett et al., 2015). Thus, understory trees can even enhance their growth when more light reaches the understory and competition for water is alleviated when there is

mortality or leaf loss from tall trees (Rowland et al., 2015; McDowell et al., 2018). This suggests that a loss of carbon due to mortality of tall trees could be offset by carbon gains in understory trees, explaining why forests with a high γ were found to recover better.

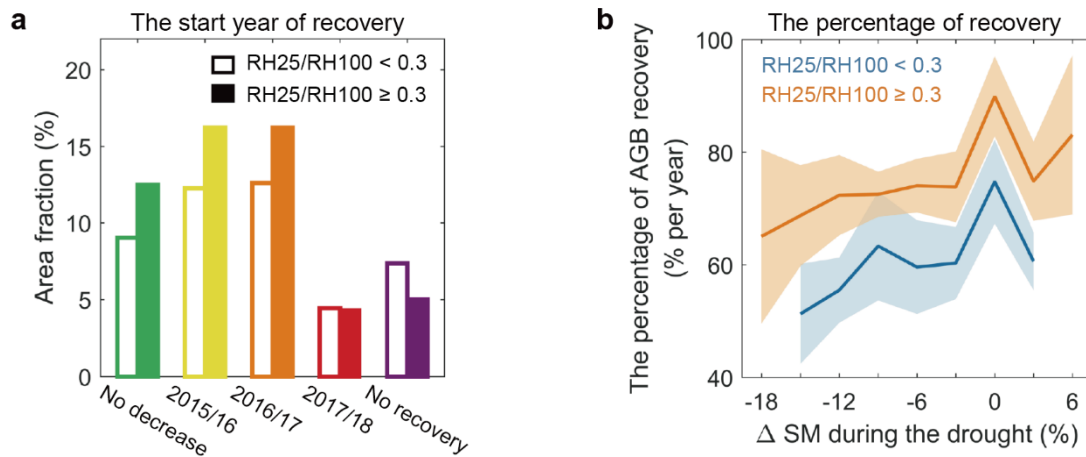




Figure 5-11: (a) The start year of AGB recovery and (b) the percentage of AGB recovery per year (% per year) of canopy-closed forests where the understory height is close to the top canopy height ($\gamma \geq 0.3$), and forests with low understory ($\gamma < 0.3$). In (a), the fraction of study area (%) with different start year of AGB recovery are shown. In (b), the median of the percentage of AGB recovery per year (% per year) are calculated for different levels of soil moisture deficits during the drought year.

The tropical drought in 2015/16 by ENSO occurred primarily in the wet season. Following previous studies (Wigneron et al., 2020; Brandt et al., 2018; Fan et al., 2019), our results of forest AGB changes during the drought period (wet season) are retrieved from L-VOD dataset, based on the assumption that seasonal averages of vegetation water content and above-ground biomass are correlated over time. However, water percolation into the ground/roots might lead to the changes in vegetation water content lagging behind the biomass (Feldman et al., 2018), which could increase uncertainty in the L-VOD-derived biomass estimates. Also, L-VOD product is known to have reduced sensitivity in high biomass regions, and this could result in underestimation of AGB (Wigneron et al., 2020).

As a consequence, forest AGB changes during the 2015/16 drought, both positive and negative, are associated with drought severity (soil water deficit) and duration, as well as with soil clay content. AGB recovery after the drought is influenced by previous AGB losses, modulated by climatic water deficit, soil clay fraction and vertical forest structure. Note that we found the same influential variables for absolute AGB recovery after the drought as for relative changes. Our results shed light on the attribution of AGB changes during and after droughts to drivers, showing that predicting the long-term impact of drought on forest communities is challenging, because drought also influences demographic processes beyond immediate growth and mortality during drought exposure. The driving role of forest structure suggesting compensatory responses of taller trees and understory trees to drought needs to be confirmed by ground-based inventories and drought experiments results. Moreover, as the climate extreme event is expected to move towards more compound, frequent, severe and long-lasting in the future (Seveviratne et al., 2012; Zscheischler et al., 2018), a better understanding of the response and recovery of tropical forest dynamics during and after drought can provide valuable information for the climate modelling community, in order to more accurately predict ecosystem response to drought events under future climate change scenarios.

	Ref	CCI Biomass Climate Assessment Report v3		
	Issue	Page	Date	
	3.0	61	14.07.2021	

6. Biomass change products

There are two main ways of estimating biomass change, a change in the signal or a difference in estimated biomass values over time. Changes in sensor signals are difficult to use as multiple sensors with different characteristics cover different time periods.

The most promising sensor for which signal change can be transformed into biomass (AGB) change is the SMOS-IC L-band VOD that was found to be linearly related to biomass. This relationship was used to infer temporal changes since 2010. However, L-VOD has some limitations in tracking biomass changes and its resolution is coarse, so that biomass changes at its 25 km gridded resolution cannot be easily attributed to different processes, such as e.g. deforestation, degradation and forest regrowth occurring in the same pixel:

- 1) Values of AGB change are provided in each 25 km resolution grid-cell in which both forest AGB loss and gain can occur. So L-VOD gives an integrated estimate of biomass change but will require additional data to attribute the observed changes to different sub-grid processes in case of highly dynamic AGB change processes that have different signs, such as in the tropics, where we may have primary forest deforestation, secondary forest growth, secondary forest deforestation, fires, degradation, etc. in the same 25 x 25 km grid cell.
- 2) The signal of dielectric properties of vegetation on sub-annual time scales related to changes in water content is hard to filter from biomass change and, for applications like those in Section 5, we have used mean L-VOD over a period of two years, or only wet season maximum L-VOD values.
- 3) Possible saturation of L-VOD-AGB relations for $AGB > 200 \text{ t ha}^{-1}$ Further, the validation of L-VOD against plot-scale point data is challenging because L-VOD data reflect the status of an entire area of 25 x 25km, not that of a relatively small plot, and the median or tall trees are more easily to be measured relative to the small trees by inventories using in-situ height and and DBH to infer tree biomass. This means L-VOD AGB data can underestimate AGB and AGB change in dense forest regions, but we don't know the extent of this possible systematic error in L-VOD AGB.
- 4) The quality of VOD (here SMOC-IC L-VOD) depends on the region where it is applied because of RFI (non-stationary noise, unfortunately). RFI can partly be diagnosed from the difference between ascending and descending orbits. From the experience of LSCE working with the team of J.P. Wigneron, VOD appears reliable for AGB change in the tropics and Australia. It has also been used successfully in Southern China and preliminary results from Siberia look good. North America and Europe need more work on the RFI filtering.

Nevertheless, a number of successful applications of L-VOD for AGB change have been produced recently and are illustrated below.

- 1) Consistency between combining low resolution L-VOD datasets and high-resolution datasets (e.g. forest cover change multiplied by static AGB at high resolution, or optical sensor-based AGB changes like Baccini et al., 2017) was shown to be achievable in regions where AGB is highly dynamic, such as some Amazon regions or Southern China (Figure 6-1). However, for regions that are less dynamic, it will be more difficult to assess smaller signals. L-VOD and forest area change from high resolution data are very well correlated for Amazon deforestation pixels (Figure 3; Qin et al. Nature Climate, 2021).

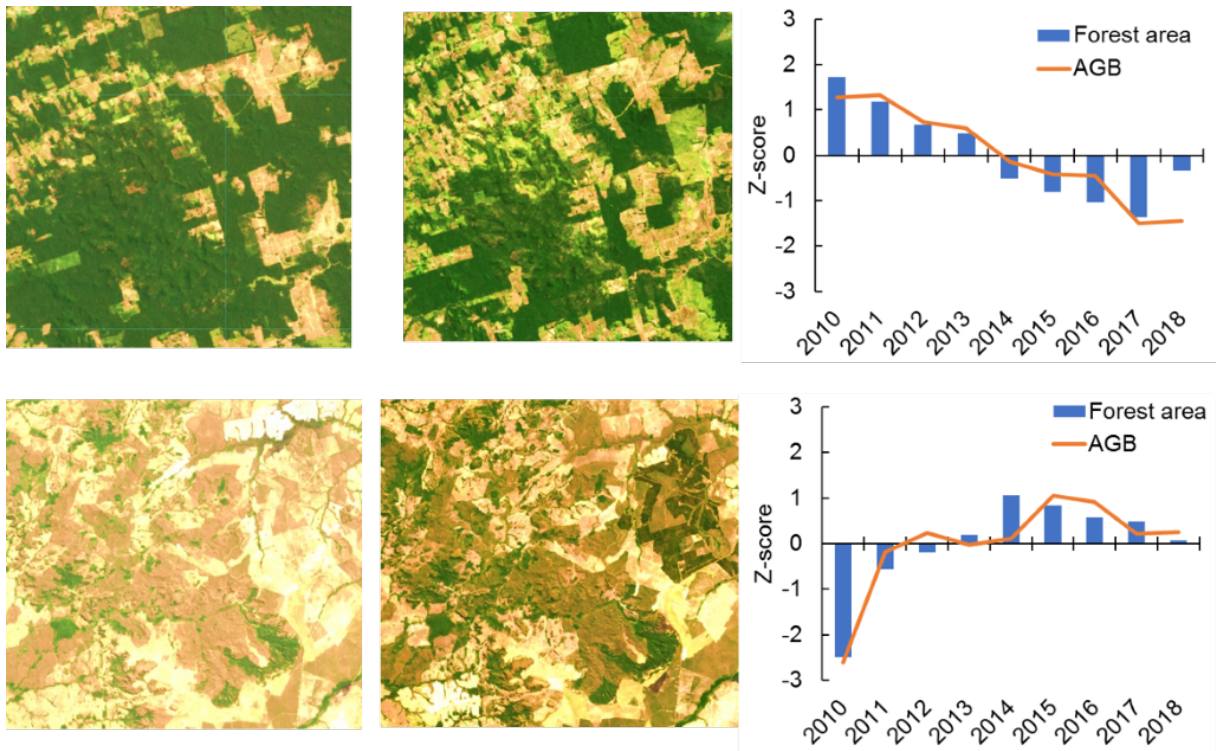


Figure 6-1: The link between Amazon deforestation (area loss) and L-VOD.

The global biomass loss derived from L-VOD also agrees well with forest area loss in the tropics (the two datasets are independent), as shown in Figure 6-2 (Fan et al. 2019).

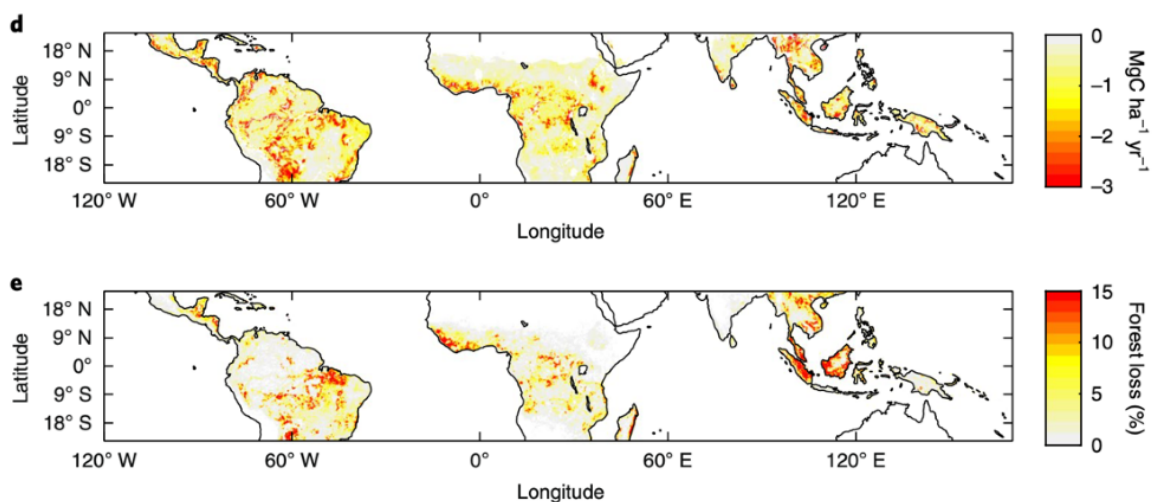


Figure 6-2: The correspondence between L-VOD and Landsat-derived forest loss.

Very good correspondence was observed (Figure 6-3) in Southern China between MODIS and Landsat C stocks and L-VOD, and changes of C stocks from SMOS in this region, which is experiencing a fast change in management (Tong et al., 2020). Similarly, AGB loss from L-VOD in 2019 from Australian fires and forest area loss from MODIS-PALSAR are comparable (Qin et al. Nature Climate 2021).

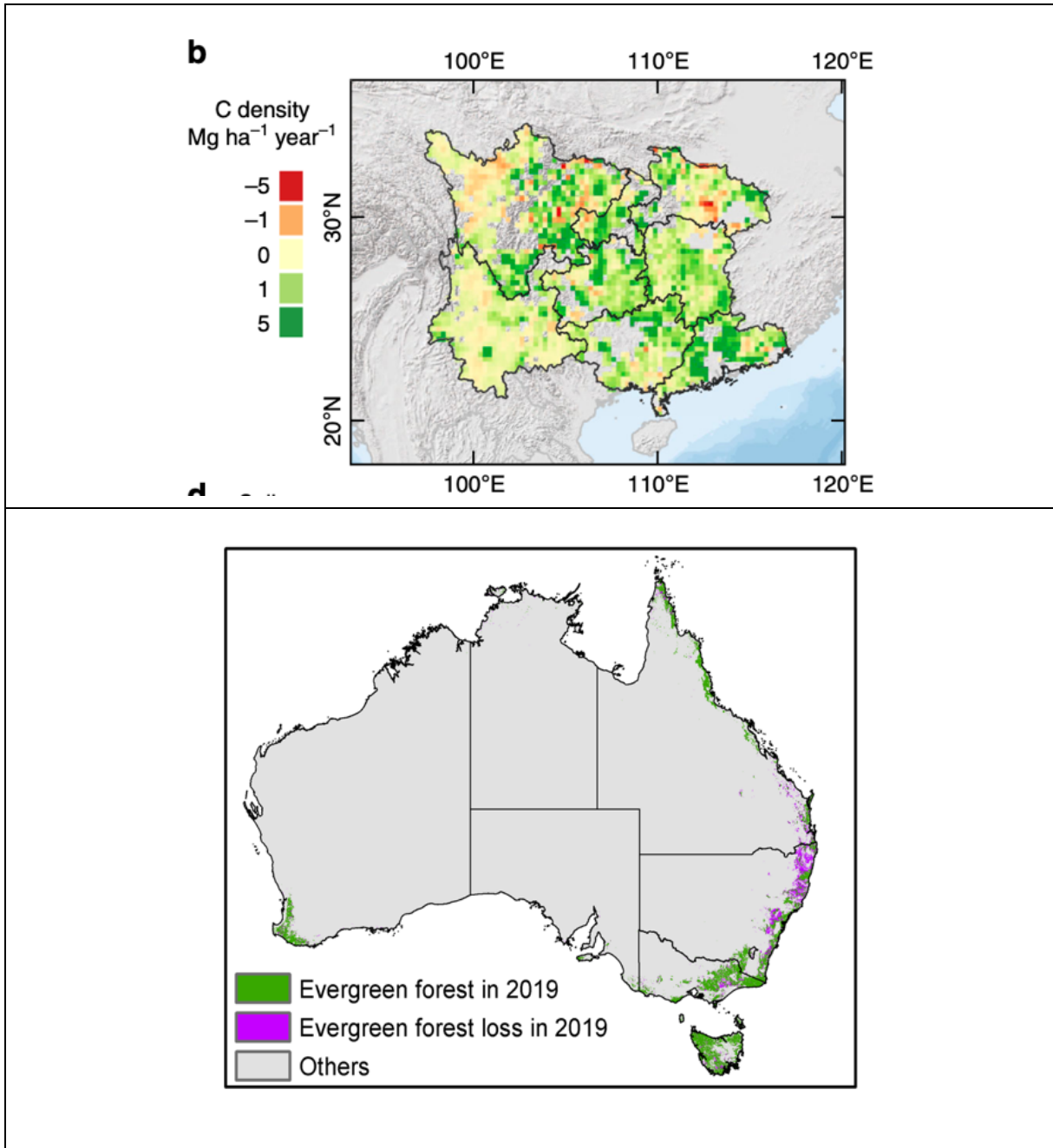




Figure 6-3: Corresponding changes in AGB retrieved from L-VOD for China and Australia.

Measuring biomass change is not just an issue of the biomass difference. A change of say 40 t/ha in a low biomass forest may be measurable with good accuracy while for a high biomass forest it may be less than the measurement noise. Two numbers are essential for quantifying the error in biomass change: bias and precision (which is independent of bias and quantifies the scatter in the estimates). Both of these may depend on the true value of AGB. When averaging multiple estimates, e.g. several times of year, and if the bias for every estimate is the same, the precision will improve but not the accuracy if errors have a temporal autocorrelation. If the bias is constant over time or between products from two sensors, it can still affect the estimated change of AGB. The worst case is when bias

	Ref	CCI Biomass Climate Assessment Report v3		
	Issue	Page	Date	
	3.0	64	14.07.2021	

changes over time, e.g. when using two different sensors. Then the change of AGB can be biased both by the bias of each sensor /product and the bias changes over time.

There are therefore two relevant questions: How likely is a biomass change to be observed (and will prior knowledge help)? How accurate is the change estimate (which depends on knowing the error properties of the AGB estimates)? Answering the second question is difficult if the bias or precision varies with AGB, as was been seen in the GlobBiomass or CCI Biomass products; we therefore need to develop a bias and precision model for the data. An error model should be developed which could vary depending on biomass level and region; without this we cannot approach this problem in any real quantitative sense. The validation exercise is therefore crucial as it should provide the basis for this, but we can also use the assessment exercises by Gamma and WP4000 to offer insight (and, even better, numbers).

From a global modelling user point of view, notional accuracy requirements for change mapping can be based on DGVM simulations at 0.5° (typically $\approx 1 \text{ Mg ha}^{-1}$ per 0.5° model grid cell). However, in the real world, within a 0.5° grid cell some areas are losing and some gaining biomass. So this notional accuracy at 0.5° requirement has to be split into accuracy of loss (subgrid) and accuracy of gain from regrowth (subgrid) when using high resolution EO data to arrive at a mean accuracy at 0.5° for each model grid-cell when using high resolution datasets like CCI Biomass (100m) or Saatchi et al. Biomass maps (1 km). AGB gains in growing forest are a function of prior AGB. Further, AGB gains at low AGB should be easier to measure than lower AGB gains at high AGB, due to, e.g. saturation at high AGB and smaller growth for high AGB systems. This means accuracy at 0.5° will depend on the proportions of high and low biomass, which differ between regions.

7. Forest edge biomass carbon deficits in Africa

African forests show fragmentation that causes forest degradation near forest edges. The impact of fires used for slash-and-burn on forest edge effects remains unclear. Using high-resolution (30 m \times 30 m) satellite-based forest cover and the CCI biomass data sets, we found that edge effects extend $0.11_{-0.04}^{+0.06}$ km (median and interquartile range) and $0.15_{-0.05}^{+0.09}$ km into moist and dry forests. The biomass within the forest edge zones has a total carbon deficit for the African continent of 4.1 Pg C ($16.1_{-5.9}^{+8.0}$ Mg C ha⁻¹). Fires occurred in 52% of the forest edges and produce a carbon deficit higher by $5.5_{-2.9}^{+4.3}$ Mg C ha⁻¹ than non-fire edges. This effect can be explained by direct impact (fires intruding into forests) and indirect impact (increasing canopy dryness). If small-scale slash-and-burn practices continue, increasing fragmentation during 2010-2100, we predict a cumulative committed carbon loss from edge effects of 0.54-4.6 Pg C, which could be avoided by implementing dedicated forest protection policies, supported by satellite monitoring of forest edges. African tropical forests are the largest stores of biomass carbon in terrestrial ecosystems but are exposed to anthropogenic disturbances causing deforestation and degradation and to fires. Estimates of carbon losses from land use and land cover change (LULCC) and forest degradation may be underestimated because small-scale disturbances are not captured with moderate to high (Landsat) resolution sensors. Small-scale disturbances are increased by fragmentation, caused by diverse human activities such as logging, road development, cattle ranching and small-scale farming, which leads to small and irregularly shaped forest patches, increasing the area of forest edges. Further, close to disturbance affected areas, drying conditions and enhanced wind turbulence, tend to make biomass carbon e lower within the forest edge zones than in the forest interior (i.e. edge effects) as observed from field studies and using remote sensing data with relatively coarse resolution.

The African forest is one of the most productive and high biomass-density ecosystems in the world, but it is threatened by growing timber demands and fast population growth increasing shifting

cultivation. In the central Congo basin, LULCC appears to have shifted from large-scale industrial deforestation to clearing by smallholders for farming, leading to higher forest fragmentation. Lower precipitation, soil moisture and evapotranspiration in the vicinity of burnt areas slows forest recovery and may enhance edge-induced carbon loss.

The material in this section has been published in Zhao et al. (2021).

7.1. Forest Edge characteristics and AGB deficits compared to interior forests

We combined high-resolution remote sensing datasets of forest cover and forest AGB around the year 2010 from the CCI project (Globbiomass) with burned area data from the ESA CCI Fire project (Chiuveco et al. 2019) to forest edge AGB deficits at fire and non-fire edges over grid cells of 0.25°. Forests were divided into moist and dry forests. Two indicators were used to characterize edge effects on AGB, scale and magnitude. The scale parameter (km) is defined as the distance to the edge at which AGB equals 90% of that of the interior forest. The magnitude parameter is the relative difference in AGB between the edge and interior of forests. We estimated the AGB carbon deficit within forest edge zones (i.e., where the distance to edge was smaller than the scale in each grid cell). The carbon deficit is the difference in AGB between forest edges and interior forests, because the present edges include both long-established edges and recently created ones. The long-established edges reflect an equilibrium state of carbon stocks and do not result in any additional carbon change exchanged with the atmosphere, while recently created edges result in carbon loss and represent an elusive component of global LULCC emissions.

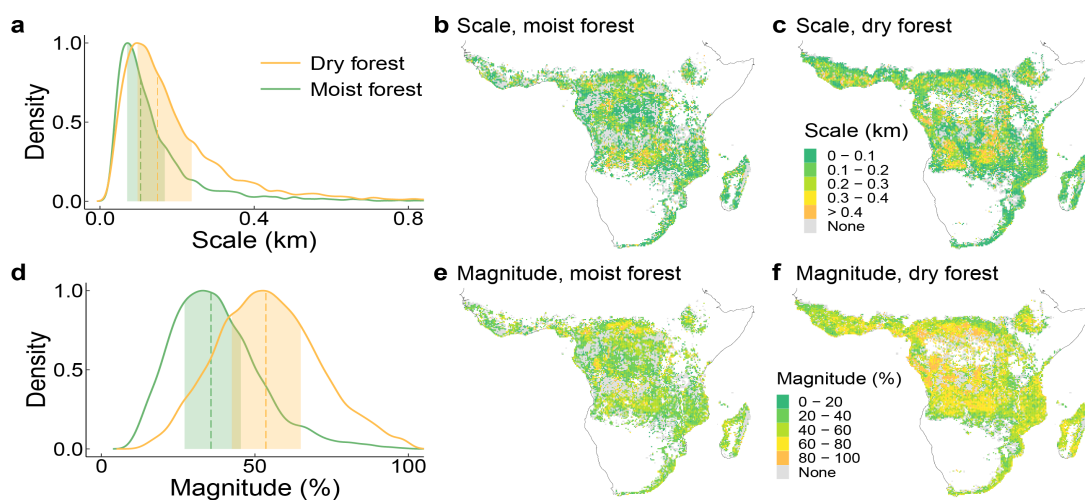




Figure 7-1: Scales and magnitudes of forest edge in Africa. (a) and (d) are the frequency distributions of scales and magnitudes; (b-c) and (e-f) are maps of scales and magnitudes. Shading in (a) and (d) indicates the weighted interquartile ranges, and dashed lines indicate weighted medians. Gray area in (b), (c), (e) and (f) indicates grid cells without detected edge effects (27% and 18% of all grid cells for moist and dry forests).

The scales of edge effects for moist and dry forests are $0.11_{-0.04}^{+0.06}$ km (median and interquartile range weighted by forest area) and $0.15_{-0.05}^{+0.09}$ km, and magnitudes are 36_{-9}^{+10} % and 54_{-11}^{+12} %, respectively (Fig 7-2). Edge effects have longer scale and greater magnitude in dry forests than in moist forests. We detected more grid cells with an edge effect in dry forests. Both moist and dry forests surrounding the Congo basin show edge effects with higher scales and magnitudes than in other areas (Fig. 7-2). Large edge effects were also found in the dry forests of regions along the Guinean gulf. Total AGB carbon

	Ref	CCI Biomass Climate Assessment Report v3		
	Issue	Page	Date	
	3.0	66	14.07.2021	

deficit over the African continent over edge areas is 4.06 Pg C ($16.1_{-5.9}^{+8.0}$ Mg C ha⁻¹, median and interquartile) (Table 7-1), partitioned into 3.4 Pg C in dry forests and 0.66 Pg C in moist ones.

Table 7-1: Carbon deficit from edge effects, fire-increased carbon deficit and area with edge effects. Note that carbon deficit from edge effects includes fire-increased carbon deficit. The weighted median of density of carbon deficit and density of fire-increased carbon deficit are shown in the table.

	Moist forest	Dry forest	Total
Carbon deficit (Pg C)	0.66	3.4	4.06
Density of carbon deficit (Mg C ha ⁻¹)	19.1	15.4	16.1
Fire-increased carbon deficit (Pg C)	0.077	0.82	0.90
Density of fire-increased carbon deficit (Mg C ha ⁻¹)	3.8	6.4	5.5
Area with edge effects (ha)	3.3×10 ⁷	1.8×10 ⁸	2.1×10 ⁸

7.2. Fire impacts on edge effects

Next, we considered forest edges with at least one fire event during 2004-2009. The scales of those fire related edges are higher in most grid cells (Fig. 7-2). The patterns of fire impact on the magnitude parameter are similar to those observed for the scale of edges. Fires increase the magnitudes by 14_{-8}^{+16} % and 10_{-5}^{+8} % in 70% and 61% of the grid cells in moist and dry forests. Fires edges have a higher carbon deficit by 0.90 Pg C ($5.5_{-2.9}^{+4.3}$ Mg C ha⁻¹), accounting for 22% of the total carbon deficit (Table 1). Most of the fire-related increased carbon deficit is in dry forests (0.82 Pg C, $6.4_{-2.9}^{+4.4}$ Mg C ha⁻¹) rather than in moist forests (0.077 Pg C, $3.8_{-1.7}^{+3.2}$ Mg C ha⁻¹) (Table 1). Two mechanisms relating to fire impact on edge effects were identified: direct fire intrusion into forests and indirect changes in local atmospheric circulation and canopy dryness. The first mechanism was studied through the distance that fires burn into a forest (fire distance) and the second through the difference in Bowen Ratio (β) between fire and non-fire edges ($\Delta\beta$), where β is the ratio between sensible and latent heat fluxes. The value of β for different pixel types follows the order: moist forest < dry forest < non-fire edge < fire edge (Fig 7-2)

In the published study (Zhao et al. 2021) these results were used to make future projections of edge carbon losses using a downscaling of forecasts of African deforestation areas in 2100 obtained from two Representative Concentration Pathways (gross forest loss area = 1.2×10⁷ ha and 9.7×10⁷ ha in RCP2.6 and RCP8.5). Future work could include the use of high-resolution fire datasets from Sentinel-2 (Ramo et al. 2021) that include small fires and show a 80% larger burned area in the African continent, and more recent CCI maps.

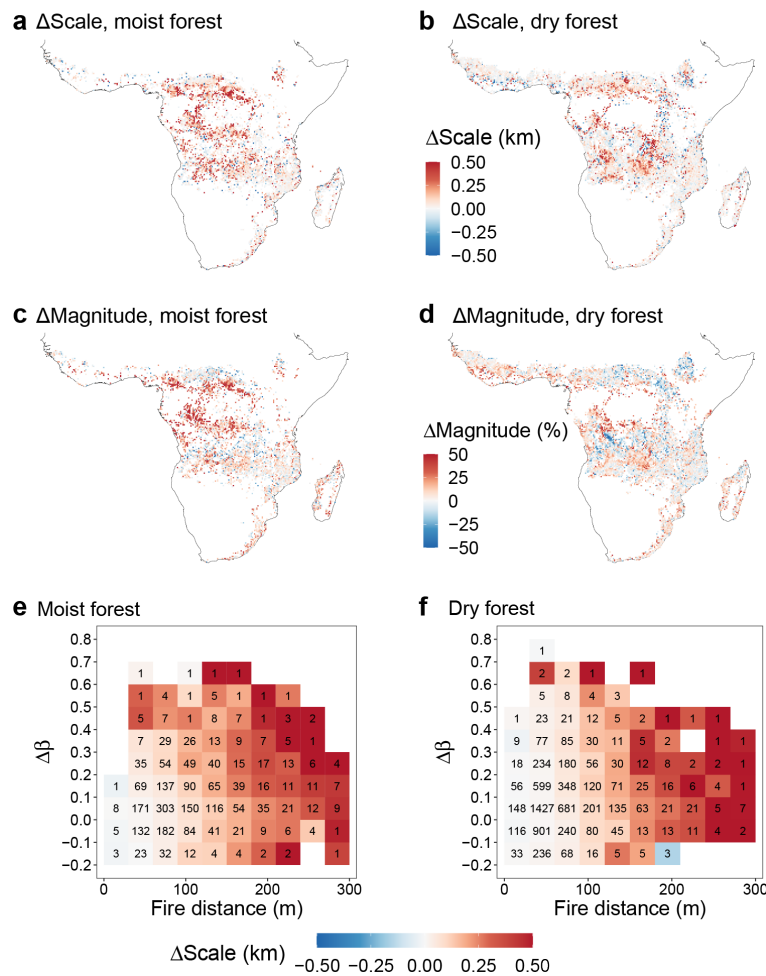




Figure 7-2: Difference of forest edge effects at fire and non-fire edges (Δ scale, fire minus non-fire, a-b; Δ magnitude, c-d) for moist and dry forests and Δ Scale change with $\Delta\beta$ (enhanced Bowen ratio) and fire distance (e-f). The scale and magnitude parameters that characterize the biomass deficit at forest edges are fitted from high resolution CCI Globbiomass data. The differences in edge effects (Δ scale and Δ magnitude) are regarded as the fire impacts on edge effects. Numbers in (e-f) are the total number of 0.25° grid cells located in each $\Delta\beta$ and fire distance interval. Only grid cells with successfully fitted curves at both fire and non-fire edges and with available β at both fire and non-fire edges are shown.

8. Preliminary global estimates of AGB changes combining SMOS passive microwave data and CCI Biomass high resolution maps

Over the past decades, the terrestrial biosphere globally removed about 30% of the anthropogenic CO₂ emissions due to fossil fuel burning and land use change. This net terrestrial carbon sink is the sum of carbon gains from vegetation growth and regrowth after human and environmental disturbances, and carbon losses from disturbance and environmental effects like drought. Monitoring the terrestrial carbon sink changes over time is essential to understand, accurately quantify and predict the effects of present and future climate change. Decadal changes of carbon stocks from inventories mainly give changes in forest ecosystems without information on spatial distribution. Only managed

	Ref	CCI Biomass Climate Assessment Report v3		
	Issue	Page	Date	
	3.0	68	14.07.2021	



forests are considered by countries' reports to the UNFCCC (e.g., Tubiello et al., 2021). Most countries do not have a National Forest Inventory to estimate forest carbon stock changes from repeated plot surveys and use a gain-loss approach based on areas disturbed by harvest or fires, and loss factors and typical static recovery curves that do not include the indirect impact of environmental factors affecting forest growth. Process-based models have also been used to assess the spatial distribution of the land sink, but show diverging estimates and poorly represent disturbances and land use change processes, lacking for instance a representation of forest degradation. Harris et al. (2021) recently created a map of above-ground biomass (AGB) change in the period 2001-2019 using a gain-loss inventory approach from different data sources including C removal from fire and harvest and carbon gains from recovery curves and remote sensing data for gains in intact forests. They found that tropical, temperate and boreal forests were carbon sinks over the years 2001-2019. However, this approach is unable to estimate temporal variations, and has large uncertainty. Xu et al. (2021) built a machine learning model spatially mapping AGB from ground plots using airborne lidar and satellite data, and used it to predict AGB variations spatially and temporally. Their findings suggested that total living biomass (including above- and below-ground biomass) increased by 8 PgC during 2000 – 2019, mainly due to the net gain of carbon in tropical and subtropical dry forests. However, this space-time substitution approach, predicting long-term temporal changes using spatial sensitivities of AGB to environmental factors and disturbances, ignored the local constraints on carbon stocks dynamics (e.g., forest demographic process, the legacy effects of environmental conditions).

The L-band vegetation optical depth (L-VOD) product from ESA's passive microwave Soil Moisture and Ocean Salinity (SMOS) satellite has been used to monitor vegetation carbon change (Fan et al., 2019; Wigneron et al., 2020; Qin et al., 2021). However, the L-VOD products are strongly perturbed by Radio Frequency Interference (RFI), especially in areas of the Northern Hemisphere (Oliva et al., 2016). Previous filtering methods for L-VOD have limited capability in RFI-affected regions, and we developed here a stricter filtering method that selects the "best" quality data. We also note that the L-VOD product is simultaneously sensitive to biomass and water stress (Konings et al., 2019). Separating the signals of carbon mass and water content from VOD is, therefore, necessary to better monitor carbon stock changes.

We designed a new filter to remove RFI effects from the raw daily L-VOD data from ascending and descending orbits. Then we fitted and reconstructed the changes in the shape of the seasonal cycle and long-term trends of L-VOD using curve fitting methods, which was used by NOAA to process the atmospheric carbon dioxide measurements. After removing the seasonality changes of L-VOD (mainly associated with the water content variations), we calculated the mean annual value of L-VOD during the less water stressed periods of May to Aug for all northern hemisphere regions. We then mapped annual aboveground biomass (AGB) changes globally, using L-VOD and an empirical spatial calibration relationship with the AGB map for the year 2010 from the CCI Biomass project. Specific relationships were built for the tropics (25°N to 25°S) and the Northern Hemisphere (above 25°N). We then made a first attempt to quantify the spatial-temporal annual dynamics of AGB in relation to forest cover changes from 2010 to 2019, and compared results to the ensemble of 15 dynamic global vegetation models (DGVMs) from the TRENDY project.

8.1. Regional aboveground biomass (AGB) changes

Between 2010 and 2019, AGB stocks increased by + 4.07 PgC (from 255 to 259 PgC) globally, but with larger relative variations at regional scales as shown in Fig. 8-1. Pixels with significant net carbon losses were distributed in the northern and eastern Amazon, Congo basin, eastern Australia, and Siberia, across all climatic biomes. The total AGB loss in boreal (-2.44 PgC) and dry tropics (-1.9 PgC) was higher

	Ref	CCI Biomass Climate Assessment Report v3		
	Issue	Page	Date	
	3.0	69	14.07.2021	

than those in the wet tropics (-1.47 PgC), temperate (-1.34 PgC) and arid (-0.80 PgC) regions (Fig. 8-1). The spatial distribution of AGB loss is consistent with areas of observed forest loss during 2010-2019 from Hansen et al. (2013). However, not all forest loss regions showed significant net carbon losses, e.g., British Columbia, European Russia, Cambodia, Malaysia and Indonesia (in Southeast Asia). In these regions, carbon accumulation from undisturbed forest gains and post-disturbance recovery appear to have offset carbon losses from forest area loss. In addition, pixels in western Central Africa and southern China show large net carbon gains without significant forest gains. The total carbon gains in the boreal and temperate regions are +4.21 PgC and +3.41 PgC, followed by the dry tropics (1.92 PgC), arid regions (1.26 PgC), and wet tropical region (0.90 PgC).

Boreal and temperate regions experienced a net carbon gain of +1.76 PgC and +2.01 PgC from 2010 to 2019, accounting for the largest and the second largest fraction (47% and 55%) of the global carbon sink from AGB changes. Both TRENDY model ensemble and three inversion models consistently show a carbon sink in the boreal and temperate regions, although the spread in the magnitude of this sink among different models is large. Note that atmospheric inversions include belowground biomass changes, soil organic carbon changes and CO₂ lateral exports, which are not in our AGB carbon stock change estimates. For the arid region and dry tropics, AGB changes were a small net gain or approximately neutral (+0.4 PgC and +0.001 PgC), while TRENDY models differ in the direction of AGB carbon change, showing on average a small mean carbon source in arid regions and in dry tropics. In the wet tropics, we found a net carbon loss of -0.15 PgC from 2010 to 2019, while the simulated AGB changes from TRENDY models indicate a carbon sink. One explanation for this discrepancy could be the incomplete or missing representation in TRENDY models of disturbances in particular from degradation, and anthropogenic disturbances in the wet tropics.

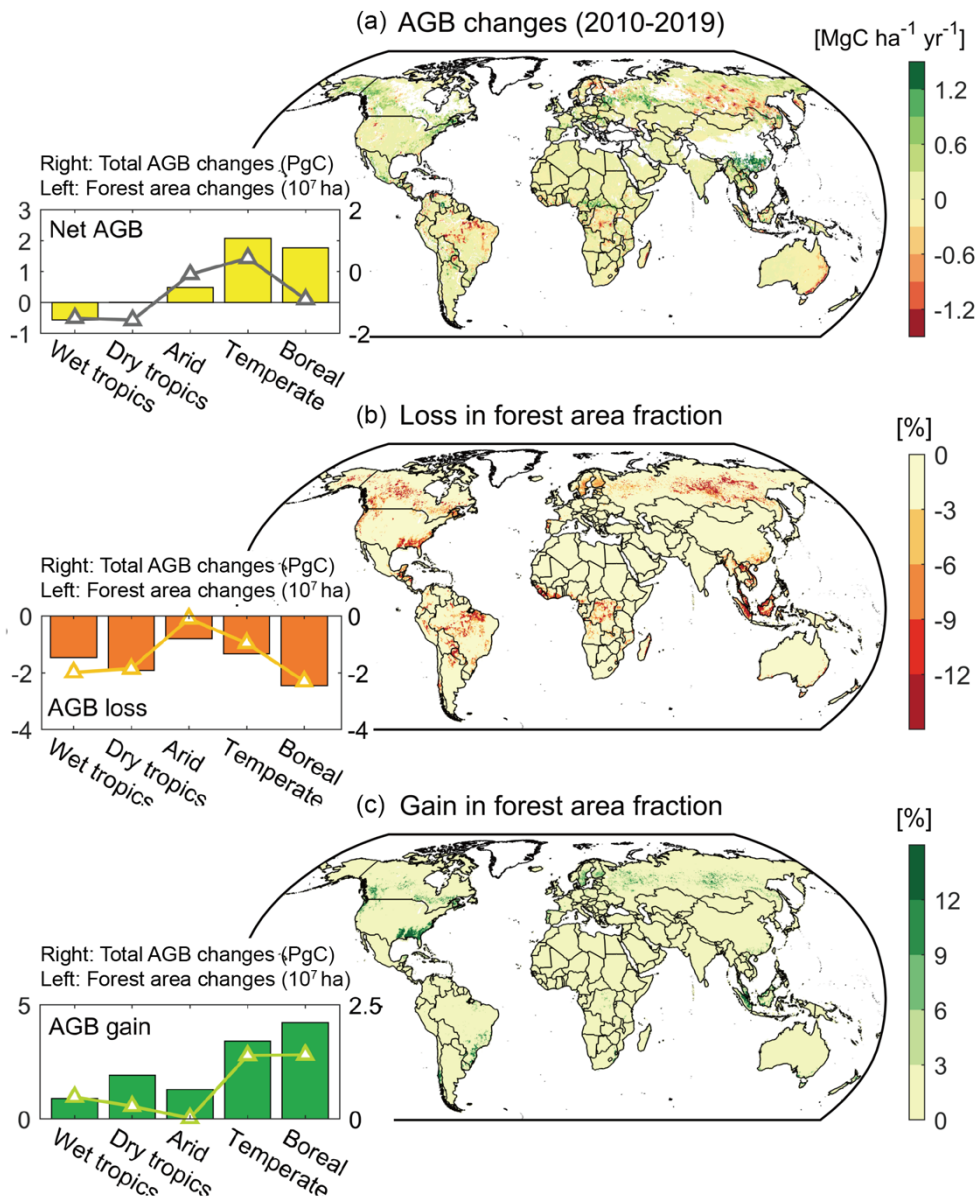


Figure 8-1: (a) Spatial distribution of mean annual changes in aboveground biomass (AGB) carbon between 2010 to 2019. The inset shows the total net AGB changes (yellow bars) and forest area changes (black curve) for five climatic biomes. (b) Spatial distribution of the areal fraction of forest loss (2010 – 2019). The inset shows the total changes in AGB (orange bars) and forest area (orange curve) for regions with AGB loss. (c) Spatial distribution of the areal fraction of forest gains (2010 – 2019). The inset shows the total changes in AGB (green bars) and forest area (green curve) for regions with AGB gain.

8.2. AGB changes attributed to disturbances

To quantify the contributions of anthropogenic disturbances to AGB changes, we used the global classification map of the drivers of forest loss (Curtis et al., 2018) and aggregated this forest disturbance classification map with a spatial resolution of 10 x 10 km to the areal fractions of each disturbance type at 25 x 25 km, and then estimated the total AGB changes due to five disturbance

drivers (i.e., deforestation, agriculture, forestry, wildfire and urbanization) (Fig. 8-2). In the Tropics (wet and dry), deforestation was the most important contributor to forest and AGB losses, with a total loss of -0.33 PgC in the wet tropics and -0.42 PgC in the dry tropics. Important contributions were also from agriculture (small- to medium-scale forest/shrub to agriculture) which led to a decrease in AGB of -0.23 PgC in the wet tropics and of -0.14 PgC in the dry tropics. The negative effects of deforestation and agriculture on AGB in the dry tropics do not appear to be offset by the positive effects of forestry and vegetation growth. In contrast, TRENDY models forced by the land-use and land-cover change map from the LUH2v2h reconstruction show no significant forest fraction decrease in the wet tropics, so models do not reproduce the AGB loss in this region. In the Temperate and Boreal regions, forestry (defined as large-scale forestry operations in managed forests and tree plantations) has been a substantial driver of the carbon sink (increase in total AGB of +1.53 PgC and +1.02 PgC in Temperate and Boreal forests respectively). Several recent satellite data provide evidence that forest planting and management in southern China and rubber plantations in mountainous Southeast Asia (e.g., Cambodia, Indonesia, etc.) led to greening and extensive carbon sequestration during the last decade. TRENDY models largely underestimated the effects of plantations on AGB in the above-mentioned regions. Lastly, wildfires (defined as forest burning with no visible human conversion or agricultural activity) contributed to a net AGB loss of -0.25 PgC in the boreal region.

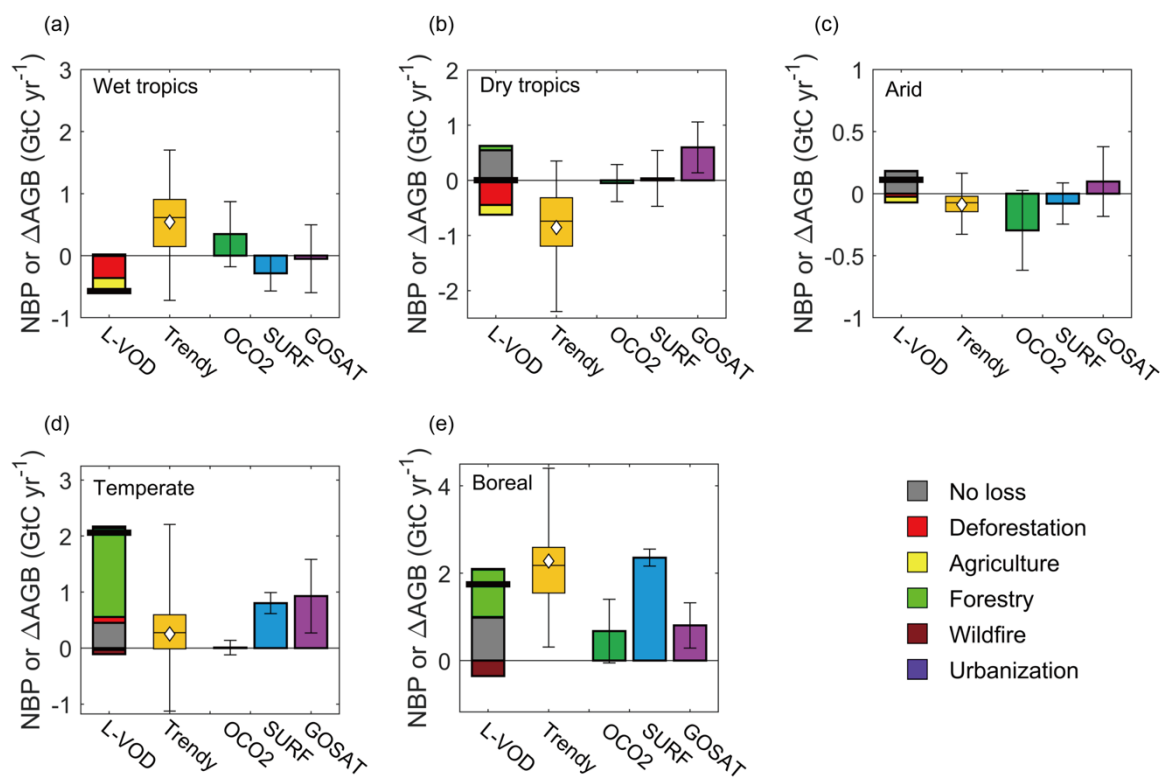




Figure 8-2: Aboveground biomass annual changes (ΔAGB) from L-VOD (thick black line) and Trendy DGVMs, and mean net biome productivity (NBP) from inversion models (OCO2, SURF, and GOSAT) from 2010 to 2019 for five climatic biomes: wet tropics (a), dry tropics (b), arid (c), temperate (d), and boreal (e). The stacked bars of L-VOD show the subcomponents of ΔAGB that are caused by no forest loss (grey), deforestation (red), agriculture (yellow), forestry (green), wildfire (brown) and urbanization (dark blue).

	Ref	CCI Biomass Climate Assessment Report v3		
	Issue	Page	Date	
	3.0	72	14.07.2021	

8.3. AGB changes in relation to forest age

In regions with a forest loss fraction of less than 5%, a possible reason for the discrepancy between satellite data and DGVMs is that current DGVMs predicted the carbon sink without considering the different capacities to sequester carbon for young, mature, and old-growth forests. To confirm this, we utilized a global database of forest age (Besnard et al., 2021 in review) to calculate the total net AGB changes in each forest age bin. We found that very young forests (aged 0 – 10 years) and old-growth forests (aged > 150 years) were approximately neutral, while middle-aged forests (aged 10 – 50 years) contributed the largest fraction of the carbon sink. The total carbon sink decreases with age (from 50 to 150 years). In contrast, TRENDY models showed different (even opposite) curves of total AGB changes with forest age. Models predicted that the old-growth forests were the largest carbon sink and young forests (aged 10 – 40 years) were a carbon source, and models overestimated the carbon sink of old-growth forests growing in the Tropics. This is probably because modelled AGB changes from the TRENDY ensemble mainly depend on the response of productivity and mortality to environmental drivers (CO₂, climate, nitrogen deposition and neglect demographic processes). A previous modelling study found that after incorporating forest age into LPJ-GUESS model, the carbon sink from regrowing forests (young forests typically younger than 40 years) is greater than that of old-growth forests (Pugh et al., 2019). Forest age is correlated with height, so we also used canopy height data from spaceborne lidar measurements (Simard et al., 2011) to assess the robustness of the AGB changes response to forest age, and found a similar response curve of AGB changes to canopy height than the response curve of AGB to forest age.

8.4. Interannual variability of AGB changes

Since the interannual variations in the net land–atmosphere carbon exchange come mainly from the AGB carbon pool, we compared the interannual differences in global AGB stocks (Δ AGB) with the global atmospheric CO₂ growth rate. The CO₂ growth rate lagged behind the curve of global Δ AGB because dead trees decay slowly (Palace et al. 2012), and AGB losses (due to mortality events) do not cause an instantaneous CO₂ emission to the atmosphere, rather a lagged CO₂ emission from decaying coarse woody debris (CWD), litter and soil pools. This lagged CWD decay should be considered, at least in the wet Tropics. We estimated CWD decomposition rates using inventory data and calculated the delayed net CO₂ losses of CWD with a first-order kinetics model and satellite net primary productivity (NPP) from the Moderate Resolution Imaging Spectroradiometer (MODIS). Considering the decay rate of CWD fed by AGB losses, we found that the interannual variability in the gross carbon loss flux, which was reduced due to part of the carbon remaining in CWD, agreed better with the interannual variability of the growth rate, especially the carbon loss flux variations after the big mortality events in 2012 and 2015 (Fig 8-3). This work is in progress and will be submitted in summer 2021 as a project publication (Yang et al.).

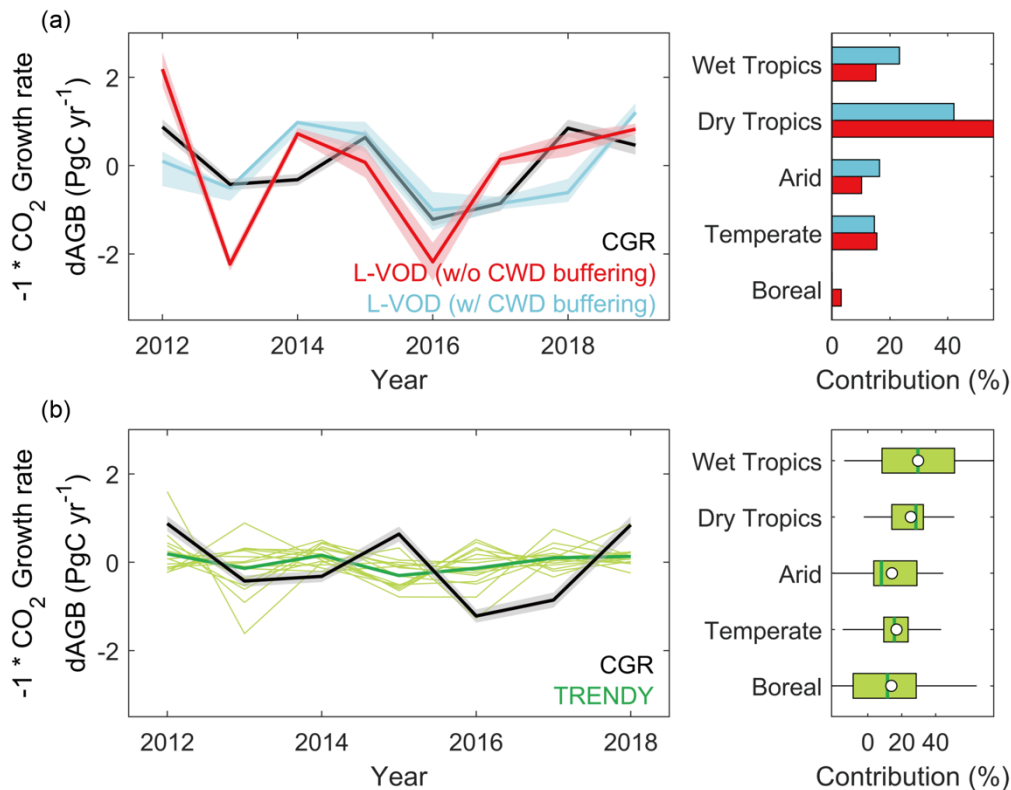






Figure 8-3: (a) Global atmospheric carbon growth rate (CGR, with reversed sign, black line), global AGB fluxes from L-VOD without coarse woody debris (CWD) buffering (red line), AGB fluxes from L-VOD with CWD buffering (blue line), over 2012 – 2019. The right-hand panel shows the contribution (%) of five climate biomes to the interannual variability in global AGB fluxes from L-VOD without and with CWD buffering. Red is the original AGB change from one year to the next from LVOD. Blue is the change of AGB carbon flux exchanged with the atmosphere after correcting for the residence time of dead carbon in CWD. The global AGB fluxes were calculated using annual AGB changes compared to the previous year. The shadings of each curve show the uncertainty of CGR and the standard deviation of L-VOD AGB estimated by different calibrations. (b) Reversed sign global atmospheric carbon growth rate (CGR, black line) and global AGB fluxes from Trendy DGVMs (green lines) over 2012 – 2018. The right-hand panel shows the contribution (%) of five biomes to the interannual variability in global AGB fluxes from individual TRENDY models.

9. References

- Ahlström, A., Canadell, J. G., Schurgers, G., et al. (2017). Hydrologic resilience and Amazon productivity. *Nat. Commun.*, 8(1), 387.
- Alamgir, M., Campbell, M. J., Sloan, S., et al. (2017). Economic, socio-political and environmental risks of road development in the tropics. *Curr. Biol.*, 27(20), R1130-R1140.
- Albani, M., Medvigy, D., Hurtt, G. C., Moorcroft, P. R. (2006). The contributions of land-use change, CO₂ fertilization, and climate variability to the Eastern US carbon sink. *Global Change Biol.*, 12(12), 2370-2390.
- Allen, C. D., Macalady, A. K., Chenchouni, H., et al. (2010). A global overview of drought and heat-induced tree mortality reveals emerging climate change risks for forests. *For. Ecol. Manage.*, 259(4), 660-684.

	Ref	CCI Biomass Climate Assessment Report v3		
	Issue	Page	Date	
	3.0	74	14.07.2021	

- Anav, A., Friedlingstein, P., Kidston, M., et al. (2013). Evaluating the land and ocean components of the global carbon cycle in the CMIP5 Earth System Models. *J. Clim.*, 26(18), 6801-6843.
- Anderegg, W. R. L., Anderegg, L. D. L., Huang, C. Y. (2019). Testing early warning metrics for drought-induced tree physiological stress and mortality. *Global Change Biol.*, 25(7), 2459.
- Aragão, L. E. O., Malhi, Y., Roman-Cuesta, R. M., Saatchi, S., Anderson, L. O. & Shimabukuro, Y. E. Spatial patterns and fire response of recent Amazonian droughts. *Geophys. Res. Lett.* 34, L07701 (2007).
- Arellano, G., Medina, N. G., Tan, S., Mohamad, M. & Davies, S. J. Crown damage and the mortality of tropical trees. *New Phytol.* 221, 169-179 (2019).
- Asner, G. P., Knapp, D. E., Broadbent, E. N., et al. (2005). Selective logging in the Brazilian Amazon. *Science*, 310(5747), 480-482.
- Avitabile, V., Herold, M., Heuvelink, G. B., et al. (2016). An integrated pan-tropical biomass map using multiple reference datasets. *Global Change Biol.*, 22(4), 1406-1420.
- Baccini, A. G. S. J., Goetz, S. J., Walker, W. S., et al. (2012). Estimated carbon dioxide emissions from tropical deforestation improved by carbon-density maps. *Nat. Clim. Change*, 2(3), 182.
- Baccini, A., Walker, W., Carvalho, L., Farina, M., Sulla-Menashe, D., & Houghton, R. A. (2017). Tropical forests are a net carbon source based on aboveground measurements of gain and loss. *Science*, 358(6360), 230-234.
- Becknell, J. M., Kucek, L. K., Powers, J. S. (2012). Aboveground biomass in mature and secondary seasonally dry tropical forests: A literature review and global synthesis. *For. Ecol. Manage.*, 276, 88-95.
- Beer, C., Reichstein, M., Tomelleri, E., et al. (2010). Terrestrial gross carbon dioxide uptake: global distribution and covariation with climate. *Science*, 329(5993), 834-838.
- Bennett, A. C., McDowell, N. G., Allen, C. D. & Anderson-Teixeira, K. J. Larger trees suffer most during drought in forests worldwide. *Nat. Plants* 1, 15139 (2015).
- Bertram, J., Dewar, R. C. (2013). Statistical patterns in tropical tree cover explained by the different water demand of individual trees and grasses. *Ecology*, 94(10), 2138-2144.
- Bloom AA, Exbrayat JF, van der Velde IR et al. (2016) The decadal state of the terrestrial carbon cycle: Global retrievals of terrestrial carbon allocation, pools, and residence times. *Proc Natl Acad Sci USA*, 113(5), 1285-1290.
- Bolin, B., Rodhe, H. (1973). A note on the concepts of age distribution and transit time in natural reservoirs. *Tellus*, 25(1), 58-62.
- Bontemps, S., Defourny, P., Radoux, J., et al. (2013). Consistent global land cover maps for climate modelling communities: current achievements of the ESA's land cover CCI. In *Proceedings of the ESA Living Planet Symposium, Edimburgh* (pp. 9-13).
- Bouget, C., Duelli, P. (2004). The effects of windthrow on forest insect communities: a literature review. *Biol. Conserv.*, 118(3), 281-299.
- Bouvet, A., Mermoz, S., Le Toan, T., Villard, L., Mathieu, R., Naidoo, L. & Asner, G. P. An above-ground biomass map of African savannahs and woodlands at 25 m resolution derived from ALOS PALSAR. *Remote Sens. Environ.* 206, 156-173 (2018).
- Bowman, D. M., Balch, J. K., Artaxo, P., et al. (2009). Fire in the Earth system. *Science*, 324(5926), 481-484.

	Ref	CCI Biomass Climate Assessment Report v3		
	Issue	Page	Date	
	3.0	75	14.07.2021	

Brando, P. M., Nepstad, D. C., Balch, J. K., Bolker, B., Christman, M. C., Coe, M., Putz, F. E. (2012). Fire-induced tree mortality in a neotropical forest: the roles of bark traits, tree size, wood density and fire behavior. *Global Change Biol.*, 18(2), 630-641.

Brando, P. M. et al. Abrupt increases in Amazonian tree mortality due to drought-fire interactions. *Proc. Natl. Acad. Sci. U.S.A.* 111, 6347-6352 (2014).

Brandt, M., Rasmussen, K., Hiernaux, P., et al. (2018). Reduction of tree cover in West African woodlands and promotion in semi-arid farmlands. *Nat. Geosci.*, 11(5), 328.

Breiman, L. Random forests. *Machine learning* 45, 5-32 (2001).

Brienen RJW, Phillips OL, Feldpausch TR et al. (2015) Long-term decline of the Amazon carbon sink. *Nature*, 519(7543), 344-348.

Brinck, K., Fischer, R., Groeneveld, J., et al. (2017). High resolution analysis of tropical forest fragmentation and its impact on the global carbon cycle. *Nat. Commun.*, 8, 14855.

Brodribb, T. J., Powers, J., Cochard, H. & Choat, B. Hanging by a thread? Forests and drought. *Science* 368, 261-266 (2020).

Burton, C., Rifai, S. & Malhi, Y. Inter-comparison and assessment of gridded climate products over tropical forests during the 2015/2016 El Niño. *Philos. Trans. R. Soc. London, Ser. B* 373, 20170406 (2018).

Butler, E. E., Datta, A., Flores-Moreno, H., et al. (2017). Mapping local and global variability in plant trait distributions. *Proc. Natl. Acad. Sci. U.S.A.*, 114(51), E10937-E10946.

Büntgen U, Krusic PJ, Piermattei A et al. (2019) Limited capacity of tree growth to mitigate the global greenhouse effect under predicted warming. *Nat Commun*, 10(1), 2171.

Campioli, M., Vicca, S., Luyssaert, S., et al. (2015). Biomass production efficiency controlled by management in temperate and boreal ecosystems. *Nat. Geosci.*, 8(11), 843-846.

Cantú, A. G., Frieler, K., Reyer, C. P., et al. (2018). Evaluating changes of biomass in global vegetation models: the role of turnover fluctuations and ENSO events. *Environ. Res. Lett.*, 13(7), 075002.

Carvalhais, N., Reichstein, M., Ciais, P., et al. (2010). Identification of vegetation and soil carbon pools out of equilibrium in a process model via eddy covariance and biometric constraints. *Global Change Biol.*, 16(10), 2813-2829.

Carvalhais, N., Forkel, M., Khomik, M., et al. (2014). Global covariation of carbon turnover times with climate in terrestrial ecosystems. *Nature*, 514(7521), 213.



Caspersen, J. P., Pacala, S. W., Jenkins, J. C., Hurtt, G. C., Moorcroft, P. R., Birdsey, R. A. (2000). Contributions of land-use history to carbon accumulation in US forests. *Science*, 290(5494), 1148-1151.

Clark, D. B., Mercado, L. M., Sitch, S., et al. (2011). The Joint UK Land Environment Simulator (JULES), model description-Part 2: carbon fluxes and vegetation dynamics. *Geosci. Model Dev.*, 4(3), 701-722.

Chang, J., Ciais, P., Wang, X., et al. (2017). Benchmarking carbon fluxes of the ISIMIP2a biome models. *Environ. Res. Lett.*, 12(4), 045002.

Channan, S., Collins, K., Emanuel, W. R. (2014). Global mosaics of the standard MODIS land cover type data. University of Maryland and the Pacific Northwest National Laboratory, College Park, Maryland, USA, 30.

Chapin, F. S., Woodwell, G. M., Randerson, J. T., et al. (2006). Reconciling carbon-cycle concepts, terminology, and methods. *Ecosystems*, 9(7), 1041-1050.

	Ref	CCI Biomass Climate Assessment Report v3		
	Issue	Page	Date	
	3.0	76	14.07.2021	

Chaplin-Kramer, R., Ramler, I., Sharp, R., et al. (2015). Degradation in carbon stocks near tropical forest edges. *Nat. Commun.*, 6, 10158.

Chave J, Navarrete D, Almeida S et al. (2010) Regional and seasonal patterns of litterfall in tropical South America, *Biogeosci*, 7(1), 43-55.

Chen G, Yang Y, Robinson D. (2013) Allocation of gross primary production in forest ecosystems: allometric constraints and environmental responses. *New Phytol*, 200(4), 1176-1186.

Chen, X. et al. Novel representation of leaf phenology improves simulation of Amazonian evergreen forest photosynthesis in a land surface model. *J. Adv. Model. Earth Syst.* 12, e2018MS001565 (2020).

Chuvieco, E., Yue, C., Heil, A., et al. (2016). A new global burned area product for climate assessment of fire impacts. *Global Ecol. Biogeogr.*, 25(5), 619-629.

Coley PD, Barone JA. (1996) Herbivory and plant defenses in tropical forests. *Annu Rev Ecol Evol Syst*, 27(1), 305-335.

Condit, R., Hubbell, S. P. & Foster, R. B. Assessing the response of plant functional types to climatic change in tropical forests. *J. Veg. Sci.* 7, 405-416 (1996).

da Costa, A. C. L. et al. Effect of 7-yr of experimental drought on vegetation dynamics and biomass storage of an eastern Amazonian rainforest. *New Phytol.* 187, 579-591 (2010).

Cox, P. M., Betts, R. A., Jones, C. D., Spall, S. A., Totterdell, I. J. (2000). Acceleration of global warming due to carbon-cycle feedbacks in a coupled climate model. *Nature*, 408(6809), 184.

Das, A. J., Stephenson, N. L., Davis, K. P. (2016). Why do trees die? Characterizing the drivers of background tree mortality. *Ecology*, 97(10), 2616-2627.

De Kauwe MG, Medlyn BE, Zaehle S et al. (2014) Where does the carbon go? A model-data intercomparison of vegetation carbon allocation and turnover processes at two temperate forest free-air CO₂ enrichment sites. *New Phytol*, 203(3), 883-899.

Delbart, N., Ciais, P., Chave, J., Viovy, N., Malhi, Y., Le Toan, T. (2010). Mortality as a key driver of the spatial distribution of aboveground biomass in Amazonian forest: results from a dynamic vegetation model. *Biogeosci.*, 7, 3027-3039.

Domingues TF, Berry JA, Martinelli LA et al. (2005) Parameterization of canopy structure and leaf-level gas exchange for an eastern Amazonian tropical rain forest (Tapajos National Forest, Para, Brazil). *Earth Interact*, 9(17), 1-23.

Dong, J., Kaufmann, R. K., Myneni, R. B., et al. (2003). Remote sensing estimates of boreal and temperate forest woody biomass: carbon pools, sources, and sinks. *Remote Sens. Environ.*, 84(3), 393-410.



Doughty CE, Metcalfe DB, Girardin CAJ et al. (2015) Drought impact on forest carbon dynamics and fluxes in Amazonia. *Nature*, 519(7541), 78-82.

Ellis, E. C., Antill, E. C., Kreft, H. (2012). All is not loss: plant biodiversity in the Anthropocene. *PloS one*, 7(1), e30535.

Erb, K. H., Fetzel, T., Plutzer, C., et al. (2016). Biomass turnover time in terrestrial ecosystems halved by land use. *Nat. Geosci.*, 9, 674-678.

Erb, K. H., Kastner, T., Plutzer, C., et al. (2018). Unexpectedly large impact of forest management and grazing on global vegetation biomass. *Nature*, 553(7686), 73-76.

Espírito-Santo, F. D. B., Keller, M., Braswell, B., Nelson, B. W., Frohling, S., Vicente, G. (2010). Storm intensity and old-growth forest disturbances in the Amazon region. *Geophys. Res. Lett.*, 37, L11403.

	Ref	CCI Biomass Climate Assessment Report v3		
	Issue	Page	Date	
	3.0	77	14.07.2021	

Espirito-Santo, F. D., Gloor, M., Keller, M., Malhi, Y., et al. (2014). Size and frequency of natural forest disturbances and the Amazon forest carbon balance. *Nat. Commun.*, 5(3434), 1.

Fahey, R. T., Fotis, A. T. & Woods, K. D. Quantifying canopy complexity and effects on productivity and resilience in late-successional hemlock–hardwood forests. *Ecol. Appl.* 25, 834-847 (2015).

Fan, L., Wigneron, J. P., Ciais, P., et al. (2019). Satellite-observed pantropical carbon dynamics. *Nat. Plants*, 1.

Farrior, C. E., Tilman, D., Dybzinski, R., et al. (2013). Resource limitation in a competitive context determines complex plant responses to experimental resource additions. *Ecology*, 94(11), 2505-2517.

Farrior, C. E., Bohlman, S. A., Hubbell, S., Pacala, S. W. (2016). Dominance of the suppressed: Power-law size structure in tropical forests. *Science*, 351(6269), 155-157.

Feldman, A. F., Gianotti, D. J. S., Konings, A. G., McColl, K. A., Akbar, R., Salvucci, G. D. & Entekhabi, D. Moisture pulse-reserve in the soil-plant continuum observed across biomes. *Nat. Plants* 4, 1026-1033 (2018).

Fensham, R. J., Fairfax, R. J., Ward, D. P. (2009). Drought-induced tree death in savanna. *Global Change Biol.*, 15(2), 380-387.

Fensham, R. J., Butler, D. W. & Foley, J. How does clay constrain woody biomass in drylands? *Global Ecol. Biogeogr.* 24, 950-958 (2015).

Fernández-Martínez, M., Vicca, S., Janssens, et al. (2014). Nutrient availability as the key regulator of global forest carbon balance. *Nat. Clim. Change*, 4, 471-476.

Fernandez-Moran, R., Al-Yaari, A., Mialon, A., et al. (2017). SMOS-IC: An alternative SMOS soil moisture and vegetation optical depth product. *Remote Sens.*, 9(5), 457.

Franklin O, Johansson J, Dewar RC et al. (2012) Modeling carbon allocation in trees: a search for principles. *Tree Physiol*, 32(6), 648-666.

Frieler, K., Lange, S., Piontek, F., et al. (2017). Assessing the impacts of 1.5° C global warming-Simulation protocol of the Inter-Sectoral Impact Model Intercomparison Project (ISIMIP2b). *Geosci. Model Dev.*, 10(12), 4321-4345.

Friend, A. D., Lucht, W., Rademacher, T. T., et al. (2014). Carbon residence time dominates uncertainty in terrestrial vegetation responses to future climate and atmospheric CO₂. *Proc. Natl. Acad. Sci. U.S.A.*, 111(9), 3280-3285.

Galbraith, D., Malhi, Y., Affum-Baffoe, K., et al. (2013). Residence times of woody biomass in tropical forests. *Plant Ecol. Divers.*, 6(1), 139-157.



Gessler, A., Schaub, M. & McDowell, N. G. The role of nutrients in drought-induced tree mortality and recovery. *New Phytol.* 214, 513-520 (2017).

Goll, D. S., Brovkin, V., Parida, B. R., et al. (2012). Nutrient limitation reduces land carbon uptake in simulations with a model of combined carbon, nitrogen and phosphorus cycling. *Biogeosci.*, 9, 3547-3569.

Goll, D. S., Brovkin, V., Liski, J., et al. (2015). Strong dependence of CO₂ emissions from anthropogenic land cover change on initial land cover and soil carbon parametrization. *Global Biogeochem. Cycles*, 29(9), 1511-1523.

Green, J. et al. Amazon rainforest photosynthesis increases in response to atmospheric dryness. in review.

Guan, K. et al. Photosynthetic seasonality of global tropical forests constrained by hydroclimate. *Nat. Geosci.* 8, 284-289 (2015).

	Ref	CCI Biomass Climate Assessment Report v3		
	Issue	Page	Date	
	3.0	78	14.07.2021	

Guimberteau, M., Zhu, D., Maignan, F., et al. (2018). ORCHIDEE-MICT (v8.4.1), a land surface model for the high latitudes: model description and validation. *Geosci. Model Dev.*, 11(1), 121.

Haberl, H., Erb, K. H., Krausmann, F., et al. (2007). Quantifying and mapping the human appropriation of net primary production in earth's terrestrial ecosystems. *Proc. Natl. Acad. Sci. U.S.A.*, 104(31), 12942-12947.

Hansen, M. C., Potapov, P. V., Moore, R., et al. (2013). High-resolution global maps of 21st-century forest cover change. *Science*, 342(6160), 850-853.

Harding, D. J. & Carabajal, C. C. ICESat waveform measurements of within-footprint topographic relief and vegetation vertical structure. *Geophys. Res. Lett.* 32, L21S10 (2005).

Haverd, V., Smith, B., Nieradzki, L., et al. (2018). A new version of the CABLE land surface model (Subversion revision r4601) incorporating land use and land cover change, woody vegetation demography, and a novel optimisation-based approach to plant coordination of photosynthesis. *Geosci. Model Dev.*, 11(7), 2995-3026.

Heinimann, A., Mertz, O., Frohling, S., et al. (2017). A global view of shifting cultivation: Recent, current, and future extent. *PloS one*, 12(9), e0184479.

Herrero M, Havlík P, Valin H et al. (2013) Biomass use, production, feed efficiencies, and greenhouse gas emissions from global livestock systems. *Proc Natl Acad Sci U.S.A.*, 110(52), 20888-20893.

Hofhansl F, Schneckner J, Singer G et al. (2015) New insights into mechanisms driving carbon allocation in tropical forests. *New Phytol*, 205(1), 137-146.

Huang, M., Piao, S., Ciais, P., Peñuelas, J., Wang, X., Keenan, T. F., ... & Alkama, R. (2019). Air temperature optima of vegetation productivity across global biomes. *Nat. Ecol. Evol.*, 3(5), 772-779.

Humphrey, V., Gudmundsson, L. (2019). GRACE-REC: a reconstruction of climate-driven water storage changes over the last century. *Earth Syst. Sci. Data*, 11(3), 1153-1170.

Huntingford, C., Zelazowski, P., Galbraith, D., et al. (2013). Simulated resilience of tropical rainforests to CO₂-induced climate change. *Nat Geosci.*, 6(4), 268.

Huntzinger, D. N., Schwalm, C., Michalak, A. M., et al. (2013). The north american carbon program multi-scale synthesis and terrestrial model intercomparison project—part 1: Overview and experimental design. *Geosci. Model Dev.*, 6(6), 2121-2133.

Hurt, G. C., Chini, L. P., Frohling, S., et al. (2011). Harmonization of land-use scenarios for the period 1500–2100: 600 years of global gridded annual land-use transitions, wood harvest, and resulting secondary lands. *Clim. Change*, 109(1-2), 117.



Issartel, J., & Coiffard, C. (2011). Extreme longevity in trees: live slow, die old?. *Oecologia*, 165(1), 1-5.

Jiang C, Ryu Y. (2016) Multi-scale evaluation of global gross primary productivity and evapotranspiration products derived from Breathing Earth System Simulator (BESS). *Remote Sens Environ*, 186, 528-547.



Johnson, M. O., Galbraith, D., Gloor, M., et al. (2016). Variation in stem mortality rates determines patterns of above-ground biomass in Amazonian forests: implications for dynamic global vegetation models. *Global Change Biol.*, 22(12), 3996-4013.

Jung, M., Reichstein, M., Margolis, H. A., et al. (2011). Global patterns of land-atmosphere fluxes of carbon dioxide, latent heat, and sensible heat derived from eddy covariance, satellite, and meteorological observations. *J. Geophys. Res. Biogeosci.*, 116(G3).

Kaiser, J. W. et al. Biomass burning emissions estimated with a global fire assimilation system based on observed fire radiative power. *Biogeosci.* 9, 527-554 (2012).

	Ref	CCI Biomass Climate Assessment Report v3		
	Issue	Page	Date	
	3.0	79	14.07.2021	

- Keller, K., Lienert, S., Bozbiyik, A., et al. (2017). 20th century changes in carbon isotopes and water-use efficiency: tree-ring-based evaluation of the CLM4. 5 and LPX-Bern models. *Biogeosci.*, 14(10), 2641-2673.
- Koven, C. D., Chambers, J. Q., Georgiou, K., et al. (2015). Controls on terrestrial carbon feedbacks by productivity versus turnover in the CMIP5 Earth System Models. *Biogeosci.*, 12(17), 5211-5228.
- Konings, A. G., Gentine, P. (2017). Global variations in ecosystem-scale isohydricity. *Global Change Biol.*, 23(2), 891-905.
- Krinner, G., Viovy, N., de Noblet-Ducoudré, N., et al. (2005). A dynamic global vegetation model for studies of the coupled atmosphere-biosphere system. *Global Biogeochem. Cycles*, 19(1).
- Laurance, W. F., Fearnside, P. M., Laurance, S. G., et al. (1999). Relationship between soils and Amazon forest biomass: a landscape-scale study. *For. Ecol. Manage.*, 118(1-3), 127-138.
- Lehmann, C. E., Anderson, T. M., Sankaran, M., et al. (2014). Savanna vegetation-fire-climate relationships differ among continents. *Science*, 343(6170), 548-552.
- Li, W., Ciais, P., Peng, S., et al. (2017). Land-use and land-cover change carbon emissions between 1901 and 2012 constrained by biomass observations. *Biogeosci.*, 14(22), 5053-5067.
- Li, W., MacBean, N., Ciais, P., et al. (2018). Gross and net land cover changes in the main plant functional types derived from the annual ESA GLOBBIOMASS land cover maps (1992–2015). *Earth Syst. Sci. Data*, 10(1), 219-234.
- Liu, Y., Liu, R., Chen, J. M. (2012). Retrospective retrieval of long-term consistent global leaf area index (1981–2011) from combined AVHRR and MODIS data. *J. Geophys. Res. Biogeosci.*, 117(G4).
- Liu, Y. Y., Van Dijk, A. I., De Jeu, R. A., et al. (2015). Recent reversal in loss of global terrestrial biomass. *Nat. Clim. Change*, 5(5), 470-474.
- Liu, J. et al. Contrasting carbon cycle responses of the tropical continents to the 2015-2016 El Niño. *Science* 358, eaam5690 (2017).
- Luyssaert, S., Inglima, I., Jung, M., et al. (2007). CO2 balance of boreal, temperate, and tropical forests derived from a global database. *Global Change Biol.*, 13(12), 2509-2537.
- MacDicken, K. G. (2015). Global forest resources assessment 2015: what, why and how?. *For. Ecol. Manage.*, 352, 3-8.
- Maherali, H., Pockman, W. T., Jackson, R. B. (2004). Adaptive variation in the vulnerability of woody plants to xylem cavitation. *Ecology*, 85(8), 2184-2199.
- Malhi, Y., Aragão, L. E., Galbraith, D., et al. (2009). Exploring the likelihood and mechanism of a climate-change-induced dieback of the Amazon rainforest. *Proc. Natl. Acad. Sci. U.S.A.*, 106(49), 20610-20615.
- Malhi Y, Doughty CE, Galbraith D. (2011) The allocation of ecosystem net primary productivity in tropical forests. *Philos Trans R Soc London Ser B*, 366(1582), 3225-3245.
- Malhi Y. (2012) The productivity, metabolism and carbon cycle of tropical forest vegetation. *J Ecol*, 100(1), 65-75.
- Malhi, Y. et al. The linkages between photosynthesis, productivity, growth and biomass in lowland Amazonian forests. *Global Change Biol.* 21, 2283-2295 (2015).
- Malhi, Y., Rowland, L., Aragão, L. E. & Fisher, R. A. New insights into the variability of the tropical land carbon cycle from the El Niño of 2015/2016. *Philos. Trans. R. Soc. London, Ser. B* 373, 20170298 (2018).

	Ref	CCI Biomass Climate Assessment Report v3		
	Issue	Page	Date	
	3.0	80	14.07.2021	

Martens, B. et al. GLEAM v3: Satellite-based land evaporation and root-zone soil moisture. *Geosci. Model Dev.* 10, 1903-1925 (2017).

Martínez-Ramos, M., Alvarez-Buylla, E. R. (1998). How old are tropical rain forest trees?. *Trends Plant Sci.*, 3(10), 400-405.

45. McDowell, N. et al. Drivers and mechanisms of tree mortality in moist tropical forests. *New Phytol.* 219, 851-869 (2018).

Melton, J. R., Arora, V. K. (2016). Competition between plant functional types in the Canadian Terrestrial Ecosystem Model (CTEM) v.2.0. *Geosci. Model Dev.*, 9(1), 323-361.

Mermoz, S., Le Toan, T., Villard, L., Réjou-Méchain, M., Seifert-Granzin, J. (2014). Biomass assessment in the Cameroon savanna using ALOS PALSAR data. *Remote Sens. Environ.*, 155, 109-119.

Mitchard, E. T., Saatchi, S. S., Baccini, A., et al. (2013). Uncertainty in the spatial distribution of tropical forest biomass: a comparison of pan-tropical maps. *Carbon Balance Manag.*, 8(1), 10.

Mitchard, E. T. The tropical forest carbon cycle and climate change. *Nature* 559, 527-534 (2018).

Negrón-Juárez, R. I., Koven, C. D., Riley, W. J., Knox, R. G., Chambers, J. Q. (2015). Observed allocations of productivity and biomass, and turnover times in tropical forests are not accurately represented in CMIP5 Earth system models. *Environ. Res. Lett.*, 10(6), 064017.

Nemani, R. R., Keeling, C. D., Hashimoto, H., et al. (2003). Climate-driven increases in global terrestrial net primary production from 1982 to 1999. *Science*, 300(5625), 1560-1563.

Van Nieuwstadt, M. G., Sheil, D. (2005). Drought, fire and tree survival in a Borneo rain forest, East Kalimantan, Indonesia. *J. Ecol.*, 93(1), 191-201.

Niinemets, Ü. (2001). Global-scale climatic controls of leaf dry mass per area, density, and thickness in trees and shrubs. *Ecology*, 82(2), 453-469.

Le Moigne, P., Boone, A., Calvet, J. C., et al. (2012). SURFEX scientific documentation. Note de centre (CNRM/GMME), Météo-France, Toulouse, France.

Palace, M., Keller, M., Hurtt, G., & Frohling, S. (2012). A review of above ground necromass in tropical forests. *Tropical forests*, 215-252.

Pan, Y., Birdsey, R. A., Fang, J., et al. (2011). A large and persistent carbon sink in the world's forests. *Science*, 333(6045), 988-993.

Peylin P, Law RM, Gurney KR et al. (2013) Global atmospheric carbon budget: results from an ensemble of atmospheric CO2 inversions. *Biogeosci*, 10, 6699-6720.



Phillips, O. L., Aragão, L. E., Lewis, S. L., et al. (2009). Drought sensitivity of the Amazon rainforest. *Science*, 323(5919), 1344-1347.

Piao, S., Ciais, P., Friedlingstein, P., Noblet-Ducoudré, N. D., Cadule, P., Viovy, N., Wang, T. (2009). Spatiotemporal patterns of terrestrial carbon cycle during the 20th century. *Global Biogeochem. Cycles*, 23(4), 16.

Piao, S., Luysaert, S., Ciais, P., et al. (2010). Forest annual carbon cost: A global-scale analysis of autotrophic respiration. *Ecology*, 91(3), 652-661.

Piao, S., Sitch, S., Ciais, P., et al. (2013). Evaluation of terrestrial carbon cycle models for their response to climate variability and to CO2 trends. *Global Change Biol.*, 19(7), 2117-2132.

Piao S, Wang X, Wang K et al. (2020) Interannual variation of terrestrial carbon cycle: Issues and perspectives. *Glob Change Biol*, 26(1), 300-318.

	Ref	CCI Biomass Climate Assessment Report v3		
	Issue	Page	Date	
	3.0	81	14.07.2021	

Poorter, H., Jagodzinski, A. M., Ruiz-Peinado, R., et al. (2015). How does biomass distribution change with size and differ among species? An analysis for 1200 plant species from five continents. *New Phytol.*, 208(3), 736-749.

Potapov, P., Hansen, M. C., Laestadius, L., Turubanova, S., Yaroshenko, A., Thies, C., ... & Esipova, E. (2017). The last frontiers of wilderness: Tracking loss of intact forest landscapes from 2000 to 2013. *Sci. Adv.*, 3(1), e1600821.

Pütz, S., Groeneveld, J., Henle, K., et al. (2014). Long-term carbon loss in fragmented Neotropical forests. *Nat. Commun.*, 5, 5037.

Pugh, T. A., Arneeth, A., Kautz, M., Poulter, B., & Smith, B. (2019). Important role of forest disturbances in the global biomass turnover and carbon sinks. *Nature geoscience*, 12(9), 730-735.

Le Quéré, C., Andrew, R. M., Friedlingstein, et al. (2018). Global carbon budget 2017. *Earth Syst. Sci. Data*, 10, 405-448.

Rammig, A., Jupp, T., Thonicke, K., et al. (2010). Estimating the risk of Amazonian forest dieback. *New Phytol.*, 187(3), 694-706.

Ramo, R., Roteta, E., Bistinas, I., van Wees, D., Bastarrika, A., Chuvieco, E., & van der Werf, G. R. (2021). African burned area and fire carbon emissions are strongly impacted by small fires undetected by coarse resolution satellite data. *Proceedings of the National Academy of Sciences*, 118(9). <https://doi.org/10.1073/pnas.2011160118>

Reichstein, M., Carvalhais, N. (2019). Aspects of forest biomass in the Earth system: its role and major unknowns. *Surv. Geophys.*, 40(4), 693-707.

Rifai, S. W. et al. ENSO Drives interannual variation of forest woody growth across the tropics. *Philos. Trans. R. Soc. London, Ser. B* 373, 20170410 (2018).

Rödenbeck, C., Zaehle, S., Keeling, R. & Heimann, M. History of El Nino impacts on the global carbon cycle 1957–2017: a quantification from atmospheric CO2 data. *Philos. Trans. R. Soc. London, Ser. B* 373, 20170303 (2018).

Rödig, E., Cuntz, M., Rammig, A., Fischer, R., Taubert, F. & Huth, A. The importance of forest structure for carbon fluxes of the Amazon rainforest. *Environ. Res. Lett.* 13, 054013 (2018).

Rowland, L. et al. Death from drought in tropical forests is triggered by hydraulics not carbon starvation. *Nature* 528, 119-122 (2015).

Saatchi, S. S., Harris, N. L., Brown, S., et al. (2011). Benchmark map of forest carbon stocks in tropical regions across three continents. *Proc. Natl. Acad. Sci. U.S.A.*, 108(24), 9899-9904.



Saatchi, S., Asefi-Najafabady, S., Malhi, Y., Aragão, L. E., Anderson, L. O., Myneni, R. B. & Nemani, R. Persistent effects of a severe drought on Amazonian forest canopy. *Proc. Natl. Acad. Sci. U.S.A.* 110, 565-570 (2013).

Saleska, S. R. et al. (2016). Dry-season greening of Amazon forests. *Nature* 531, E4-E5 (2016).

Sankaran, M., Ratnam, J., Hanan, N. P. (2004). Tree-grass coexistence in savannas revisited-insights from an examination of assumptions and mechanisms invoked in existing models. *Ecol. Lett.*, 7(6), 480-490.

Santoro, M., Beaudoin, A., Beer, C., et al. (2015). Forest growing stock volume of the northern hemisphere: Spatially explicit estimates for 2010 derived from Envisat ASAR. *Remote Sens. Environ.*, 168, 316-334.

Santoro, M., Kirches, G., Wevers, et al. (2017). *Land Cover CCI: Product User Guide Version 2.0*.

	Ref	CCI Biomass Climate Assessment Report v3		
	Issue	Page	Date	
	3.0	82	14.07.2021	

Santoro, M., Cartus, O., Mermoz, S., et al. (2018). A detailed portrait of the forest aboveground biomass pool for the year 2010 obtained from multiple remote sensing observations. In EGU General Assembly Conference Abstracts (Vol. 20, p. 18932).

Santoro, M., et al. (2021). Forest aboveground biomass pool of 2010 estimated from high-resolution spaceborne remote sensing observations, *JSTARS* (in press)

Scurlock JMO, Asner GP, Gower ST. (2001) Worldwide historical estimates and bibliography of leaf area index, 1932–2000. In ORNL Technical Memorandum TM-2001/268, Oak Ridge National Laboratory, Oak Ridge, Tennessee, USA.

Seidl, R. et al. Forest disturbances under climate change. *Nat. Clim. Change* 7, 395-402 (2017).

Sellers, P. J., Bounoua, L., Collatz, G. J., et al. (1996). Comparison of radiative and physiological effects of doubled atmospheric CO₂ on climate. *Science*, 271(5254), 1402-1406.

Seveviratne, S. et al. Changes in climate extremes and their impacts on the natural physical environment. In *Managing the Risks of Extreme Events and Disasters to Advance Climate Change Adaptation: Special Report of the Intergovernmental Panel on Climate Change* (pp. 109-230). Cambridge University Press (2012).

Shenkin, A., Bolker, B., Peña-Claros, M., Licona, J. C., Ascarrunz, N. & Putz, F. E. Interactive effects of tree size, crown exposure and logging on drought-induced mortality. *Philos. Trans. R. Soc. London, Ser. B* 373, 20180189 (2018).

Shiodera, S., Rahajoe, J. S., & Kohyama, T. (2008). Variation in longevity and traits of leaves among co-occurring understorey plants in a tropical montane forest. *J. Trop. Ecol.*, 121-133.

Sierra, C. A., Müller, M., Metzler, H., Manzoni, S., Trumbore, S. E. (2017). The muddle of ages, turnover, transit, and residence times in the carbon cycle. *Global Change Biol.*, 23(5), 1763-1773.

Simard, M., Pinto, N., Fisher, J. B., & Baccini, A. (2011). Mapping forest canopy height globally with spaceborne lidar. *Journal of Geophysical Research: Biogeosciences*, 116(G4).

Sitch, S., Cox, P. M., Collins, W. J., Huntingford, C. (2007). Indirect radiative forcing of climate change through ozone effects on the land-carbon sink. *Nature*, 448(7155), 791-794.

Sitch, S., Friedlingstein, P., Gruber, N., et al. (2015). Recent trends and drivers of regional sources and sinks of carbon dioxide. *Biogeosci.*, 12(3), 653-679.

Smith, B., Warlind, D., Arneeth, A., et al. (2014). Implications of incorporating N cycling and N limitations on primary production in an individual-based dynamic vegetation model. *Biogeosci.*, 11, 2027-2054.

Smith, W. K., Reed, S. C., Cleveland, C. C., et al. (2016). Large divergence of satellite and Earth system model estimates of global terrestrial CO₂ fertilization. *Nat. Clim. Change*, 6(3), 306-310.



Soong, J. L. et al. Soil properties explain tree growth and mortality, but not biomass, across phosphorus-depleted tropical forests. *Sci. Rep.* 10, 1-13 (2020).

Stark, S. C. et al. Amazon forest carbon dynamics predicted by profiles of canopy leaf area and light environment. *Ecol. Lett.* 15, 1406-1414 (2012).

Stephens, B. B., Gurney, K. R., Tans, P. P., et al. (2007). Weak northern and strong tropical land carbon uptake from vertical profiles of atmospheric CO₂. *Science*, 316(5832), 1732-1735.

Stovall, A. E., Shugart, H. & Yang, X. Tree height explains mortality risk during an intense drought. *Nat. Commun.* 10, 1-6 (2019).

Sullivan, M. J., Lewis, S. L., Affum-Baffoe, K., Castilho, C., Costa, F., Sanchez, A. C., ... & Qie, L. (2020). Long-term thermal sensitivity of Earth's tropical forests. *Science*, 368(6493), 869-874.

	Ref	CCI Biomass Climate Assessment Report v3		
	Issue	Page	Date	
	3.0	83	14.07.2021	

Taylor, K. E., Stouffer, R. J., Meehl, G. A. (2012). An overview of CMIP5 and the experiment design. *Bull. Am. Meteorol. Soc.*, 93(4), 485-498.

Thum, T., MacBean, N., Peylin, P., et al. (2017). The potential benefit of using forest biomass data in addition to carbon and water flux measurements to constrain ecosystem model parameters: case studies at two temperate forest sites. *Agric. For. Meteorol.*, 234, 48-65.

Thurner, M., Beer, C., Santoro, M., et al. (2014). Carbon stock and density of northern boreal and temperate forests. *Global Ecol. Biogeogr.*, 23(3), 297-310.

Thurner, M., Beer, C., Carvalhais, N., Forkel, M., Santoro, M., Tum, M., Schullius, C. (2016). Large-scale variation in boreal and temperate forest carbon turnover rate related to climate. *Geophys. Res. Lett.*, 43(9), 4576-4585.

Thurner, M., Beer, C., Ciais, P., et al. (2017). Evaluation of climate-related carbon turnover processes in global vegetation models for boreal and temperate forests. *Global Change Biol.*, 23(8), 3076-3091.

Tong, X., Brandt, M., Yue, Y., Ciais, P., Jepsen, M. R., Penuelas, J., ... & Rasmussen, K. (2020). Forest management in southern China generates short term extensive carbon sequestration. *Nat. Commun.*, 11(1), 1-10.

55. Tootchi, A., Jost, A. & Ducharme, A. Multi-source global wetland maps combining surface water imagery and groundwater constraints. *Earth Syst. Sci. Data* 11, 189-220 (2019).

Trugman, A. T. et al. Tree carbon allocation explains forest drought-kill and recovery patterns. *Ecol. Lett.* 21, 1552-1560 (2018).

Vicca, S., Luysaert, S., Penuelas, J., et al. (2012). Fertile forests produce biomass more efficiently. *Ecol. Lett.*, 15(6), 520-526.

Viovy, N. (2018). CRUNCEP Version 7-Atmospheric Forcing Data for the Community Land Model. Research Data Archive at the National Center for Atmospheric Research, Computational and Information Systems Laboratory, Boulder CO, USA.

Walker, A. P., Zaehle, S., Medlyn, B. E., et al. (2015). Predicting long-term carbon sequestration in response to CO₂ enrichment: How and why do current ecosystem models differ?. *Global Biogeochem. Cycles*, 29(4), 476-495.

Wang J, Sun J, Xia J et al. (2018) Soil and vegetation carbon turnover times from tropical to boreal forests. *Funct Ecol*, 32(1), 71-82.

Wang X, Piao S, Ciais P et al. (2014) A two-fold increase of carbon cycle sensitivity to tropical temperature variations. *Nature*, 506(7487), 212-215.



Wigneron, J. P. et al. Modelling the passive microwave signature from land surfaces: A review of recent results and application to the L-band SMOS & SMAP soil moisture retrieval algorithms. *Remote Sens. Environ.*, 192, 238-262 (2017).

Wigneron, J. P. et al. Tropical forests did not recover from the strong 2015–2016 El Niño event. *Sci. Adv.* 6, eaay4603 (2020).

Wittig, V. E., Ainsworth, E. A., Naidu, S. L., Karnosky, D. F., Long, S. P. (2009). Quantifying the impact of current and future tropospheric ozone on tree biomass, growth, physiology and biochemistry: a quantitative meta-analysis. *Global Change Biol.*, 15(2), 396-424.

Wright SJ, Kitajima K, Kraft NJB et al. (2011) Functional traits and the growth-mortality trade-off in tropical trees. *Ecology*, 91(12), 3664-3674.

Wu D, Piao S, Liu Y et al. (2018) Evaluation of CMIP5 Earth System Models for the spatial patterns of biomass and soil carbon turnover times and their linkage with climate. *J Clim*, 31(15), 5947-5960.

	Ref	CCI Biomass Climate Assessment Report v3		
	Issue	Page	Date	
	3.0	84	14.07.2021	

Wu, J., Albert, L. P., Lopes, A. P., et al. (2016). Leaf development and demography explain photosynthetic seasonality in Amazon evergreen forests. *Science*, 351(6276), 972-976.

Xia, J., Yuan, W., Lienert, S., et al. (2019) Global patterns in net primary production allocation regulated by environmental conditions and forest stand age: a model–data comparison. *J. Geophys. Res. Biogeosci.*, 124.

Xu, X., Medvigy, D., Joseph Wright, S., Kitajima, K., Wu, J., Albert, L. P., ... & Pacala, S. W. (2017). Variations of leaf longevity in tropical moist forests predicted by a trait-driven carbon optimality model. *Ecol. Lett.*, 20(9), 1097-1106.

Xue, B. L., Guo, Q., Hu, T., Xiao, J., Yang, Y., Wang, G., ... & Zhao, X. (2017). Global patterns of woody residence time and its influence on model simulation of aboveground biomass. *Global Biogeochem. Cycles*, 31(5), 821-835.

Yang, W., Shabanov, N. V., Huang, D., et al. (2006). Analysis of leaf area index products from combination of MODIS Terra and Aqua data. *Remote Sens. Environ.*, 104(3), 297-312.

Yang, Y. et al. Post-drought decline of the Amazon carbon sink. *Nat. Commun.* 9, 1-9 (2018).

Yang, H., P. Ciais, Y. Wang, Y. Huang, J.-P. Wigneron, A. Bastos, J. Chave, J. Chang, C. Doughty, L. Fan, D. Goll, E. Joetzjer, W. Li, R. Lucas, S. Quegan, T. Le Toan, K. Yu (2021). Variations of carbon allocation and turnover time across tropical forests, *Global Ecology and Biogeography*, doi: 10.1111/geb.13302

Yu, Y., Saatchi, S. (2016). Sensitivity of L-band SAR backscatter to aboveground biomass of global forests. *Remote Sens.*, 8(6), 522.

Zaehle, S., Friend, A. D., Friedlingstein, P., Dentener, F., Peylin, P., Schulz, M. (2010). Carbon and nitrogen cycle dynamics in the O-CN land surface model: 2. Role of the nitrogen cycle in the historical terrestrial carbon balance. *Global Biogeochem. Cycles*, 24(1), GB1006.

Zhang, Q., Ficklin, D. L., Manzoni, S., Wang, L., Way, D., Phillips, R. P. & Novick, K. A. Response of ecosystem intrinsic water use efficiency and gross primary productivity to rising vapor pressure deficit. *Environ. Res. Lett.* 14, 074023 (2019).

Zhao, M., Running, S., Heinsch, F. A., Nemani, R. (2010). MODIS-derived terrestrial primary production. In *Land remote sensing and global environmental change* (pp. 635-660). Springer, New York, NY.

Zhao, Z., Li, W., Ciais, P., Santoro, M., Cartus, O., Peng, S., et al. (2021). Fire enhances forest degradation within forest edge zones in Africa. *Nature Geoscience*, 14(7), 479–483. <https://doi.org/10.1038/s41561-021-00763-8>

Zhu, Z., Bi, J., Pan, Y., et al. (2013). Global data sets of vegetation leaf area index (LAI) 3g and fraction of photosynthetically active radiation (FPAR) 3g derived from global inventory modeling and mapping studies (GIMMS) normalized difference vegetation index (NDVI3g) for the period 1981 to 2011. *Remote Sens.*, 5(2), 927-948.

Zhuravleva, I., Turubanova, S., Potapov, P., et al. (2013). Satellite-based primary forest degradation assessment in the Democratic Republic of the Congo, 2000-2010. *Environ. Res. Lett.*, 8(2), 024034.

Zscheischler, J. et al. Future climate risk from compound events. *Nat. Clim. Change* 8, 469-477 (2018).